THESIS FOR THE DEGREE OF DOCTOR OF PHILOSOPHY

Multi-Gigabaud Millimeter-Wave Communication

Challenges and Solutions

Jingjing Chen

Microwave Electronics Laboratory
Department of Microtechnology and Nanoscience – MC2
CHALMERS UNIVERSITY OF TECHNOLOGY
Gothenburg, Sweden, November 2017

Multi-Gigabaud Millimeter-Wave Communication Challenges and Solutions

Jingjing Chen

ISBN: 978-91-7597-650-1

Doktorsavhandlingar vid Chalmers tekniska högskola
Ny serie nr: 4331
ISSN 0346-718X

Technical Report MC2-372
ISSN 1652-0769

Microwave Electronics Laboratory
Department of Microtechnology and Nanoscience – MC2
Chalmers University of Technology
SE-412 96 Goteborg, Sweden
Phone: 46 (0) 31 772 10 00

Printed by Chalmers Reproservice
Gothenburg, Sweden, November 2017

“You don't stop running because you get old, you get old because you stop running.”

— Christopher McDougall, *Born to Run*

Abstract

A major challenge in future mobile networks is to overcome the capacity barrier in wireless communication. Utilizing large bandwidth at higher frequencies is key to enabling capacity upgrade for next generation mobile networks (5G). As expected, multi-gigabit wireless communication is needed to support future 5G networks, particularly in the transport capacity of wireless backhaul and fronthaul. To be futureproof, wireless technologies towards 100 Gbps are of great interest.

Millimeter-wave (mm-wave) frequency bands (30 to 300 GHz) have sufficient bandwidth to support these high data rates. However, due to hardware limitations, it is challenging to implement multi-GHz modulation bandwidth in actual hardware. For example, limited by the sampling rate of analog-to-digital and digital-to-analog converters, conventional digital modulator and demodulator (modem) designs cannot be applied to the very wide bandwidth required. As proof-of-concept, this thesis presents modems with multi-GHz bandwidth capability [A, B, C, D, E], as required for further capacity enhancement when combined with high-order modulations. The solutions in [C, D, E] do not require any data converters, therefore state-of-the-art energy efficiency is achieved [D, E]. The digital receiver in [B], on the other hand, relaxes requirements on the sampling speed thus being cost and power efficient. Enabled by the proposed modems, multi-gigabit transmission is demonstrated over mm-wave bands [B, C, E] and a short-range optical link [D].

Another aspect that limits the practical use of mm-wave is the degradation of the communication signal quality due to high-frequency hardware impairments. In particular, oscillator phase noise increases with the carrier frequency. An analog phase noise mitigation technique is proposed for arbitrary mm-wave signal waveforms [F]. As a new system application, an analog fronthaul radio link is enabled by implementing phase noise mitigation, where LTE transmission is demonstrated at 70/80 GHz as a step towards future 5G systems [G].

To reach 100 Gbps and beyond, despite the wide bandwidth available at mm-wave bands, the simultaneous use of high-order modulations is also required. However, it is primarily the oscillator noise floor that prevents this combination from being successfully achieved, as confirmed in measurements [H]. A new understanding of performance limitation in wideband communication is provided in a detailed study [I], with guidelines on how to improve hardware designs.

Keywords: Frequency multiplier, fronthaul, high frequency oscillator, high data rate, high-order modulation, mobile backhaul, modem, millimeter-wave communication, multi-gigabit, multi-gigabaud, multiplicative noise, phase noise, phase noise mitigation, power detector, PAM-4, VCSEL driver, white noise, 64-QAM, 5G.

List of Publications

Appended papers

The thesis is based on the work contained in the following papers:

[A] **J. Chen**, Z. He, L. Bao, C. Svensson, Y. Li, S. Gunnarsson, C. Stoij and H. Zirath, "10 Gbps 16QAM transmission over a 70/80 GHz (E-band) radio test-bed," in *Proc. 7th European Microwave Integrated Circuit Conference (EuMIC)*, Amsterdam, 2012, pp. 556-559.

[B] Z. He, **J. Chen**, C. Svensson, L. Bao, A. Rhodin, Y. Li, J. An and H. Zirath, "A hardware efficient implementation of a digital baseband receiver for high-capacity millimeter-wave radios," in *IEEE Transactions on Microwave Theory and Techniques*, vol. 63, no. 5, pp. 1683-1692, May 2015.

[C] **J. Chen**, Z. He, Y. Li, T. Swahn and H. Zirath, "A data-rate adaptable modem solution for millimeter-wave wireless fronthaul networks," in *IEEE International Conference on Communication Workshop (ICCW)*, London, 2015, pp. 1-6.

[D] **J. Chen**, Z. He, T. Lengyel, K. Szczerba, P. Westbergh, J. S. Gustavsson, H. Zirath and A. Larsson, "An energy efficient 56 Gbps PAM-4 VCSEL transmitter enabled by a 100 Gbps driver in 0.25 μm InP DHBT technology," in *Journal of Lightwave Technology*, vol. 34, no. 21, pp. 4954-4964, Nov. 2016.

[E] M. Bao, **J. Chen**, R. Kozhuharov and H. Zirath, "A high speed power detector for D-band communication," in *IEEE Transactions on Microwave Theory and Techniques*, vol. 62, no. 7, pp. 1515-1524, July 2014.

[F] **J. Chen**, B. E. Olsson, A. Persson and J. Hansryd, "Experimental demonstration of RF-pilot-based phase noise mitigation for millimeter-wave systems," in *IEEE 80th Vehicular Technology Conference (VTC2014-Fall)*, Vancouver, BC, 2014, pp. 1-5.

[G] **J. Chen**, B. E. Olsson, J. Hansryd and I. Gerszberg, "Demonstration of analog millimeter-wave fronthaul link for 64-QAM LTE signal transmission," in *IEEE 82nd Vehicular Technology Conference (VTC2015-Fall)*, Boston, MA, 2015, pp. 1-5.

[H] **J. Chen**, Z. He, D. Kuylenstierna, T. Eriksson, M. Hörberg, T. Emanuelsson, T. Swahn and H. Zirath, "Does LO noise floor limit performance in multi-gigabit millimeter-wave communication?," in *IEEE Microwave and Wireless Components Letters*, vol. 27, no. 8, pp. 769-771, Aug. 2017.

[I] **J. Chen**, D. Kuylenstierna, S. E. Gunnarsson, Z. He, T. Eriksson, T. Swahn and H. Zirath, "Influence of white LO noise on wideband millimeter-wave communication," *submitted to IEEE Transactions on Microwave Theory and Techniques, September 2017.*

Other papers

The following papers have been published but are not included in the thesis. The content partially overlaps with the appended papers or is outside the scope of the thesis.

[a] J. Hansryd, Y. Li, **J. Chen** and P. Ligander, "Long term path attenuation measurement of the 71-76 GHz band in a 70/80 GHz microwave link," in *Proc. 4th European Conference on Antennas and Propagation*, Barcelona, 2010, pp. 1-4.

[b] J. Hansryd, **J. Chen**, Y. Li and B. E. Olsson, "A simple DBPSK modem based on high-speed logical gates for a 70/80 GHz GbE microwave link," in *IEEE 71st Vehicular Technology Conference (VTC 2010-Spring)*, Taipei, Taiwan, 2010, pp. 1-4.

[c] Z. He, **J. Chen**, Y. Li and H. Zirath, "A novel FPGA-based 2.5Gbps D-QPSK modem for high capacity microwave radios," in *IEEE International Conference on Communications*, Cape Town, 2010, pp. 1-4.

[d] Z. He, W. Wu, **J. Chen**, Y. Li and H. Zirath, "An FPGA-based 5 Gbit/s D-QPSK modem for E-band point-to-point radios," in *Proc. 41st European Microwave Conference (EuMC)*, Manchester, 2011, pp. 690-692.

[e] M. Bao, **J. Chen** and L. Aspemyr, "A single-chip 15 to 30 GHz six-port demodulator for multi-Gb/s communication," in *IEEE/MTT-S International Microwave Symposium Digest*, Montreal, QC, 2012, pp. 1-3.

[f] Z. Ghebretensae, K. Laraqui, S. Dahlfort, **J. Chen**, Y. Li, J. Hansryd, F. Ponzini, L. Giorgi, S. Stracca and A. R. Pratt, "Transmission solutions and architectures for heterogeneous networks built as C-RANs," in *Proc. 7th International Conference on Communications and Networking in China*, Kun Ming, 2012, pp. 748-752.

[g] M. Bao, **J. Chen**, R. Kozhuharov and H. Zirath, "14 Gbps on-off keying modulator and demodulator for D-band communication," in *IEEE International Wireless Symposium (IWS 2014)*, X'ian, 2014, pp. 1-4.

[h] S. An, **J. Chen**, Z. He, S. Wang and H. Zirath, "A 40 Gbps DQPSK modem for millimeter-wave communications," in *Asia-Pacific Microwave Conference (APMC)*, Nanjing, 2015, pp. 1-3.

[i] S. An, Z. He, **J. Chen**, Y. Li and H. Zirath, "An 8 Gbps E-band QAM transmitter using symbol-based outphasing power combining technique," in *Proc. IEEE International Symposium on Radio-Frequency Integration Technology (RFIT)*, Seoul, 2017, pp. 150-152.

[j] C. Du, Z. He, **J. Chen**, A. Piemontese, J. An, H. Zirath and T. Eriksson, "Experimental verification of phase noise robust spiral constellation for THz and Optical Communication," in *Asia-Pacific Microwave Conference (APMC)*, Kuala Lumpur, 2017.

Thesis

Part of the research work during the doctoral study has been published in [k]. Therefore, contents including figures and text from [k] may be fully or partially reproduced in this thesis.

[k] **J. Chen**, "Multi-gigabit radio system demonstrators for next generation mobile networks," Thesis for the degree of Licentiate of Engineering, Department of Microtechnology and Nanoscience, Chalmers University of Technology, Gothenburg, Sweden, May 2015.

Abbreviations

3G/4G/5G	Third/Fourth/Fifth generation mobile communications technology
ADC	Analog to digital converter
ASK	Amplitude shift keying
AWG	Arbitrary waveform generator
AWGN	Additive white Gaussian noise
BBU	Baseband unit
BER	Bit error rate
BPF	Band pass filter
CDR	Clock and data recovery
C-RAN	Centralized radio access network
CR	Carrier recovery
CPRI	Common public radio interface
DAC	Digital to analog converter
DBPSK	Differential binary phase shift keying
DDCR	Decision-direct carrier recovery
DHBT	Double heterojunction bipolar transistor
DQPSK	Differential quadrature phase shift keying
DSP	Digital signal processing
ER	Extinction ratio
EVM	Error vector magnitude
FDD	Frequency division duplexing
FFE	Feed-forward equalization
FPGA	Field programmable gate array
GbE	Gigabit Ethernet
CoMP	Coordinated multi-point transmission
IF	Intermediate frequency
InP	Indium phosphide
ISI	Inter-symbol interference
LO	Local oscillator
LPF	Low pass filter
LTE	Long-term evolution
MIMO	Multiple input and multiple output

MMF	Multimode fiber
Modem	Modulator and demodulator
OFDM	Orthogonal frequency division multiplexing
OMA	Optical modulation amplitude
OOK	On-off keying
PAM	Pulse amplitude modulation
PCB	Printed circuit board
PAPR	Peak-to-average power ratio
PLL	Phase-locked loop
PN	Phase noise
PRBS	Pseudorandom binary sequence
PSPR	Pilot-to-signal power ratio
QAM	Quadrature amplitude modulation
QPSK	Quadrature phase shift keying
RAT	Radio access technology
RBS	Radio base station
RF	Radio frequency
RRU	Remote radio unit
SQAM	Spiral QAM
STR	Symbol timing recovery
SNR	Signal-to-noise ratio
VCSEL	Vertical cavity surface emitting laser

Contents

Chapter 1

Introduction

1.1 Background

Mobile networks are currently evolving from 4G LTE (long-term evolution) to the next generation, known as 5G, to be commercially launched around 2020. Mobile connectivity will extend beyond people to device and machine communication. Driven by the Internet of things (IoT), fifteen billion devices are expected to be connected by 2020 [1]. A thousandfold increase in traffic volume is predicted in future 5G mobile networks [2]. Accordingly the capacity of mobile backhaul in the transport network must be enhanced in order to support the evolving access technologies.

In today's LTE networks, the mobile backhaul connects a baseband unit (BBU) in a radio base station (RBS) to the core network. To improve the network capacity and coverage, it is expected that a large number of small cells will be deployed as a complement to the existing macro cells. Centralized baseband architecture, also referred to as the centralized radio access network (C-RAN) is believed to be a cost-efficient solution for network densification [3]. In a C-RAN network, the cell sites are simplified with only the remote radio units (RRU) deployed next to the antennas, while the BBUs are placed centrally for baseband processing and advanced coordination among the cells. A new network segment, mobile fronthaul, is created as a connection between the RRU and the BBU. Fig. 1.1 illustrates the difference between mobile backhaul and fronthaul. The mobile network architecture will evolve from the current distributed baseband deployment (Fig. 1.1 (a)) to a mixture of distributed and centralized baseband (Fig. 1.1 (b)) deployments [4].

As shown in Fig. 1.2, the combination of point-to-point microwave and fiber links is the main backhaul solution with microwave being the dominant technology [4]. Wireless solutions enable flexible and quick deployments, although the capacity of microwave links is limited mainly due to bandwidth regulations. The practical choice of backhaul media concerns more about fiber availability and cost issues than capacity. Therefore, more than 65% of all cell sites will be connected wirelessly in 2020, and multi-gigabit transport capacity will be needed in fronthaul and backhaul connections (see Fig. 1.1). A main challenge in future mobile networks is to overcome the capacity barrier in today's wireless technologies.

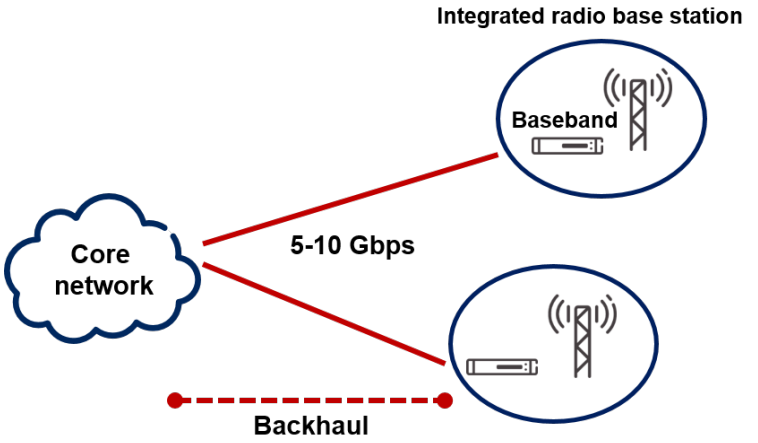

(a)

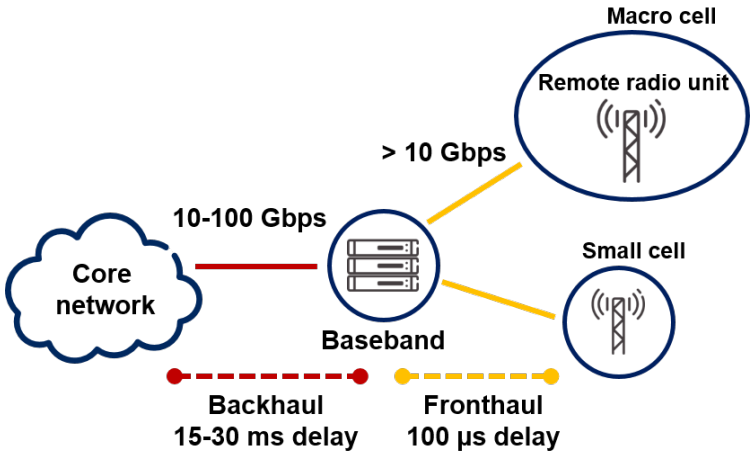

(b)

Figure 1.1: Mobile network evolution, (a) distributed architecture and (b) centralized baseband architecture [4].

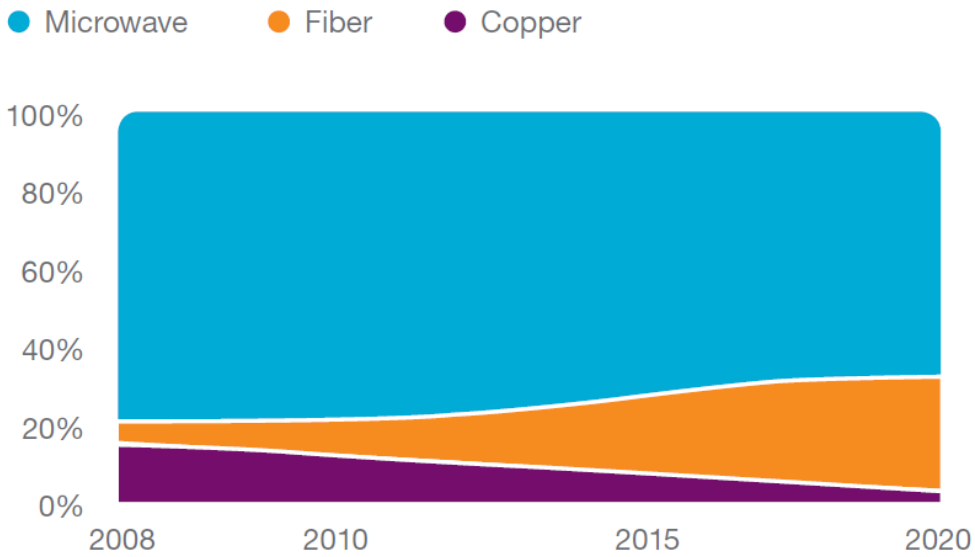

Figure 1.2: Global market share of different backhaul technologies (excluding China, Japan, Korea and Taiwan) according to Ericsson (2015) [4].

1.2 Thesis scope and outline

1.2.1 Motivation and scope

According to Shannon's theorem, the capacity of a communication channel monotonically increases with its bandwidth. Bandwidth in wireless communication is defined in two ways. On the one hand, it is the available spectrum of the frequency band in use. On the other hand, it is the useable bandwidth of the hardware. Millimeter-wave (mm-wave) frequency bands offer sufficient bandwidth so that nearly 100 Gbps has been achieved using over 60 GHz bandwidth [5]. Furthermore, bandwidth of the transmitter and receiver hardware has been significantly improved thanks to advances in semiconductor technologies. One example is a 235 GHz bandwidth amplifier design in InP DHBT technology [6].

Motivated by the technology enablers as discussed above, utilizing multi-GHz modulation bandwidth at mm-wave bands is the key to data rate increase in wireless communication. However, it is challenging to practically implement wideband communication systems. In particular, the clock frequency of commercially available data converters limits the implementation of digital modulator and demodulator (modem) in such wideband systems. Moreover, the signal-to-noise (SNR) degradation due to high frequency hardware impairments limits the practical use of spectrally efficient modulations on mm-wave carriers.

The scope of the thesis is to address hardware challenges in practical implementations of multi-gigabaud (multi-GHz bandwidth) communication. Driven by strong interest from the industry, point-to-point wireless backhaul and fronthaul systems are the main targeted applications. As proof of concept, system solutions are demonstrated at mm-wave bands of commercial interest, such as the 70/80 GHz band (E-band) and 140 GHz band (in this thesis called "D-band").

1.2.2 Outline

The thesis outline is depicted in Fig. 1.3 as a three-layered structure. The theme of the thesis on the top level (red block) is discussed in Chapter 2. In general, system aspects of multi-gigabaud communication are addressed, followed by opportunities given by the mm-wave frequency spectrum and challenges due to hardware limitations. The mid-layer presents two methods (orange blocks) for data rate increase, by improving spectral efficiency (high-order modulation) and utilizing wide modulation bandwidth (high symbol rate), respectively. Chapter 3 describes hardware limitations associated with digital modem designs in multi-GHz wide communication. Hardware-efficient modem solutions [A–E] are proposed as alternatives to conventional digital modems. In Chapter 4 on spectrally efficient communication, oscillator phase noise impairment and various phase noise reduction techniques are discussed. To deal with the phase noise challenge, solutions in [F, G] are presented. Theoretically, the combination of wideband and high spectral efficiency would be the ideal approach for capacity upgrade, as indicated by the third layer (orange block). A new understanding of the hardware challenge is introduced in Chapter 5. Experimental verifications and hardware design improvements are provided in [H, I]. Chapter 6 concludes the main scientific results in the thesis with suggestions on possible future research. Finally, appended papers [A–I] are summarized in Chapter 7.

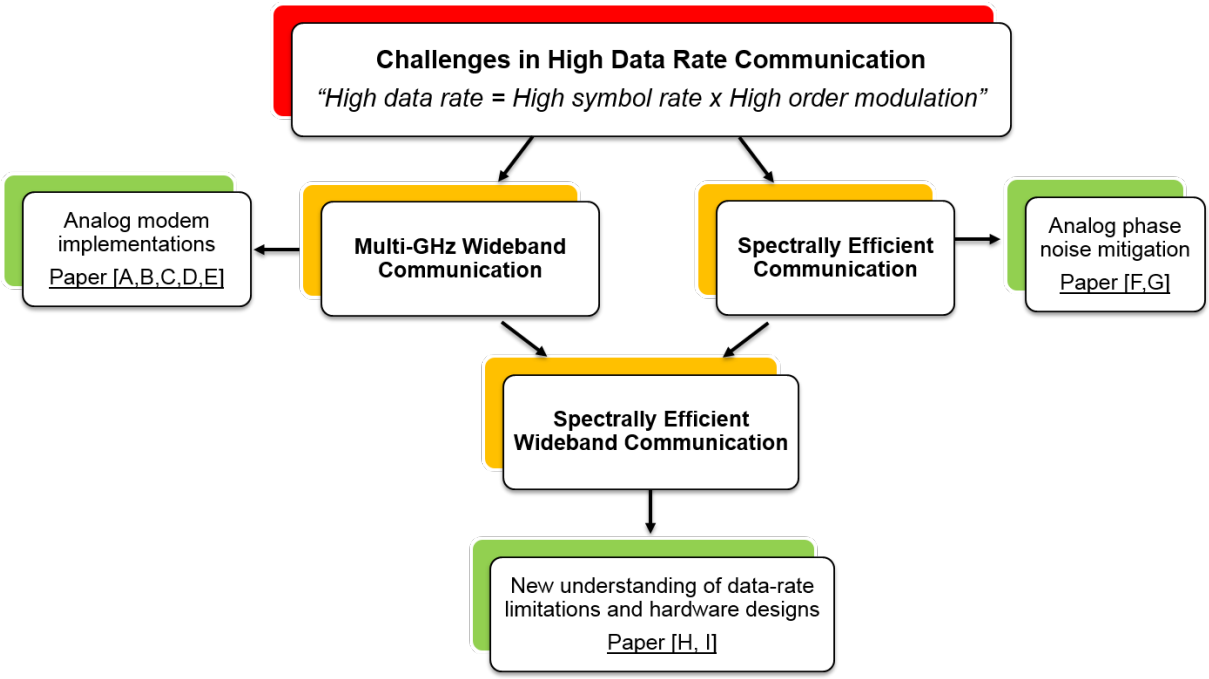

Figure 1.3: Thesis outline in block diagrams.

Chapter 2

High Data Rate Communication

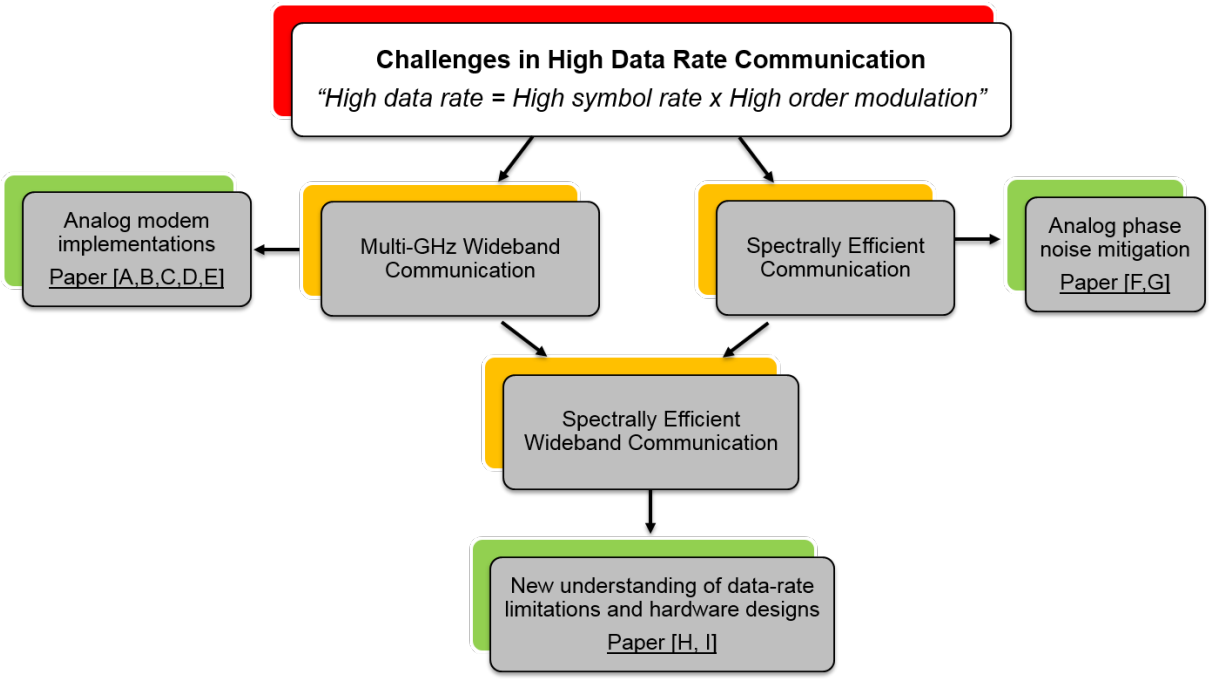

Figure 2.1: Thesis outline in block diagrams.

2.1 Capacity enhancement

Expressed in eq. (2.1) [7], the Shannon's theorem states the channel capacity, *C*, over a communication channel as a function of the channel bandwidth *B* and the signal-to-noise as a power ratio of the communication signal *SNR*

$$C = B\log_2\left(1+\frac{S}{N}\right). \tag{2.1}$$

The equation can also be expressed as [8]

$$C = 2B\log_2\left(L\right)$$

$$L = \sqrt{1+\frac{S}{N}}, \tag{2.2}$$

where *L* is the number of distinct pulse levels of the transmitted signal. $L = \sqrt{M}$ for *M*-order square QAM signals with $M = 2^k$ and *k* is even. For instance, *L* is equal to 4 for a 16-QAM modulated signal.

As indicated in eq. (2.2), the capacity of a communication channel can be increased proportionally either by increasing the channel bandwidth for a given SNR requirement, or at a given bandwidth, applying high-order modulations which result in a very high (i.e. difficult) requirement on SNR.

2.1.1 Bandwidth in communication systems

In principle, there are two ways to increase transmission capacity of a given communication channel: i) by increasing the data/modulation bandwidth and ii) by efficiently using the available bandwidth. Sufficient bandwidth is the key to high data rate communication, which is applicable to both wired and wireless channels.

Communication channels

There are three main mediums available for communication: copper cable, fiber optic cable and wireless. Over the past 100 years, copper cables were the dominant means of communication. Copper cabling is preferred for short distance and low bandwidth applications due to its simplicity and low cost. On the other hand, optical fiber is often chosen for systems demanding high speed and/or long transmission distance. Fiber optic communication was introduced in the 1980s for commercial use, offering advantages over electrical transmission, such as high bandwidth, low attenuation, and immunity to electromagnetic interference. Optical fibers have replaced copper wires in mobile backhaul networks, a network segment of mobile communication (refer to Fig. 1.2). However, trenching fiber can be expensive especially in cities, therefore fiber is not used everywhere. Wireless communication, being a flexible technology due to fast installation, becomes a cost-efficient alternative to optical fibers, as in the mobile backhaul application for example.

Limitations of the channels

Factors limiting the communication channels may be intrinsic, i.e. related to the hardware used, such as bandwidth of the copper cables, or signal distortion by optical fibers. Alternatively, communication capacity in commonly used wireless systems is limited due to regulations of the channel bandwidth. The use of wide bandwidth at mm-wave bands can relax the bandwidth limitation, where hardware in turn may become the limiting factor for reaching high-capacity potential in mm-wave communication.

Spectrum for wireless transmission

Radio spectrum is a finite resource and its usage is therefore regulated. The spectrum is divided into frequency bands for different types of services. In the case of mobile communication, frequencies below 6 GHz are allocated for radio access, and $6 - 86$ GHz is allocated for microwave backhaul as fixed service systems. To secure wireless services without interference, the use of channel bandwidth in frequency bands is governed by regulatory institutions, such as the European Telecommunications Standards Institute (ETSI), the Federal Communications Commission (FCC) in the US, and the Ministry of Industry and Information Technology (MIIT) in China.

In conventional microwave bands $6 - 40$ GHz, channels are typically 28 MHz or 56 MHz wide in Europe. New frequency bands can offer 112 MHz and 250 MHz channel bandwidths (which sometimes can be grouped together to form true GHz-wide channels) in the 42 GHz and 70/80 GHz bands, respectively [9]. The available bandwidth is even more limited in radio access technologies, for instance up to a maximum of 20 MHz in the LTE standard.

The key to high capacity wireless transmission is the availability of spectrum. More frequency spectrum is offered to wireless systems by moving up to higher carrier frequencies.

2.1.2 Spectrally efficient technologies

On the other hand, within a limited spectrum, we can upgrade the capacity by using the spectrum in an efficient way through high-order modulations. Taking quadrature amplitude

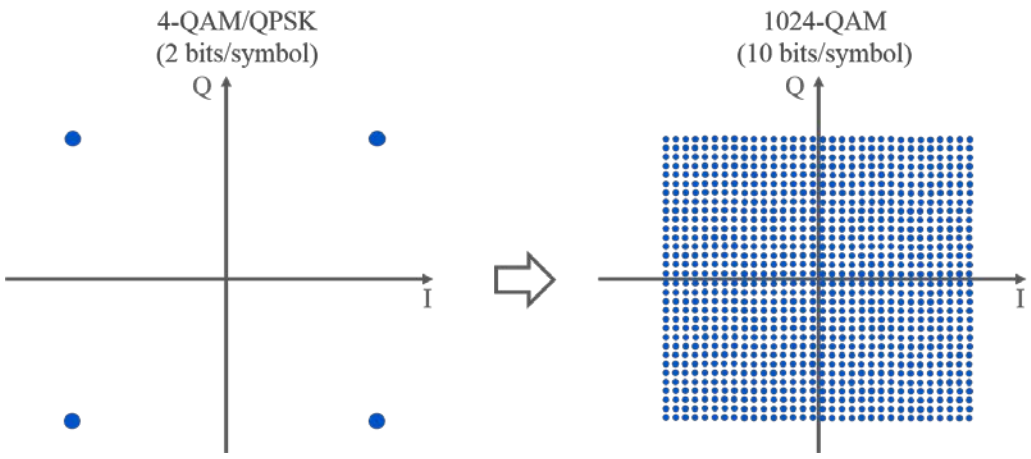

Figure 2.2: Examples of square QAM constellations.

modulation (QAM) as an example, *M*-order QAM (*M*-QAM) modulation means $\log_2(M)$ number of bits are coded on each symbol.

Increasing the modulation order, i.e. from 4-QAM to 1024-QAM, corresponds to a fivefold capacity increase within the same bandwidth (see Fig. 2.2). However, moving to a high-order modulation for a constant average power of the signal, the points in the constellation must be packed denser, and thus are more vulnerable to noise and interference. Consequently, a higher order modulation suffers from a higher bit error rate (BER), or requires a higher SNR to maintain the same BER performance. Coding one more bit per symbol requires 3 dB extra SNR in order not to increase the BER, which corresponds to 3 dB loss in receiver sensitivity. Therefore, an increase from 4-QAM to 1024-QAM leads to 24 dB loss in system gain, and the loss is even higher in reality when taking the transmitter linearity requirement into account. A high-order QAM signal typically has a high value of the peak-to-average power ratio (PAPR). To avoid signal distortion, a lower transmitter output power has to be used for a higher order QAM, to stay in the linear region. Moreover, a high-order QAM demands low phase noise, which in turn requires expensive oscillators and/or advanced digital compensation.

As a result, the capacity gain by using high-order modulations comes at a high expense of system gain, hardware and power consumption.

As a complement to applying a high-order modulation to a single carrier per channel, multi-carrier techniques enabling multiple carriers to share the same channel can be employed to further increase the spectral efficiency and the resulting data rate. Multi-carrier techniques include polarization multiplexing and spatial multiplexing, such as line-of-sight multiple input and multiple output (LoS MIMO) [9]. The focus of this thesis is on high data rate communication solutions realized on a single-carrier, and multi-carrier techniques are the potential enablers for future capacity increase on existing solutions at the expense of more hardware.

2.2 Millimeter-wave communication – opportunities and challenges

At low frequency bands up to 40 GHz, as demonstrated by Ericsson already in 2011, it is possible to reach 1 Gbps in a 28 MHz channel, but it requires 1024-QAM modulated on each carrier signal and in total 4 carriers are used [9]. The same level of data rate can be realized using simple BPSK in a wide channel at 70/80 GHz, which was also demonstrated by Ericsson in [b].

2.2.1 High data rate opportunities

For the benefits of large bandwidth, i.e. tens of GHz, mm-wave frequencies open up high data rate opportunities to fill the capacity gap between fiber optical links and low frequency wireless systems. 70/80 GHz band as an example, known as E-band, offers up to 5 GHz bandwidth which can support up to 10 Gbps capacity [a], [A, B, C] using low-order modulations. Such systems can be implemented, having sufficient gain to allow transmission over a few kilometers [10], [a], [f].

Towards 100 Gbps

In order to enable 10 − 100 Gbps wireless transmission as viable alternatives to optical fibers, the use of frequencies beyond 100 GHz is required because of the high bandwidth available through spectrum allocation at these bands [11], [12]. Assuming that the capacity of real system implementations is scaling with bandwidth as indicated in Fig. 2.3, wide channels up to 10 GHz would support 20 Gbps on a single carrier using 16-QAM modulation as in [A], 40 Gbps using two-carrier in dual polarization, and even up to 100 Gbps enabled by MIMO. The use of MIMO solutions may become feasible beyond 100 GHz frequencies due to the reduction in antenna size and the reduced spatial separation between antenna elements. For example [13], in a 2x2 MIMO configuration for a 1 km hop length, the antenna separation is 1 m, using an antenna diameter of 0.07 m for 40 dBi gain at 150 GHz, as compared to more than 3 m needed between two 15 GHz antennas each with 0.7 m diameter for the same gain. These small antennas at high frequencies are attractive for dense deployments on street level in urban areas as capacity complement to other frequency bands [10]. In addition, a small beam width increases the potential of frequency reuse for improved coverage.

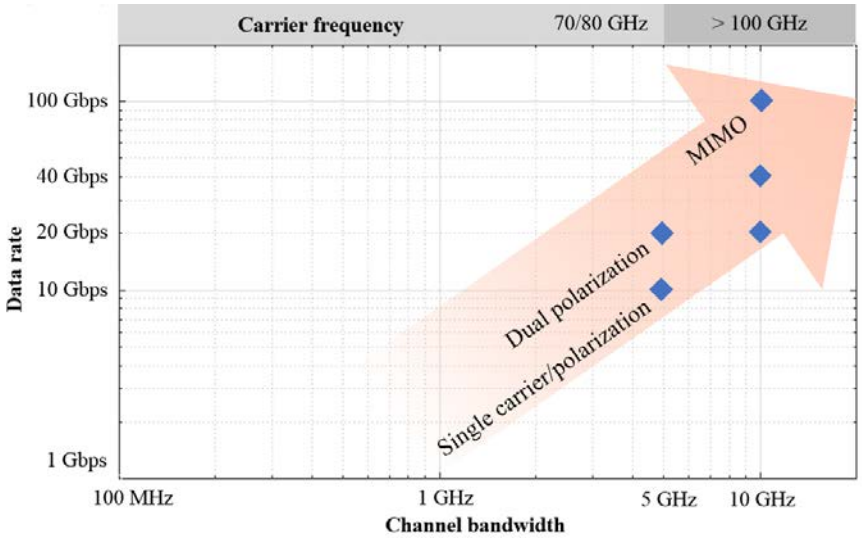

Figure 2.3: Capacity roadmap towards 100 Gbps and beyond using high carrier frequencies.

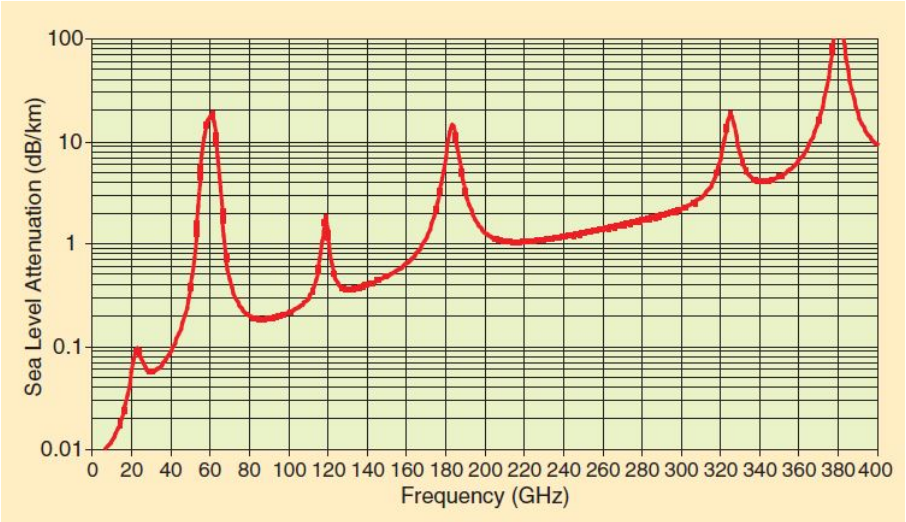

Figure 2.4: Atmospheric attenuation as a function of frequency [12].

Millimeter-wave propagation and frequency allocation

Transmission distance is more limited at mm-wave frequencies compared to the microwave bands (up to 40 GHz), because the atmospheric attenuation and the free-space pass loss both increase with frequency. As shown in Fig. 2.4, there are absorption peaks at certain frequencies to avoid, but the attenuation between the peaks increases slowly beyond 70 GHz. The E-band is regulated in 71 − 76 GHz and 81 − 86 GHz and it is available worldwide for commercial use to fixed services with a light licensing model, allowing low spectrum cost and fast installation. The propagation properties beyond 100 GHz only get slightly worse. For instance, the attenuation increases only about 0.2 dB/km from 70 GHz to 140 GHz; and the free-space path loss, according to eq. (2.3) derived from the Friis transmission equation, increases 6 dB when doubling the frequency.

$$\mathrm{FSPL(dB)} = 20\log_{10}(d) + 20\log_{10}(f) + 20\log_{10}(\frac{4\pi}{c}), \tag{2.3}$$

where d is the transmission distance in meter, f is the frequency in hertz and c is the speed of light.

Spectrum beyond 100 GHz has already been allocated to fixed service systems up to 275 GHz [14], such as the 130 − 170 GHz range, referred to as D-band, and the 252 − 275 GHz range. Research efforts are underway to enable the use of D-band for 10 − 100 Gbps capacity range. For example, 18 Gbps 64-QAM transmission and 48 Gbps QPSK transmission are demonstrated over 143 GHz by Chalmers University of Technology, using transceiver MMICs in InP DHBT technology [15]. As technology becomes mature, D-band link distance in a few kilometres comparable to 70/80 GHz systems can be expected, well suited for urban deployments [11].

2.2.2 Millimeter-wave system implementation challenges

In mm-wave communication systems, hardware performance is challenged, associated with the use of wide bandwidth and the use of mm-wave carriers. Firstly, utilization of wide channel bandwidth requires hardware components with wide operational bandwidth, such as wideband transmitter and the receiver, as well as wideband modulator and the demodulator. Moreover, the RF performance of mm-wave hardware, such as output power and linearity, decreases for increased frequency. Also, other hardware impairments increase with frequency, for example oscillator phase/frequency errors.

2.2.3 Challenges addressed in this thesis

This thesis deals with the following challenges in practical implementations of mm-wave communication systems.

GHz-bandwidth modem implementation

One challenge has been to develop new modem designs at GBaud symbol rate (GHz bandwidth), to overcome limitations of currently available digital data converters, primarily the sampling speed of ADCs. We propose modem solutions that accommodate GHz-wide channels [B, C, D, E], which would be more expensive (more hardware and high power) to realize if conventional digital modem designs were used.

Phase noise impairment on mm-wave carriers

Oscillator phase noise increases $20\log_{10}(N)$ dB when its operational frequency is multiplied by N times. For example, the phase noise is 20 dB higher for a 150 GHz carrier, as compared to a 15 GHz carrier. An analog phase noise mitigation technique is proposed for arbitrary mm-wave signal waveforms [F]. Carrying an LTE signal over mm-wave demands special care to minimize phase noise, which makes it impossible if only the digital phase tracking in an LTE system is used. As a complement to the existing system, the analog method enables an LTE transmission over a 70/80 GHz carrier [G].

A major SNR limitation in wideband mm-wave communication

Applying a high-order modulation to a wideband signal provides extremely high capacity potential in mm-wave communication. Up to now, it has been challenging, if at all possible, to implement this combination due to insufficient SNR of wideband systems. We report a new understanding of oscillator white noise as a primary limitation [H, I], taking a step towards bringing the theories into actual hardware.

Chapter 3

Multi-GHz Wideband Communication

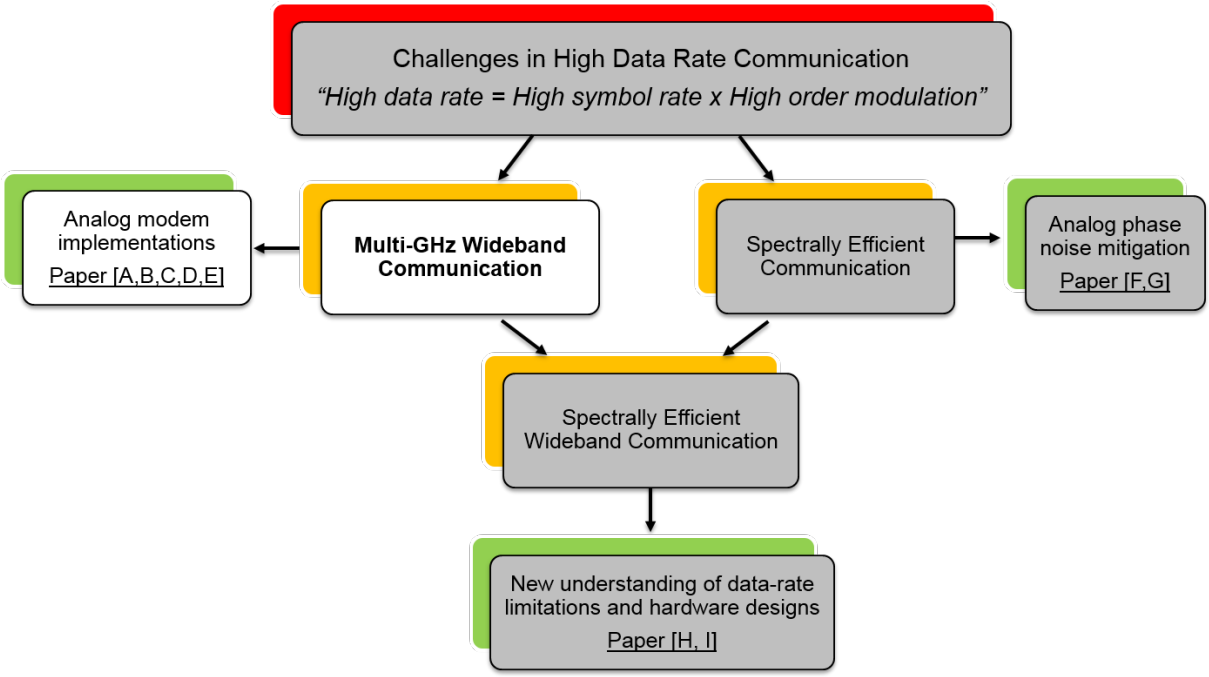

Figure 3.1: Thesis outline in block diagrams.

3.1 Published wideband modem solutions

The reported high data rate transmission experiments in open literature can be grouped in two categories, with and without real-time demodulation. Using off-line demodulation, 96 Gbps is demonstrated on a 240 GHz carrier in a single-channel electronic transceiver [5]. 105 Gbps can potentially be reached using a 6-channel transmitter at 300 GHz [16]. The focus of similar works is on extending the bandwidth of front-end transceivers using advanced semiconductor technologies. On the other hand, a main challenge in wideband communication systems is the implementations of real-time modulators and demodulators (modems) at wide bandwidth.

Table I summarizes published mm-wave transmission experiments using real-time demodulation. Thanks to wideband electronic front-end transceivers, data rates up to 25 Gbps are achieved by applying simple on-off keying (OOK) modulation at 120 and 220 GHz, respectively [E], [17]. When spectrally more efficient modulation format QPSK/DQPSK is utilized, a 20 Gbps 120 GHz link is reported [18] and a multi-rate modem solution for mm-wave systems is proposed [C]. These implementations use analog demodulators, thus ADCs are not needed.

To further improve the spectral efficiency, it is necessary to apply higher-order modulation formats, i.e. 16-QAM. Such a system requires the receiver to perform coherent demodulation, where a digital demodulator is often used to sample the received analog signal for digital signal processing [21−26], [B]. Normally, the so-called oversampling is applied in which the ADCs operate at a sampling rate several times higher than the symbol rate. This implies that the sampling speed of the ADCs may well be a bottleneck limiting the maximum achievable data rate. For example, in [25], a 10 Gbps 16-QAM system is described which requires a sampling rate of 4 times the symbol rate, because of timing synchronization algorithms. However, limited by the sampling rate of commercially available ADCs, a real-time hardware demodulator is implemented operating at 2 Gbps. To overcome this bottleneck, a commonly used solution is to apply multiple parallel channels so that the symbol rate for each channel is reduced. As in [22] and [23], 4 and 8 channels are used to afford the corresponding oversampling factor 3.2 and 3. It is obvious that multi-channel solutions require more hardware and consume more power compared to single-channel solutions. Alternatively, a single-channel digital demodulator based on minimum oversampling is proposed in [B].

Table I:
Published transmission experiments at mm-wave bands using real-time demodulation.

Ref	Data rate (Gbps)	Modulation	Channel	Sampling factor (Samples/ symbol)	Carrier frequency
[17]	25	OOK	1		220 GHz
[E]	13	OOK	1		120 GHz
[18]	20	DQPSK	1		120 GHz
[C]	5	DQPSK	1	without ADC	E-Band
[C]	10	DQPSK	1		Only modem
[19]	10	QPSK	1		60 GHz
[20]	6.2	QPSK	1		Only demodulator
[21]	2.5	QPSK	1	2.8	60 GHz
[22]	6	8PSK	4	3.2	E-Band
[23]	10	16-QAM	8	3	E-Band
[24]	6.3	16-QAM	1	1.5	60 GHz
[25]	2	16-QAM	1	4	140 GHz
[26]	3	16-QAM	1	4	340 GHz
[B]	5	16-QAM	1	1	E-Band

3.2 Digital modem implementation challenges

3.2.1 Receiver synchronization

In coherent demodulation, the receiver local oscillator must be synchronized with the received signal in frequency and phase. Receiver synchronization includes carrier synchronization and symbol synchronization. Carrier synchronization can be achieved by carrier recovery (CR) to remove frequency and phase differences between the received signal and the receiver local oscillator. Symbol synchronization is achieved by symbol timing recovery (STR) to obtain the optimum sampling point with the best SNR.

Fig. 3.2 depicts a radio receiver in block diagrams, where receiver synchronization is performed in a baseband demodulator. 16-QAM constellations are shown before and after the receiver synchronization. Three circles with different amplitudes become visible after STR, showing the impact of a carrier frequency offset. Once the CR is performed with accurate estimates of the carrier frequency and phase, the rotating effect is removed so that decisions can be made by quantizing the received symbols to the nearest constellation points.

Carrier recovery

There are two major techniques of carrier recovery for QAM modulations [27]. One is the fourth-power loop. It produces a spectral line at $4*f_c$, which is locked by a PLL and then divided by four to generate the wanted carrier at frequency f_c in phase with the received signal. Another technique is the decision-directed carrier recovery (DDCR), where the receiver demodulates the current symbol using a local oscillator and makes a decision as to which it thinks is the most likely corresponding transmitted symbol in the constellation. The phase difference between the received symbol and the constellation point is the feedback error to update the local oscillator.

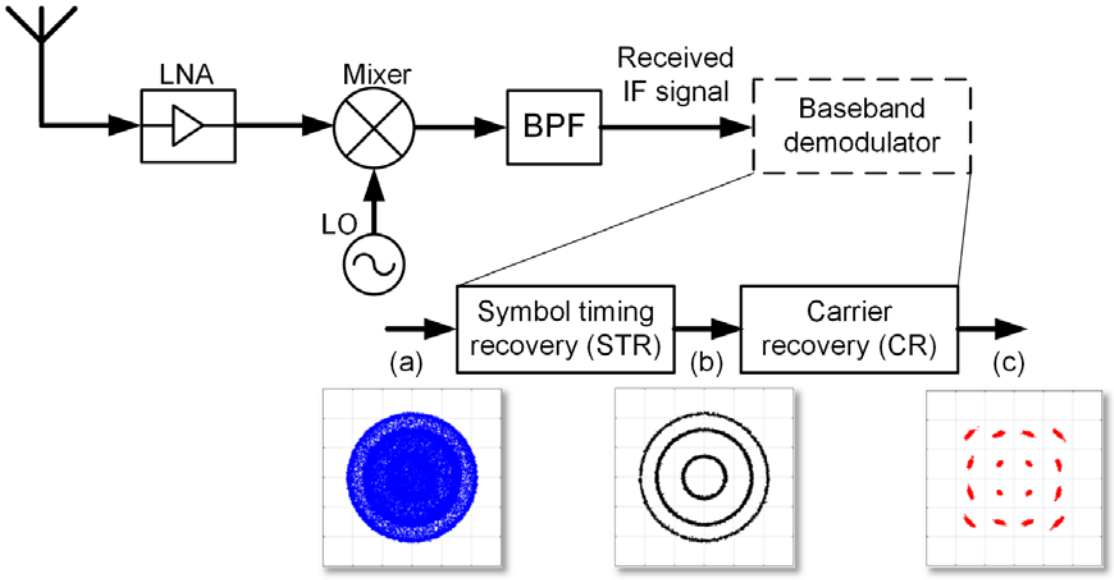

Figure 3.2: Receiver synchronization performed on a 16-QAM signal in a baseband demodulator. Constellations are shown at (a) received data before STR (in blue colour), (b) after STR (in black) and (c) after CR (in red).

Symbol timing recovery

Symbol timing at the receiver must be synchronized with the received signal in frequency and phase. Hence, both the sampling frequency and the sampling phase shall be recovered to ensure that the samples are taken at a correct rate and sampling is taking place in the middle of the symbol period to give the best SNR.

STR can be divided into two groups [27]. Open-loop synchronization (feedforward STR) recovers the symbol clock by non-linear operations on the received signal. On the other hand, closed-loop synchronization (feedback STR) uses the demodulated data stream to control a clock signal from a local oscillator by comparative measurements.

3.2.2 Symbol timing recovery methods

Fig. 3.3 gives an overview of the existing STR implementations. The digital STR in Fig. 3.3 (a) is commonly used in digital communication systems. The sampler (ADC) operates at a fixed sampling rate determined by a local clock. The signal is oversampled and then interpolated in a digital signal processor (DSP) to select the optimum sample. The higher the oversampling/interpolation factor is, the better the STR performs [28]. Therefore, this approach generally requires a high oversampling factor, not practical for high symbol rate applications.

The hybrid STR as in Fig. 3.3 (b) is a closed-loop synchronization approach. It requires a feedback from the DSP to the ADC sampling clock to tune the clock frequency. Whether the sampling occurs too early or too late is determined in the DSP, which requires ADC to perform oversampling. The classic early-late gate algorithm [27] is a closed-loop example, where the generation of the error signal in digital domain requires at least three samples per symbol.

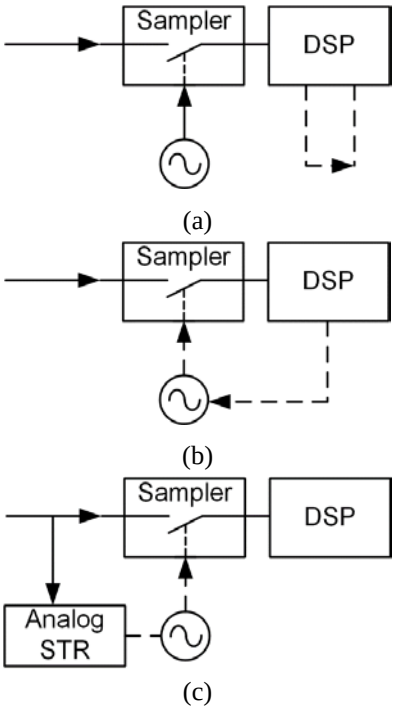

Figure 3.3: Different symbol timing recovery (STR) implementations: (a) digital STR (b) hybrid STR, and (c) analog STR [B].

Fig. 3.3 (c) shows the analog STR as an open-loop synchronization. Analog circuits such as squarer and bandpass-filter [29] are used to extract the symbol clock. The main advantage of this approach is that the STR, performed in the analog domain, is independent of the ADC and the DSP to relax the requirement on the sampling rate. Therefore, it enables the STR implementation at a higher symbol rate as compared to the first two methods [B].

3.3 Hardware-efficient modem demonstrators

3.3.1 Spectrally-efficient QAM demodulator

The basic idea is to realize STR based on one-sample-per-symbol, which relaxes the demand on the ADC's sampling rate. In paper [C], we propose an implementation solution for such digital QAM demodulator. In this sense the proposed solution is hardware-efficient. This is beneficial for two reasons: i) for a given sampling rate, the ADC is applicable to a higher symbol rate as compared to using oversampling; ii) for a given symbol rate, it is possible to use lower-end ADCs to reduce hardware cost and power consumption.

Proposed analog symbol timing recovery

The symbol timing synchronization is achieved in two steps: sampling frequency (symbol clock) recovery, followed by sampling phase recovery. Fig. 3.4 (a) presents the block diagram of the proposed STR implementation.

The symbol clock is recovered as the following. A spectral component at the clock frequency is created through the delay-and-multiply operation on the received analog signal. The length difference of two transmission lines TL_1 and TL_2 provides a true time delay of one symbol period. As shown in Fig. 3.4 (b), the length of TL_2 is adjustable (approximately +/− 5 ps) using 0-Ohm resistors to reduce timing skew. Simulated spectrum after the LPF in Fig. 3.4 (c) shows a pronounced frequency component at the symbol clock rate (1.25 GHz), in comparison with a 10 dB weaker component as the result of 10% timing skew relative to the symbol period (ε_D=10%). We use a commercial clock and data recovery (CDR) module (Silicon Lab, Si5023) that generates the recovered symbol clock signal by locking to the symbol rate frequency component. The ADC uses the clock signal to acquire *I* and *Q* samples.

To ensure that samples are taken by the ADC at the center of each symbol period, sampling phase must be aligned. The sampling phase alignment is implemented in an FPGA, which controls the ADC internal programmable clock delay to maximize the amplitude of acquired *I* and *Q* samples. It is sufficient to adjust the ADC clock delay over one symbol period (800 ps).

Implementation of a real-time 16-QAM demodulator

A proof-of-concept baseband demodulator based on one sample per symbol is implemented using a dual-channel ADC at a sampling rate of 1.25 GSps (giga-sample per second). As an example, 16-QAM is chosen as the modulation format and the resulting operational data rate is 5 Gbps. It is 1.5 times higher than the maximum data rate allowed by the ADC if the lowest sampling factor reported so far were used in the implementation [24].

The realized baseband demodulator consists mainly of an analog STR block and a digital CR block. The CR based on decision-directed technique is implemented in an FPGA using a parallel processing structure [B]. The algorithm is designed to reduce the amount of FPGA hardware resources used. Thus, a digital design including the CR, a BER tester and a logic analyzer function can be realized using the smallest FPGA device (XC4VSX25) in Xilinx Virtex-4 family.

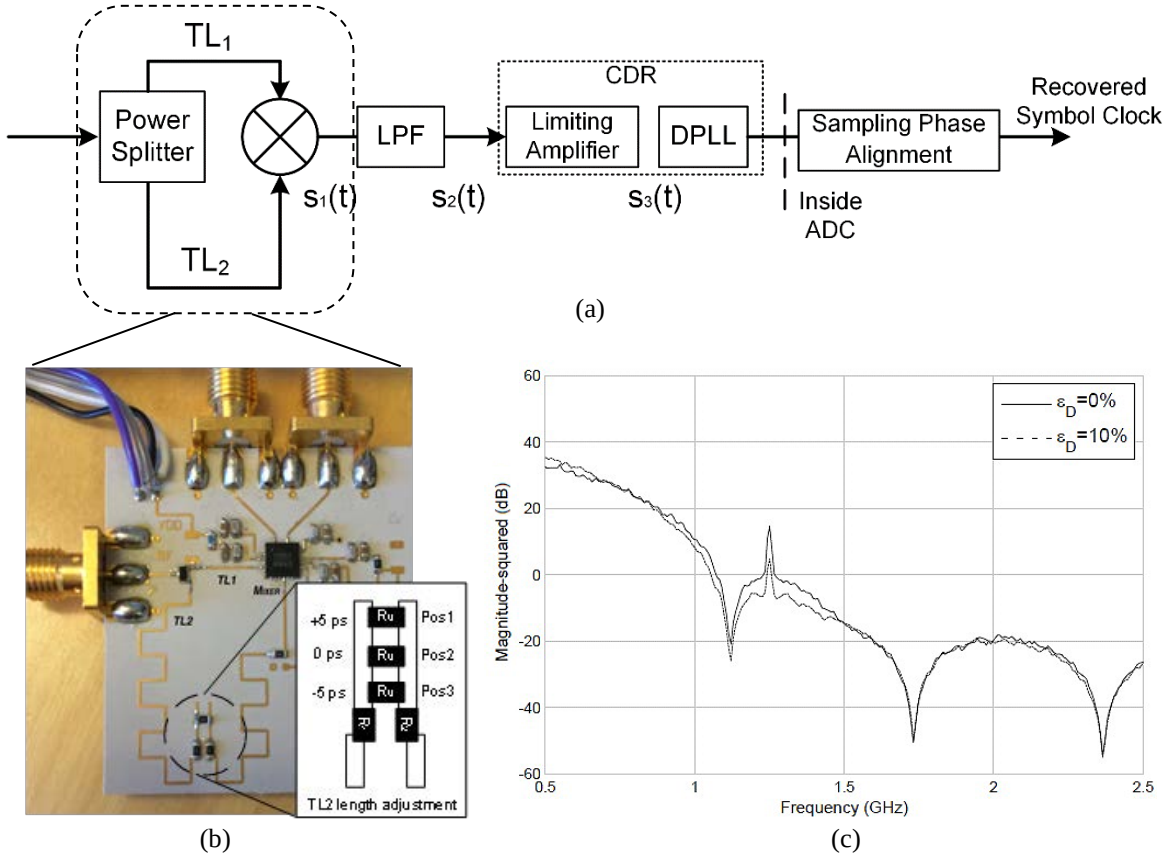

Figure 3.4: Proposed analog symbol timing recovery (STR), (a) block diagram of the STR (b) implementation of delay lines (TL_1 and TL_2) on PCB, and (c) simulated spectrum of $S_2(f)$ after LPF [B], where ε_D is the timing skew relative to the symbol period.

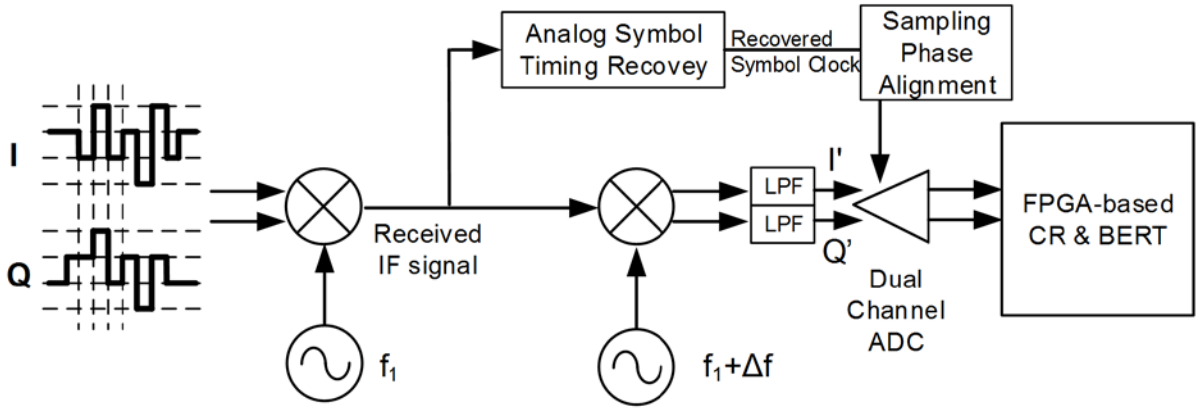

Figure 3.5: Demodulator measurement setup [B].

The function of the baseband receiver is verified in an IF back-to-back set-up as illustrated in Fig. 3.5, where the analog STR is tested together with the FPGA-based CR. A frequency offset Δf is inserted between the transmitter and the receiver LOs. The Δf is varied to investigate the CR operational frequency range. The ADC sampling clock is recovered from the analog STR and the sampling phase alignment is turned on and off to study the impact of the sampling phase offset on the CR performance. The BER tester (BERT) implemented in the FPGA can calculate the error rate down to 10^{-10}.

3.3.2 Data-rate adaptable modem

Review of relevant works

Differential phase-shift keying (D-PSK) modulation allows the receiver to perform non-coherent differential detection without the need for carrier recovery, which simplifies the receiver implementation. In the transmitter, data symbols are encoded as phase difference between adjacent symbols; therefore, the data can be recovered by comparing the phase of the received signal between two adjacent symbol periods.

At high data rates (wide bandwidth), it is hardware-efficient to implement analog differential detection (in Fig. 3.6 (a)), hence avoiding using costly and power-hungry ADCs as required in the digital design in Fig. 3.6 (b). An issue with the analog implementation of differential detection is that, when the data rate changes, the delay element τ must be changed so that the time delay provided is always equal to the symbol period. In practice, this makes it challenging to apply the analog detection to multi-rate transmission in a fixed hardware setup. As for the multi-Gbps D-PSK modems reported in [b], [c], [d], [30], it is not possible to adjust the detection to different data rates without changing the hardware, because the symbol-delay element is a fixed-length transmission line.

In paper [C], we present a novel differential encoding scheme for D-QPSK modulation. A D-QPSK modem based on the new encoding could operate at multiple data rates without changing the physical delay element in the receiver.

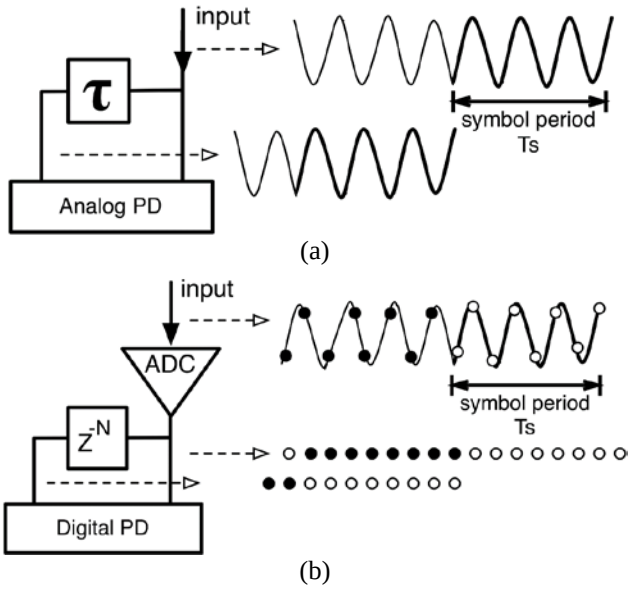

Figure 3.6: Implementations of differential detection (a) in analog domain and (b) in digital domain [C].

Proposed multi-rate differential encoding

In conventional differential encoding, the current symbol $s_{i+1}(t)$ is encoded as a phase difference $\Delta\varphi_i$ applied to the previous symbol $s_i(t)$, as shown in Fig. 3.7 (a). To perform differential detection, a time delay of exactly a symbol period T_s is needed. When the data rate is doubled, the symbol period is reduced from T_s to $T_s/2$, as shown in Fig. 3.7 (b). As a consequence, the provided time delay should be reduced by half as well, which is not straightforward to implement from a hardware standpoint, as discussed in [C].

A new differential encoding scheme is proposed for multi-rate detection using a constant time delay element. The proposed differential encoding rule is shown in Table II, where N is the multi-rate factor. When N=1, the base rate, the proposed scheme is identical to the conventional scheme. The basic idea of the proposed scheme is as follows: when the data rate is N times the base rate, data are encoded by applying a phase difference of $\Delta\varphi_i$ between the i^{th} symbol and the $(i+N)^{th}$ symbol (the N^{th} nearest neighbour symbol), instead of applying $\Delta\varphi_i$ between two adjacent symbols as in the conventional encoding.

An example is given in Fig. 3.7 (c) to illustrate the idea, when the data rate is doubled (N=2). In this case, the required time delay is two symbol periods $2 * T_s/2$. Since the symbol period for N=2 is half of that for the base rate N=1, the required time delay becomes actually the same as that for the base rate. Similarly, the proposed encoding scheme can be scaled up to higher data rates. As explained in Fig. 3.7 (d), when the data rate is tripled (N=3), the identical amount of time delay as for the base rate N=1 in Fig. 3.7 (a) is needed in the receiver.

However, one limitation with the new encoding is that it is not applicable to an arbitrary data rate. The data rate must be an integer multiple of a base rate.

Table II: Proposed differential encoding rule [C].

B_0	B_1	I_{i+N}	Q_{i+N}	$\Delta\varphi_i$
1	0	$\overline{Q_i}$	I_i	270°
0	0	$\overline{I_i}$	$\overline{Q_i}$	180°
0	1	Q_i	$\overline{I_i}$	90°
1	1	I_i	Q_i	0°

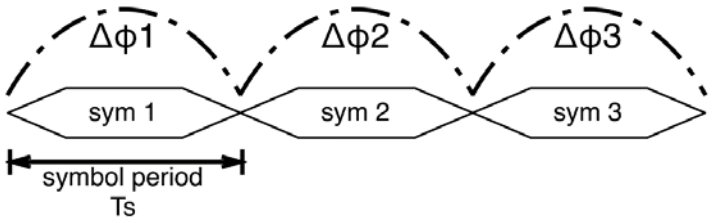

(a) Conventional differential encoding at a base rate

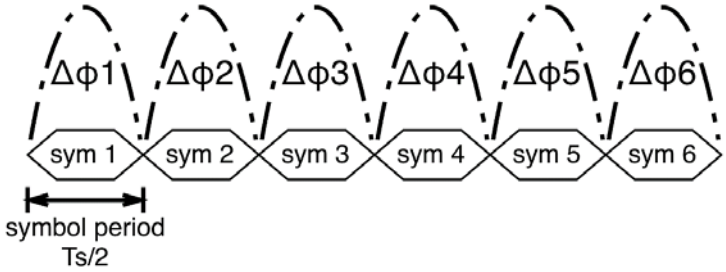

(b) Conventional differential encoding at 2x base rate

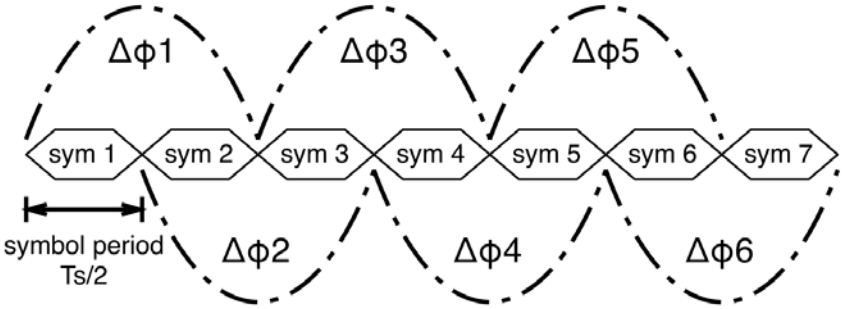

(c) Proposed differential encoding at 2x base rate

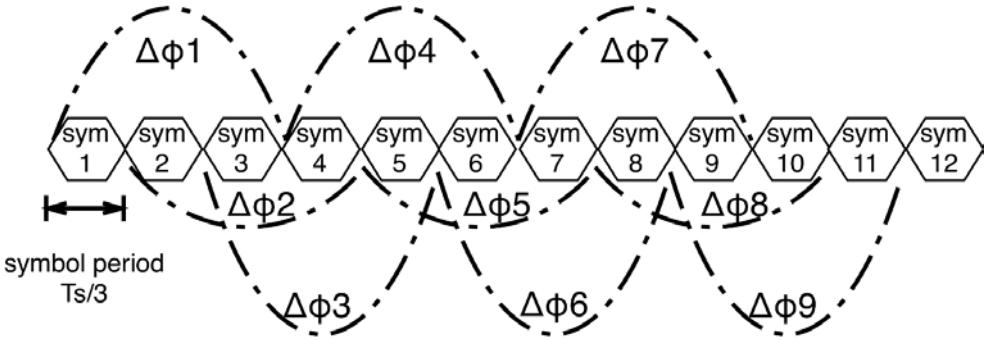

(d) Proposed differential encoding at 3x base rate

Figure 3.7: Comparison of conventional differential encoding with proposed differential encoding, where T_s is the symbol period at the base rate [C].

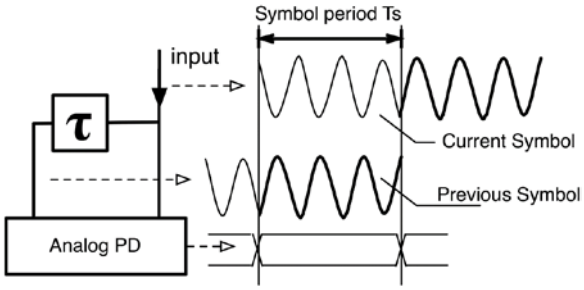

(a) $\Delta\tau = 0$

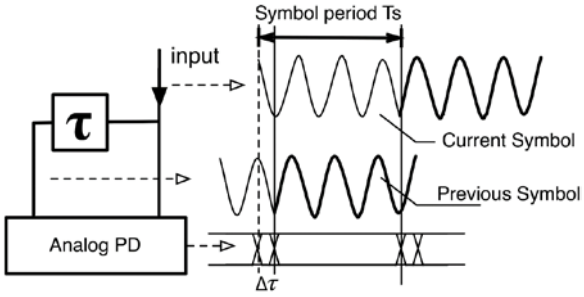

(b) $\Delta\tau \neq 0$

Figure 3.8: Impact of delay variation on differential detection, (a) an ideal symbol delay and (b) with a time skew $\Delta\tau$ [C].

Practical data-rate limitations

Theoretically, the proposed encoding scheme has no upper limit on the data rate as long as it operates at an integer multiple of a base rate. However, as the data rate increases, the symbol period becomes shorter. The tolerance of differential detection to time skew is reduced accordingly. Therefore, it is the time skew in differential detection that limits the highest operational rate of a system using the proposed encoding [C].

As illustrated in Fig. 3.8 (b), a time skew $\Delta\tau$ causes misalignment between the current symbol and the delayed symbol, resulting in inter-symbol interference. When presented in an eye-diagram, this corresponds to an increase of $\Delta\tau$ in transition time, which reduces the detection window (eye opening) for the given symbol rate. The degree of receiver tolerance depends on the actual symbol rate and it is less tolerant to the skew $\Delta\tau$ at a higher data rate.

In reality, non-ideal physical delay elements may introduce a static time skew due to the inaccuracy of the design and manufacturing process. On the other hand, jitter (phase noise on the carrier signal) causes a time-varying skew. The corresponding performance penalty on BER is studied in simulations in the case of D-BPSK modulation with differential detection. For a given phase noise level specified as −80 dBc/Hz at 100 kHz offset, the simulated BER performance is shown in Fig. 3.9 at a base rate of 10 Mbps (N=1) using conventional differential encoding, and at a 10x the base rate (N=10) using the new encoding. The theoretical BER for D-BPSK in an AWGN channel is inserted as a reference. Simulation results indicate that the phase noise penalty on the performance of differential detection increases with increasing the multi-rate factor N. It can be expected that the performance degrades faster with a higher phase noise, typical at higher carrier frequencies. To apply the new differential encoding in high frequency systems, it is critical to incorporate phase noise mitigation, such as the method proposed in [F].

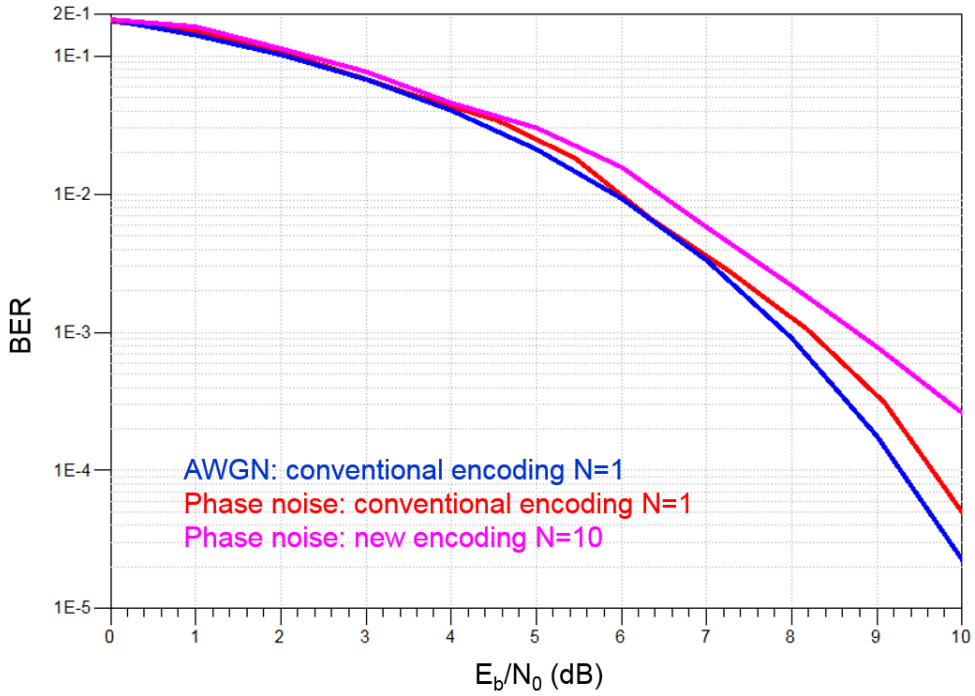

Figure 3.9: Simulated phase noise penalty on the performance of differential detection in D-BPSK modulation.

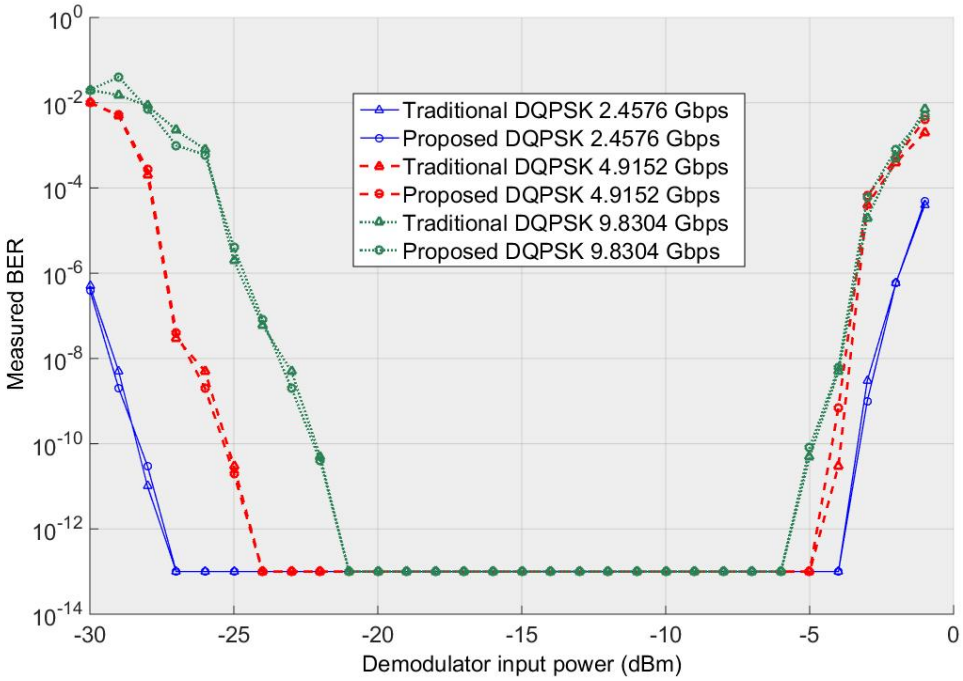

Figure 3.10: Performance comparison between the proposed differential encoding and conventional encoding at different data rates [C].

Multi-rate modem measurements

A multi-rate DQPSK modem is implemented using commercial components and the details are described in [C]. In an IF back-to-back setup, the modem is tested for BER at data rates of 2.5, 5 and 10 Gbps, with 10 Gbps being the limit by the bandwidth of the microwave components in use. The modem achieves error-free transmission (defined as BER < 10^{-13}) at all rates for PRBS-13. BER as a function of the demodulator input power, is presented in Fig. 3.10. The demodulator dynamic range shrinks as the data rate increases, which is attributed to the increased noise power at the higher data rate (wider bandwidth) that reduces the SNR. However, no performance penalty is shown from the modem using the proposed encoding compared to the conventional encoding.

3.4 Energy-efficient multilevel modulator circuit

A MMIC-based multilevel modulator is implemented using a 0.25-μm emitter width InP DHBT process developed by Teledyne Scientific Company [D]. This process has a cut-off frequency (f_T) of 350 GHz, a maximum oscillation frequency (f_{MAX}) of 650 GHz and a maximum collector-emitter breakdown voltage (BV_{CEO}) of 4 V [31]. In the same process, an amplifier with a record −3dB bandwidth of 235 GHz and a gain of 16 dB was demonstrated [6]. Thanks to the high f_T, high BV_{CEO} and low transmission loss of the process, it is feasible to realize wide band circuits using relatively simple circuit topologies. This is beneficial for achieving high energy efficiency, as demonstrated in the modulator circuit [D] and a power detector circuit in the same technology [E].

3.4.1 System applications

The function of the baseband modulator in [D] is the generation of multilevel signals to enable data communications at 100 Gbps and beyond. The modulator is designed as a 3-bit DAC, which can generate 2/4/8-level waveforms in 1, 2, and 3-bit operation mode. Possible system applications enabled by the modulator are illustrated in Fig. 3.11. In a mm-wave transmitter, generation of a wideband 64-QAM signal can be realized using two such modulators followed by an I/Q up-converter, as sketched in Fig. 3.11 (a). The same modulator can be used as a laser driver in short-range optical communications to provide multilevel pulse-amplitude-modulation (PAM) driving signals to the VCSEL (in Fig. 3.11 (b)).

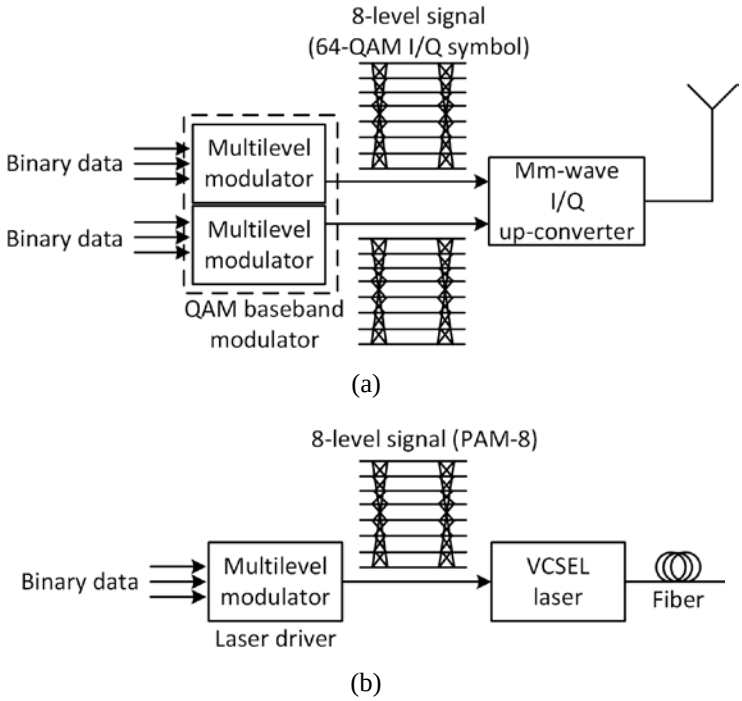

Figure 3.11: Block diagram of system applications enabled by the multilevel modulator, (a) a mm-wave transmitter and (b) a VCSEL-based optical transmitter.

3.4.2 Circuit design

A photo of the fabricated modulator circuit (0.68 mm x 1.08 mm) is shown in Fig. 3.12 (a), with a functional block diagram in Fig. 3.12 (b). The modulator has three binary input bits (B_0 to B_2) with each input passing through a limiting amplifier (in Fig. 3.12 (c)), followed by a data-controlled switch. Each switch is connected to a tuneable current source. The data-controlled switches determine the current flow from three current sources (I_{b0} to I_{b2}) to one of the two nodes in the current sum network (in Fig. 3.12 (d)). For example, as illustrated in the figure with B_0 to B_2 all equal to logic '0', currents I_{b0}, I_{b1} and I_{b2} are summed up at the inverted output of the modulator circuit. By default, $I_{b2} = 2 \times I_{b1} = 4 \times I_{b0}$, thus B_2 becomes the most significant bit (MSB) and B_0 is the least significant bit (LSB). In this design, all three current sources can be adjusted independently using analog control voltages. Therefore, the modulator input bits can be coupled using different weights for multilevel waveform generation. Additionally, the amplitude at each output level is tuneable, which enables possibilities for waveform shaping. The limiting amplifiers have single-ended inputs and all other blocks are in differential operation.

An integration of the modulator as a VCSEL driver is also sketched in Fig. 3.12 (b). The VCSEL is driven differentially by connecting the driver differential outputs to the cathode and anode of the VCSEL. Alternatively, the VCSEL can be driven single-ended by terminating one of the differential outputs of the driver. This leads to a simplified transmitter assembly as implemented in [D].

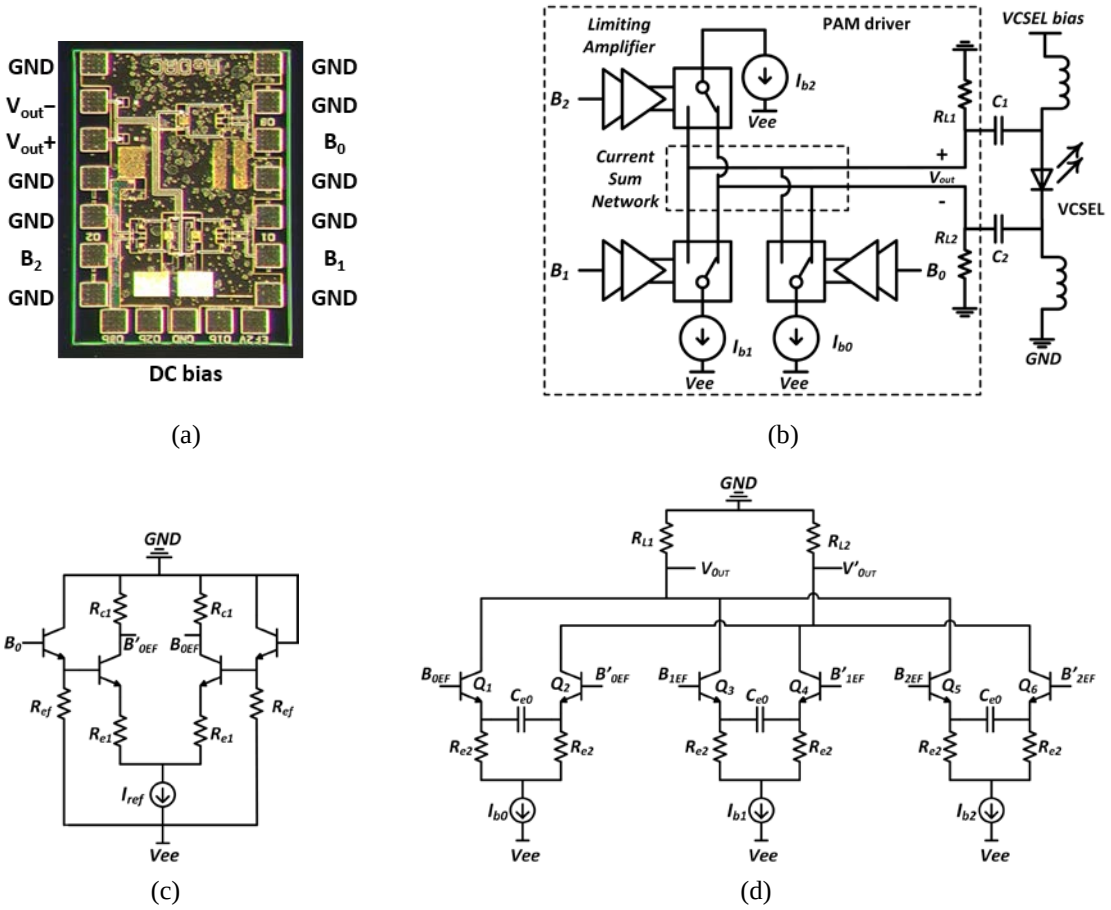

Figure 3.12: Multilevel modulator circuit topology, (a) circuit photograph, (b) block diagram including a VCSEL, (c) circuit schematic of the limiting amplifier and (d) circuit schematic of the current switches and the current sum network [D].

3.4.3 **Performance verification**

The electrical performance is verified for a packaged modulator, where the circuit is wire-bonded to a carrier board (Rogers ULTRALAM 3850) with coaxial connectors at input and output interface.

The quality of the multilevel signal generated is measured in a setup shown in Fig. 3.13. The modulator input channels are fed with uncorrelated binary PRBS streams from a pattern generator. The modulator's output signal is examined with a 70 GHz equivalent-time sampling oscilloscope for eye diagram visualization. The highest measured data rates for the generated PAM-2/-4/-8 signals are at 64 Gbps, 120 Gbps, and 75 Gbps, with the corresponding eye diagrams shown in Fig. 3.14. In addition, bathtub curves are measured using an error analyzer showing the horizontal and vertical eye margins. Fig. 3.15 presents the measured results for the PAM-4 modulation, where the maximum data rate for error-free measurement is achieved up to 100 Gbps. The PAM-4 BER is measured on the middle eye (the eye positioned between the upper one and the lower one), which is an approximation of the modulator performance in PAM-4 operation [32], [33].

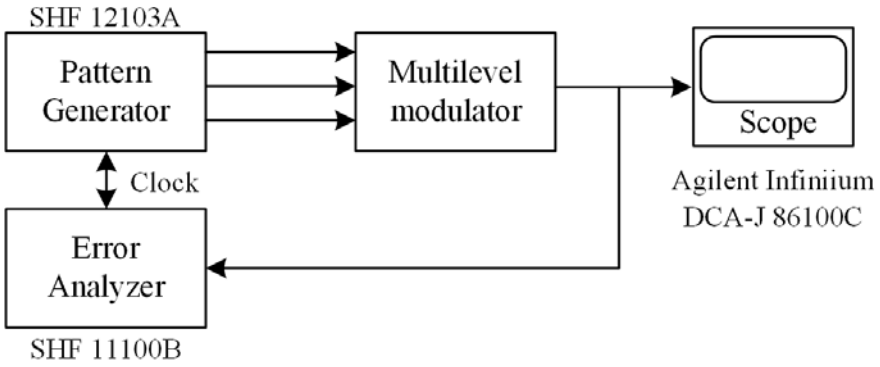

Figure 3.13: Experimental setup for evaluation of the multilevel modulator.

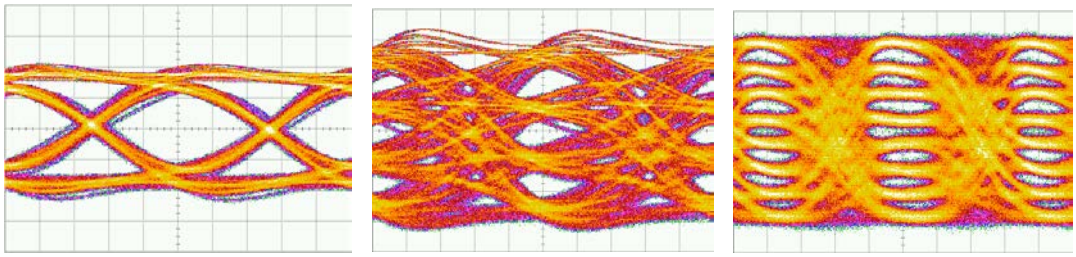

(a) (b) (c)

Figure 3.14: Captured eye diagrams at the driver output with a vertical scale of 100 mV/div, (a) PAM-2 at 64 Gbps, 3.2 ps/div, (b) PAM-4 at 120 Gbps, 3.4 ps/div and (c) PAM-8 at 75 Gbps, 5 ps/div [D].

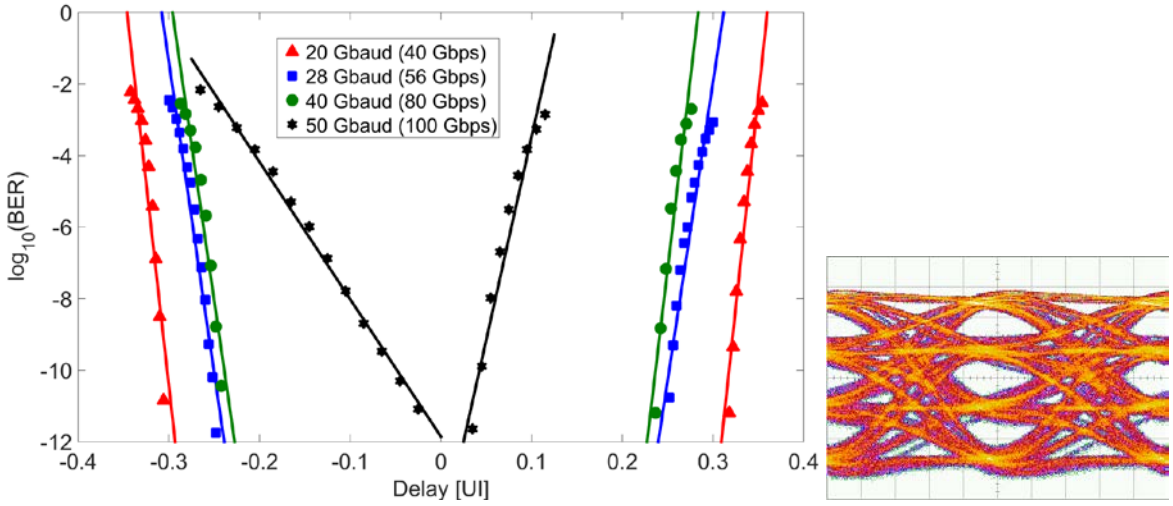

Figure 3.15: Measured bathtub curves of the driver output in PAM-4 modulation. The inset shows the captured PAM-4 eye diagram at 100 Gbps [D].

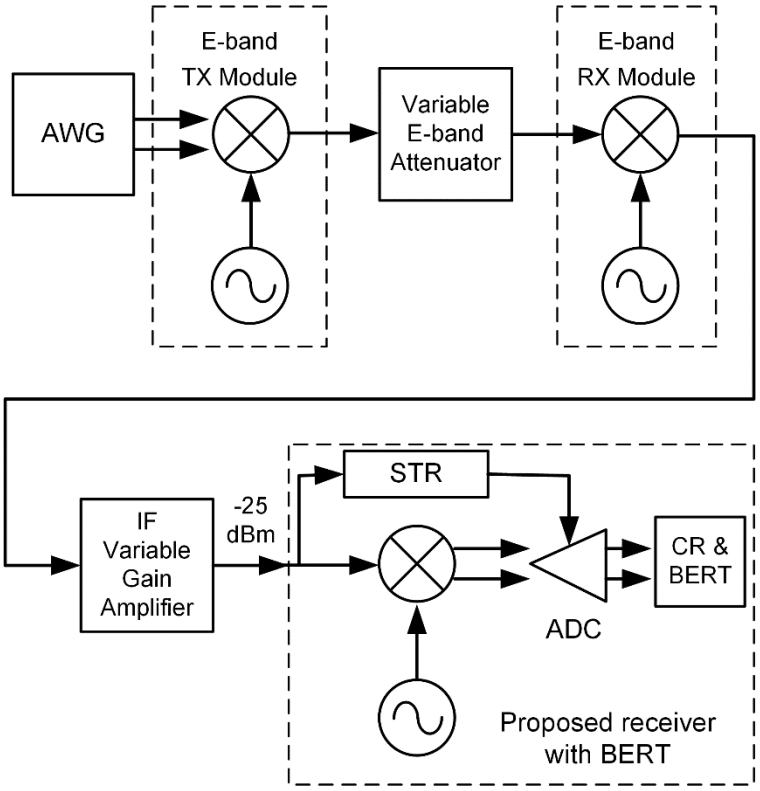

Figure 3.16: Block diagram of mm-wave transmission measurement using the real-time demodulator in [B].

3.5 System demonstrators

The modem solutions in [B] and [C] are proposed for point-to-point mm-wave transmission in future backhaul and fronthaul applications. Driven by strong interest from the industry, 70/80 GHz (E-band) is chosen for the proof-of-concept system demonstration, but the solutions are generally applicable to any mm-wave frequencies.

3.5.1 Multi-gigabit millimeter-wave transmission

Given the available bandwidth in E-band, it is feasible to transmit 10 Gbps data rate using 16-QAM modulation as demonstrated in [A]. The received signal is demodulated offline as a verification of the receiver algorithms designed for the following real-time demodulator implementation. However, to accommodate the sampling rate of the ADC, accessible for the time being, a digital 16-QAM demodulator is implemented at 5 Gbps [B]. When integrated with a commercial E-band transmitter and a receiver (in Fig. 3.16), a 5 Gbps E-band transmission link is demonstrated in a laboratory environment. The performance is verified with measured BER and receiver sensitivity [B].

3.5.2 Millimeter-wave digital fronthaul links

Digital fronthaul links carry digital common public radio interface (CPRI) information between the baseband unit and the remote radio unit (RRU). The CPRI standard specifies data rate at an integer (n) times a base rate of 614.4 Mbps, where n = 1, 2, 4, 5, 8, 10, 16 when using 8B/10B line coding, and the highest rate is 9.8304 Gbps [34]. The mm-wave frequency range, thanks to the wide bandwidth, is the most promising choice to realize wireless transmission of multi-

gigabit CPRI (in Fig. 3.17 (a)). For example, Ericsson demonstrated the world's first CPRI transmission over a 2.5 Gbps E-band radio link as in Fig. 3.17 (b) [f].

In paper [C], we propose a data-rate adaptable DQPSK modem solution for digital mm-wave fronthaul links. The data rate supported by the modem must be an integer multiple of a base rate, which is well suited for a full range of CPRI rates. The modem is verified and fulfils the CPRI specifications with respect to multi-rate, low latency (below 0.1 μs) and high system performance (BER < 10^{-13}). Based on this modem, an E-band radio link is demonstrated in laboratory environment (in Fig. 3.18). Limited by the E-band front-end bandwidth, the maximum data rate of such a link is 5 Gbps in a duplex transmission scheme [C].

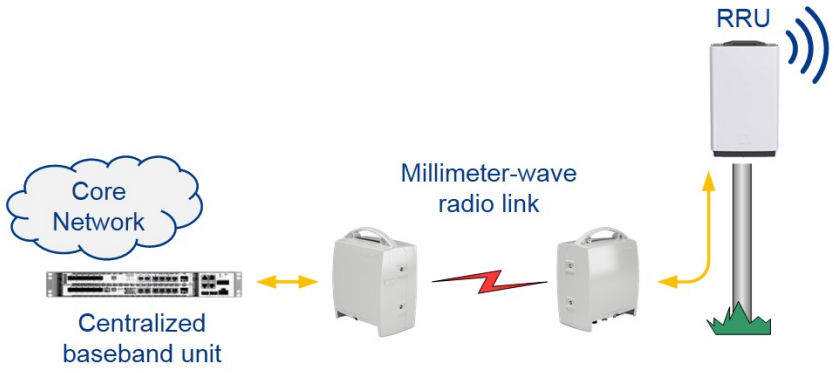

(a)

(b)

Figure 3.17: Digital fronthaul link (a) using mm-wave and (b) demonstration using an E-band link, Beijing, 19th December 2011 [f].

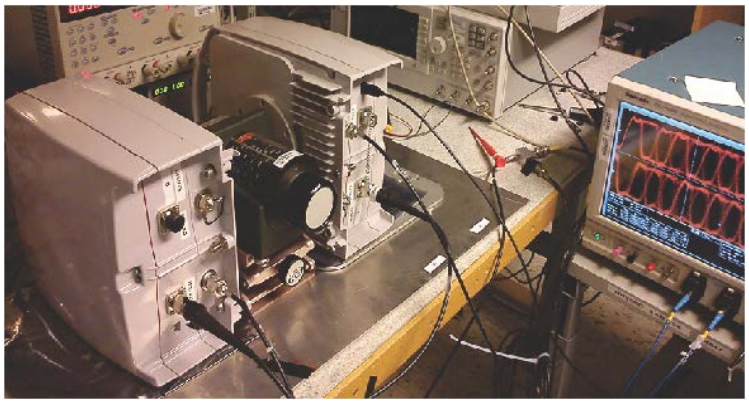

Figure 3.18: Laboratory test-bench of an E-band radio link using the proposed multi-rate modem in [C].

3.5.3 Short-range optical communication

As a proof-of-concept, the high-speed and low-power multi-level modulator in [D], used as a laser driver, is integrated in a VCSEL transmitter. Using a commercial receiver, error-free PAM-4 optical transmission is demonstrated at 56 Gbps with 3.7 pJ/bit consumed by the transmitter. This is the highest data rate reported for a driver-integrated PAM-4 VCSEL transmitter, and being the most energy efficient above 40 Gbps operation.

PAM driver integrated VCSEL link

The PAM driver and an 850 nm VCSEL [35] are integrated as a VCSEL transmitter on a carrier board (Rogers ULTRALAM 3850). Coaxial connectors are mounted on the board to connect the high speed data signal to the driver input interface. Fig. 3.19 (a) illustrates a block diagram of the transmitter integration with wire-bonds indicated by yellow lines, and Fig. 3.19 (b) shows a photograph of the transmitter assembly. The VCSEL is single-ended driven and wire-bonded to the driver single-ended output through a DC-blocking capacitor, while the other output of the driver is connected to a microstrip line with a 50 Ω termination. The VCSEL bias goes through an external inductor followed by a long wire-bond to the VCSEL. The inductor together with the blocking capacitor serve as a bias-T network for feeding the driving signal to the VCSEL.

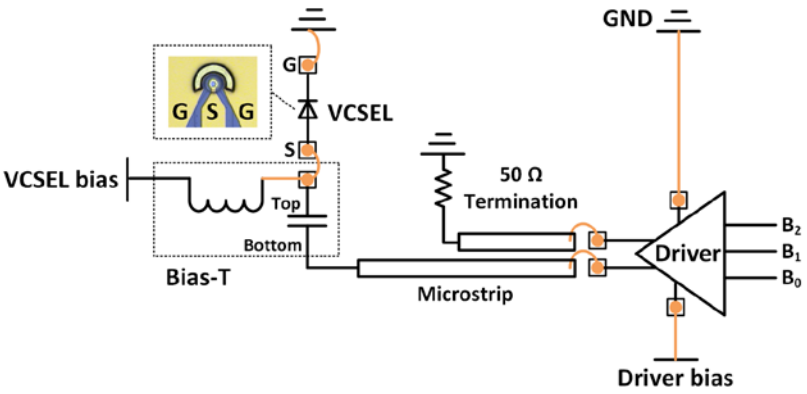

(a)

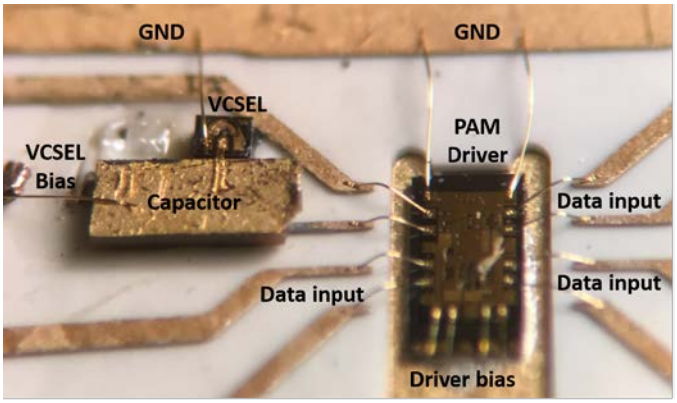

(b)

Figure 3.19: VCSEL transmitter integration, where the VCSEL is single-ended driven, (a) transmitter block diagram and (b) photograph of the transmitter assembly [D].

The performance of the driver-integrated VCSEL transmitter is evaluated in a short optical link, as depicted in Fig. 3.20. The VCSEL is biased at 10 mA for the best eye quality. The VCSEL output is coupled to a multimode fiber (MMF) using a lens package and the launch power is around 5 dBm. A commercial photoreceiver with a −3dB bandwidth of 22 GHz is used. The receiver includes a low gain inverting trans-impedance amplifier (TIA). A variable optical attenuator is connected between the transmitter and the receiver to adjust the received optical power for BER measurements. A DC output voltage from the receiver monitors the received average optical power.

As indicated in Fig. 3.21, the −3dB bandwidth of the driver-integrated VCSEL link is reduced to less than 19 GHz, compared to 25 GHz bandwidth of the stand-alone driver. The bandwidth reduction is mainly caused by adding the VCSEL and the photoreceiver to the driver. Transmission performance in PAM-2 and PAM-4 modulations is characterized over the optical link. The true BER is measured in real-time for PAM-2 modulation using the error analyzer, while the BER of PAM-4 modulation is derived from the measured error rate of the middle eye [36].

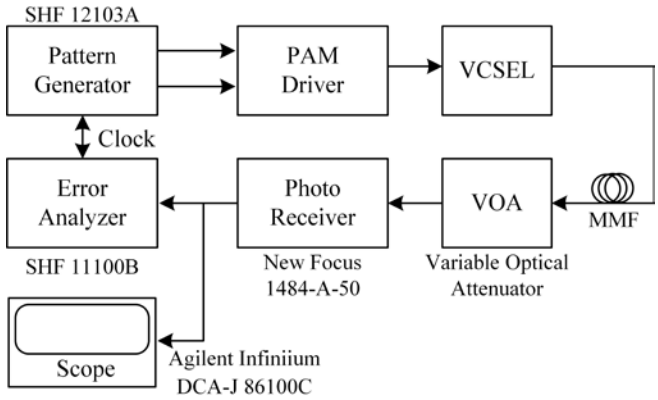

Figure 3.20: Experimental setup of the driver-integrated VCSEL link [D].

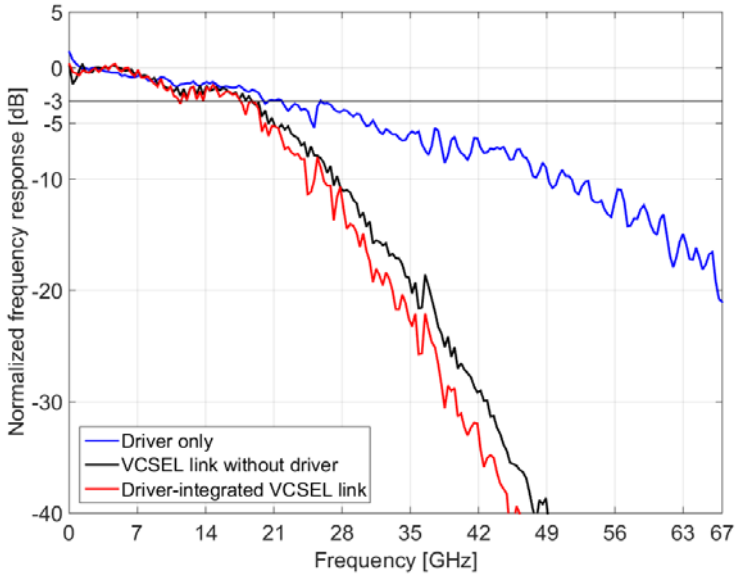

Figure 3.21: Measured frequency response of the driver, the link without driver and the link with driver [D].

Pre-emphasized PAM-2 optical transmission

Signal transmission over a bandwidth limited VCSEL link causes inter-symbol interference (ISI). To reduce the ISI, the electronic driver may pre-emphasize the driving signal to the VCSEL. In this way, it amplifies the high-frequency components (also known as peaking) of the signal to compensate for the high-frequency roll-off of the laser response.

Using two input channels of the driver, the integrated VCSEL transmitter can perform PAM-2 pre-emphasis using 1-tap feed-forward equalization (FFE). As illustrated in Fig. 3.22, 1-tap FFE pre-emphasis is realized by adding a delayed, inverted and weight-compensated copy of the signal to the signal itself, to generate overshoot at the transitions [37], [38]. The delay factor and the weight factor are chosen according to the channel characteristics [39].

Improved receiver sensitivity by applying transmitter pre-emphasis is quantified when comparing the transmission performance at the same data rates with and without pre-emphasis. As shown in Fig. 3.23, the pre-emphasis increases the error-free data rate from 44 to 47 Gbps. At 50 Gbps, the receiver sensitivity is improved by 2 dB at BER = 10^{-6}. The effect of pre-emphasis in the time domain can be understood as an enlarged eye opening at the expense of a reduced signal amplitude. Therefore, the performance gain is more pronounced at a high data rate, where the performance is mainly limited by the ISI rather than the signal power. Fig. 3.24 demonstrates the trade-off at 50 Gbps, where the pre-emphasized optical eye at the VCSEL output (d) has 60% more vertical margin than the corresponding eye without pre-emphasis (c); however, the amplitude is reduced to 78% of the original. The amplitude reduction is attributed to one part of the signal energy consumed to enhance the high frequencies, shown as the generated overshoot at the transitions when applying pre-emphasis to the driving signal (b).

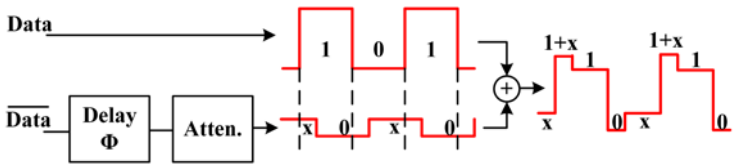

Figure 3.22: Signal generation using 1-tap FFE pre-emphasis, where the pre-emphasized signal is the sum of the original data and the inverted data with a time delay Φ and a weighted amplitude X [D].

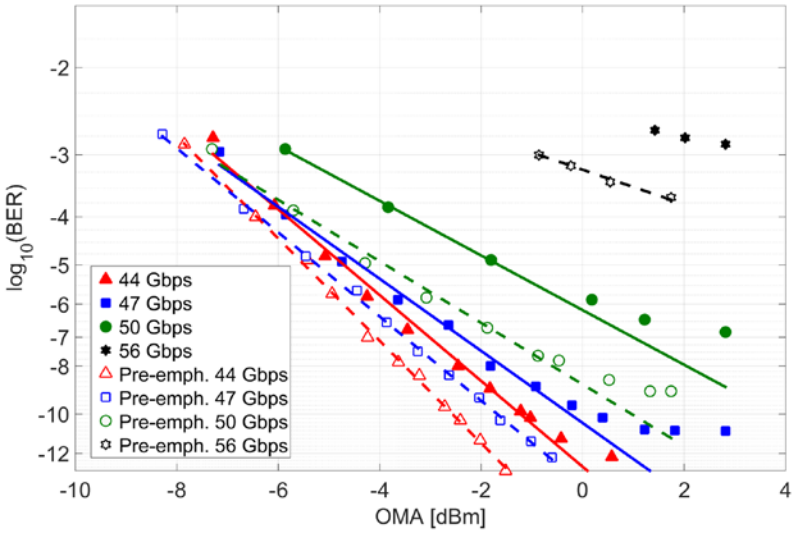

Figure 3.23: Performance comparison of pre-emphasized and non-pre-emphasized PAM-2 transmission [D].

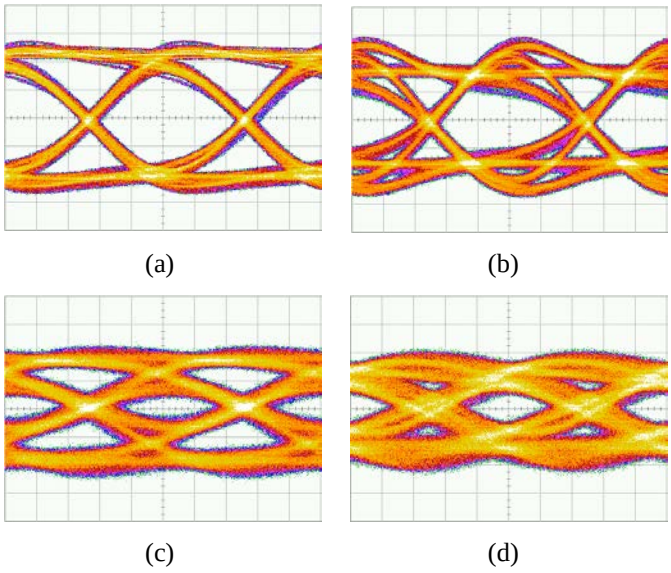

Figure 3.24: Captured eye diagrams in PAM-2 modulation at 50 Gbps (4 ps/div, 100 mV/div for (a) and (b), 50 mV/div for (c) and (d)). (a) driving signal to VCSEL without pre-emphasis (b) driving signal to VCSEL with pre-emphasis (c) VCSEL output without pre-emphasis, ER = 2.6 dB and (d) VCSEL output with pre-emphasis, ER = 2.0 dB [D].

PAM-4 optical transmission

As shown in Fig. 3.25, error-free PAM-4 optical transmission is achieved up to 56 Gbps, and an error floor at BER = 10^{-5} is reached at 64 Gbps. ISI penalty is obviously seen in the received optical eye diagrams in Fig. 3.26 (a) and (b), compared with the corresponding electrical eyes at the driver output (c) and (d). The impact of ISI is more pronounced in the outer eyes than the middle eye. The BER based on middle eye measurements is therefore an optimistic estimation for PAM-4 under the ISI penalty.

The main reason for the performance degradation in the optical link with respect to the stand-alone driver is believed to be caused by the limited link bandwidth. Significant performance gain is expected by applying PAM-4 pre-emphasis for bandwidth extension. Also, increasing the amplitude of the driving signal would enable higher data rates, as demonstrated in [40]. These proposed improvements are implemented in a new driver design in simulations. Simulation results in Fig. 3.27 show improved eye openings at 100 Gbps over the same optical link with less than 20 GHz bandwidth.

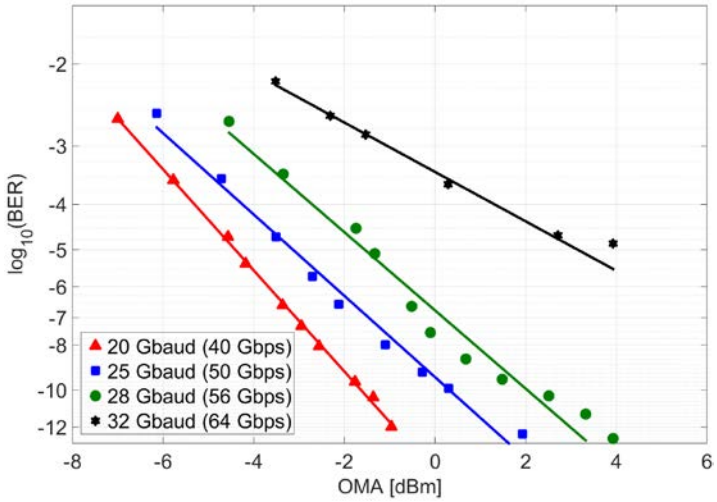

Figure 3.25: Measured BER as a function of received OMA in PAM-4 modulation from 40 to 64 Gbps [D].

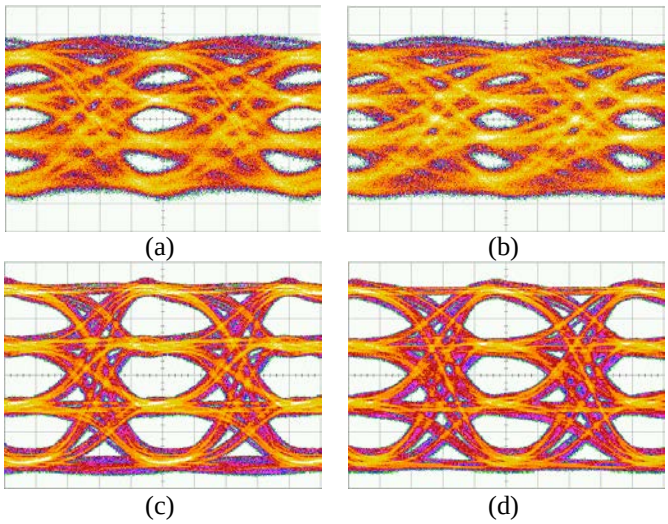

Figure 3.26: Comparing received PAM-4 eye diagrams (inverted) after optical transmission (a) 56 Gbps, 8 ps/div, 50 mV/div (b) 64 Gbps, 7 ps/div, 50 mV/div, with PAM-4 electrical eyes at the driver output (c) 56 Gbps, 8 ps/div, 100 mV/div and (d) 64 Gbps, 7 ps/div, 100 mV/div [D].

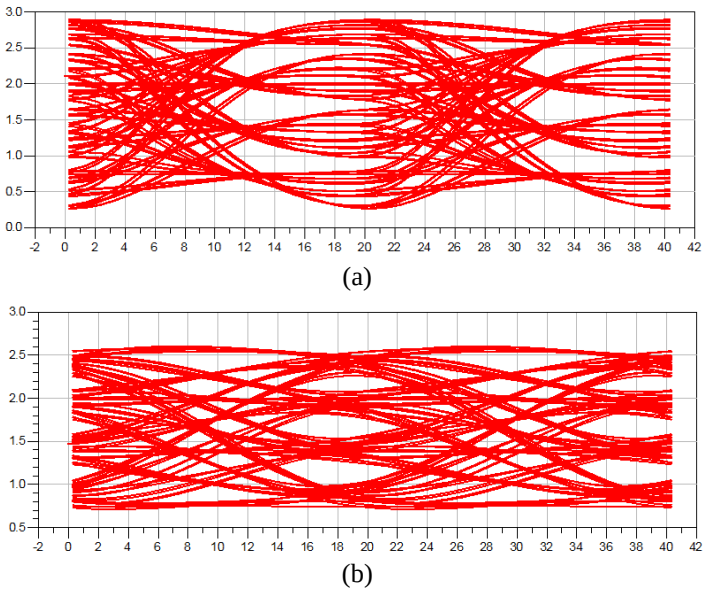

Figure 3.27: Simulated 100 Gbps PAM-4 eye diagrams, (a) at the driver output with pre-emphasis and (b) at the receiver output after band-limited optical transmission.

Chapter 4

Spectrally Efficient Communication

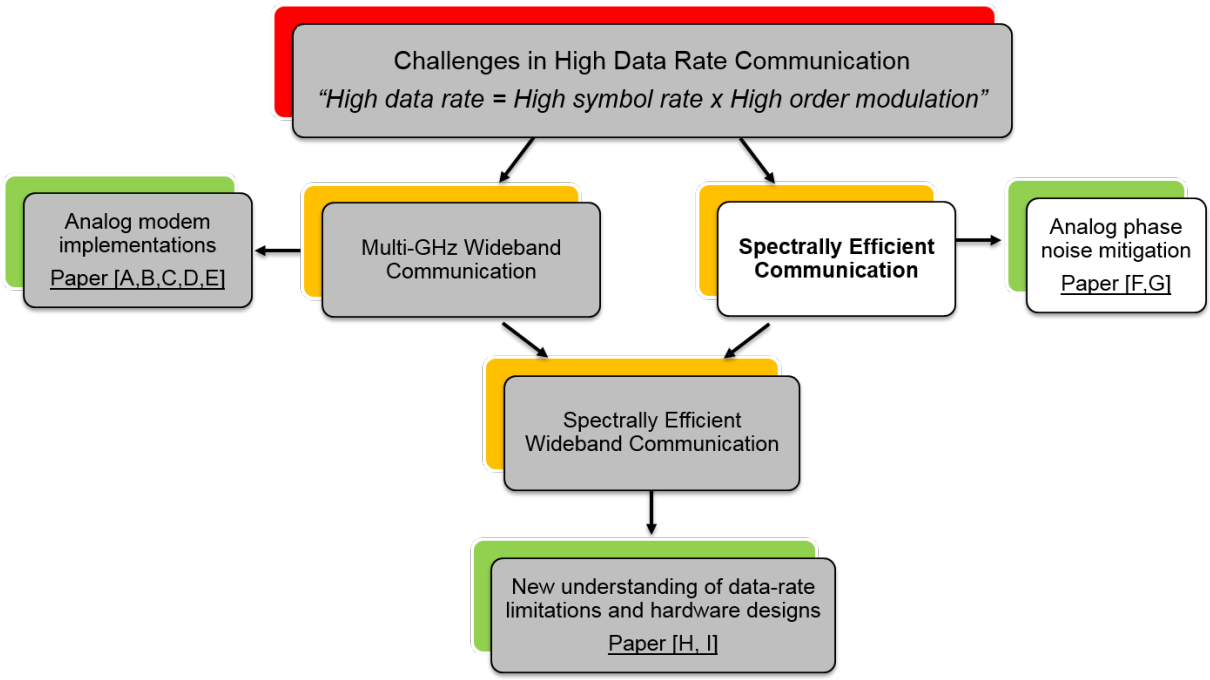

Figure 4.1: Thesis outline in block diagrams.

4.1 Phase noise limitation

Phase noise exists in all physical oscillators. It broadens the signal spectrum at the oscillation frequency to adjacent frequencies so that noise sidebands are formed. Phase noise is normally expressed in dBc/Hz, noise power relative to the carrier power within 1 Hz bandwidth, at a certain frequency offset from the carrier frequency.

Phase noise in local oscillators (LO) reduces the signal quality which in turn increases BER in wireless communication systems. The impact of phase noise on a communication signal is demonstrated in Fig. 4.2 (b), where the symbols of the constellation are spread in the angular direction. The symbols with the highest amplitude are affected the most.

Consequently, low phase noise is required for high-order QAM modulations to improve the spectral efficiency of a communication system, as indicated in Fig. 4.3 based on empirical phase noise requirements. It is also shown that the phase noise requirement is related to the channel bandwidth, and narrow-bandwidth systems demand a lower phase noise.

Today, off-the-shelf oscillators with acceptabe phase noise level are only available in the low GHz range due to technology and/or cost limitations. Therefore, frequency multipliers are often used for high-frequency signal generations. Unfortunately, when the frequency of a signal is multiplied by a factor of N, the phase noise is increased by $20\log_{10}(N)$ dB.

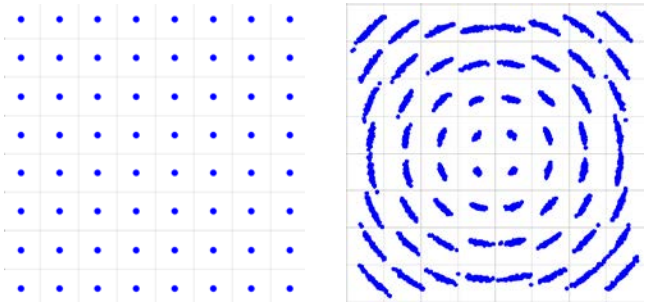

(a) (b)

Figure 4.2: Simulated QAM constellation diagrams, (a) ideal 64-QAM and (b) 64-QAM with phase noise.

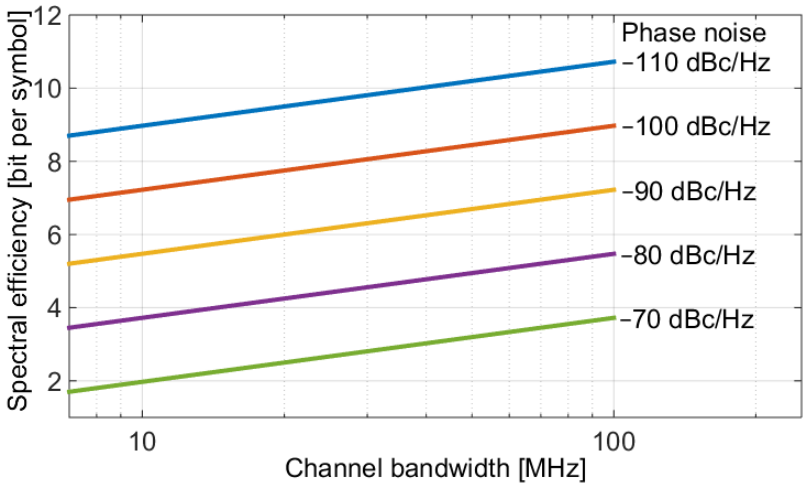

Figure 4.3: Phase noise requirements in relation to spectral efficiency and channel bandwidth, where the specified phase noise is at 100 kHz offset frequency. The plot uses empirical data and is valid for a constant SNR [41].

4.2 Phase noise reduction techniques

Due to technology limitations and cost issues, it is very challenging to maintain low LO phase noise at high frequencies, i.e. mm-wave and sub-mm-wave (>300 GHz). As an alternative, the impact of phase noise can be efficiently reduced. Digital phase tracking is a widely used solution in commercial radio systems for phase noise mitigation. Accurate estimation of phase noise is demonstrated in theoretical works using advanced tracking algorithms [42]. However, considering the computational complexity and power consumption of digital processors, mitigating phase noise is practically limited using digital tracking techniques.

To complement the conventional digital tracking, we discuss in the following subsections two different ways to deal with the remaining (residual) phase noise. It is particularly beneficial to high-frequency systems with inherently high phase noise.

Paper [F] presents an analog technique using an RF pilot-tone to cancel the phase and frequency errors introduced by high-frequency conversion. On the other hand, constellations can be designed to tolerate more phase noise than the traditional square QAM does.

4.3 Phase noise robust spiral QAM constellations

A new spiral QAM modulation scheme is proposed in [j]. It allows optimization of the constellation design for a given residual phase noise of the system, and therefore minimization of the phase noise impact on communication performance. As opposed to square QAM, the superior performance of the spiral QAM modulation is verified through numerical simulations as well as experiments in a mm-wave transmission setup.

4.3.1 Constellation construction

A *M*-order spiral QAM constellation (SQAM) is constructed by placing *M* symbol points along a spiral line. The complex coordinate of the *m*-th point can be expressed as [j]

$$c_m = I_m + jQ_m = t_m e^{jt_m} \tag{3.1}$$

$$t_m = \sqrt{\frac{(4\pi m)^2 R}{2} + \sqrt{\frac{(4\pi m)^2 R^2}{4} + (4\pi m)^2}}\,, \tag{3.2}$$

where m=1,2,….M, and R is an arbitrary number that is chosen according to the amount of residual phase noise. Fig. 4.4 illustrates the distribution of 64-point SQAM constellation for various R values. When R is equal to 0, the distance between constellation points is nearly constant. This constellation is suitable for AWGN channels, in a similar way as square QAM. In a phase noise dominant channel, the constellation points far from the center suffer more angular noise than those close to the center. With an increased R, the angular distance between adjacent constellation points is increased proportionally to the distance to the center. In this way, good margin for detection is introduced, minimizing errors caused by phase noise.

4.3.2 **Demodulation**

Two different demodulation methods are discussed in [j], Minimum Euclidean Distance (MED) and Phase Noise Optimized Distance (PNOD). As an example, taking a SQAM constellation with R = 0.01, Fig. 4.5 shows the decision region for the corresponding demodulation method, (a) PNOD and (b) MED. Each color represents an area, where the same decision is made for the received symbols. Compared to the MED optimized for AWGN channels, the PNOD with the decision region in an arc shape is applicable to phase noise limited channels.

The performance of the spiral QAM (SQAM) constellations is evaluated in simulations, where square 64-QAM and 64-SQAM are compared. Simulation results are shown in Fig. 4.6 as symbol error rate (SER) versus SNR per symbol. In an AWGN channel, SQAM achieves the same performance as QAM. When certain amount of phase noise is added, in this case, noise

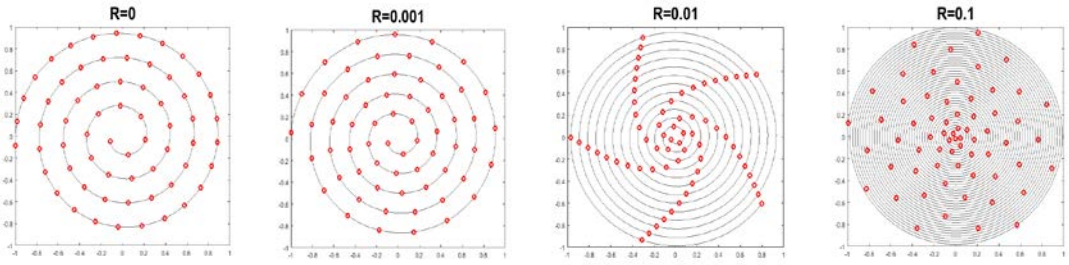

Figure 4.4: 64-point spiral QAM constellations with different R values in eq. (3.2) [j].

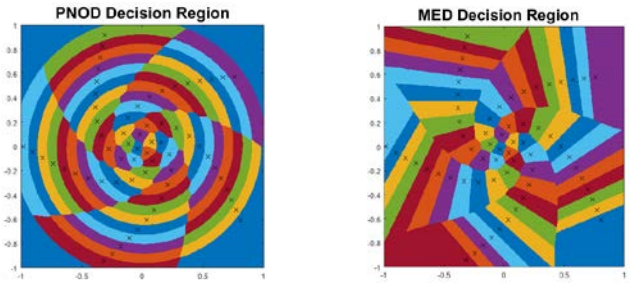

(a) (b)

Figure 4.5: 64-point spiral QAM decision region for the corresponding demodulation method, (a) PNOD and (b) MED [j].

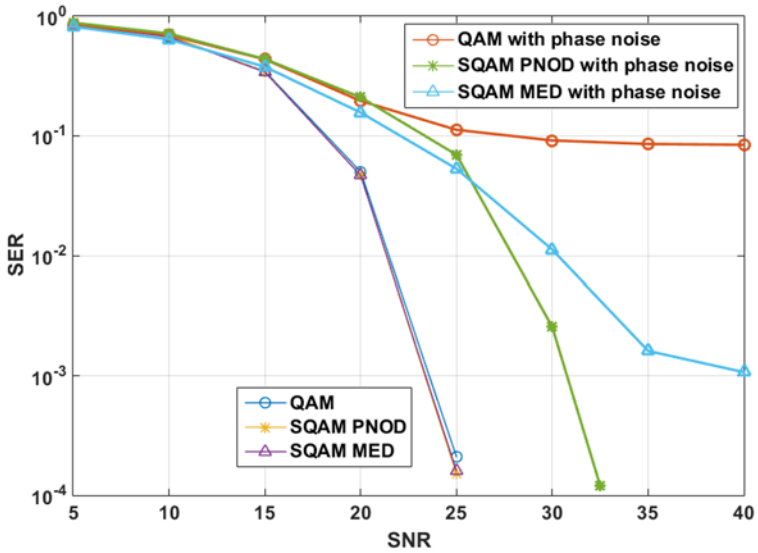

Figure 4.6: Simulated SER performance versus SNR for 64-QAM and 64-spiral QAM with added phase noise equal to noise variance of 0.01 [j].

variance of 0.01, QAM suffers from a high SER floor, while SQAM even with a simple MED detection outperforms QAM significantly. At higher SNR (>25 dB), PNOD detection gives a better performance than the MED detection. It is confirmed by simulations that the SQAM is more robust against phase noise.

4.3.3 Millimeter-wave experimental demonstration

The 64-spiral QAM transmission is demonstrated in a mm-wave experimental setup shown in Fig. 4.7. The transmission performance is compared among 64-QAM, 64-SQAM with two different constellation constructions. An arbitrary waveform generator (AWG) is used to generate modulated IF signals at symbol rate of 20 MBaud and 40 MBaud. The IF signal is up- and down-converted by mm-wave transceivers at 70/80 GHz (E-band). The transceivers are driven by independent LO sources and are connected using an adjustable waveguide attenuator. By tuning the attenuation, the received SNR is kept the same for all the measurements. The down-converted IF is received by a real-time oscilloscope, where demodulation is performed using Keysight VSA software. Error vector magnitude (EVM) and bit error rate (BER) are the measures used to compare the performance of different constellations.

Fig. 4.8 displays screen-shots from the oscilloscope showing the demodulated constellations at 20 MBaud. The measured EVM is of the same order for both QAM and SQAM2 (R=0.001) due to phase rotations, caused by phase noise. However, the SQAM2 constellation provides a significantly lower BER than QAM. Comparing the two SQAM constellations, SQAM1 (R=0.1), with outer constellation points well separated, can tolerate phase noise but suffers heavily from additive noise due to its densely packed inner points. On the other hand, SQAM2 constellation has the inner and outer points placed in an optimized way, to handle both AWGN and phase noise to some extent.

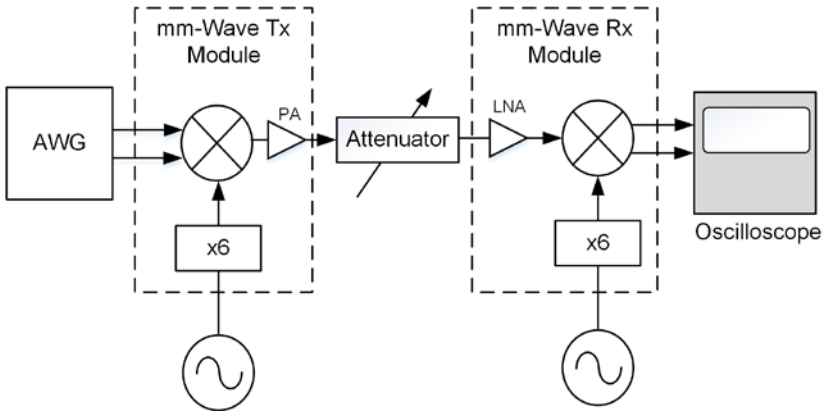

Figure 4.7: Block diagram of the mm-wave experimental setup [j].

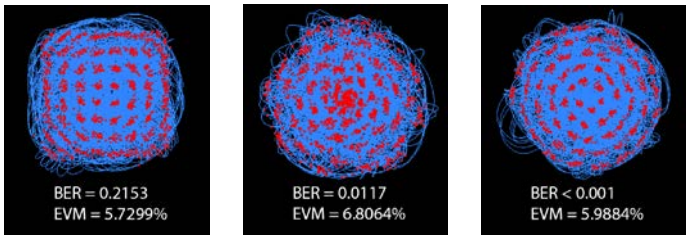

(a) (b) (c)

Figure 4.8: The demodulated signal constellation at 20 MBaud, (a) 64-QAM, (b) 64-spiral QAM when R is 0.1, and (c) 64-spiral QAM when R is 0.001 [j].

Discussion

For systems with high symbol rates, communication performance is more influenced by white LO noise than the near-carrier phase noise. Consequently, as the symbol rate is increased from 20 MBaud to 40 MBaud, the performance improvement offered by the SQAM starts to saturate, i.e. 10 times lower BER compared to the QAM [j]. The preferred system scenario, where SQAM has a clear performance advantage as compared to QAM, would be at relatively low symbol rate, i.e. <50 MBaud, with high SNR, i.e. >25 dB.

4.4 Analog phase noise mitigation

An analog phase noise mitigation method is proposed in paper [F]. As opposed to the digital counterpart, the analog technique is applicable to arbitrary signal waveforms. It is an attractive solution to enable transmission of phase-noise sensitive signals over high frequency carriers. The method is experimentally verified at mm-wave frequencies showing significant noise reduction within 100 kHz offset from the carrier.

Possible application scenarios are as follows: a complement to the existing digital phase tracking technique for improved transmission performance, e.g. higher data rates; alternatively, enabler for reduced hardware cost by relaxing the phase noise requirement of high frequency front-ends.

4.4.1 Principle of analog phase noise mitigation

Fig. 4.9 illustrates the principle of analog phase noise mitigation in a heterodyne radio link. A low power RF pilot-tone is added next to an arbitrary signal on the transmitter side at the intermediate frequency (IF) stage. The pilot tone is co-transmitted with the data signal over a mm-wave channel so that it is distorted in the same way as the signal by phase noise and frequency offset due to frequency up and down conversions at the mm-wave domain. Thus, the pilot tone can be used as a phase reference at the receiver to restore the signal through noise cancellation. The pilot tone can be placed in the middle of the signal spectrum [43] or next to the signal with a small frequency separation at the cost of extra bandwidth [44]. Inserting a pilot in the middle of the signal does not consume extra bandwidth, but it demands increased linearity from the transceiver hardware to minimize signal distortion.

One possible receiver implementation for the phase noise mitigation is shown in Fig. 4.9. The received signal is first down-converted from mm-wave to an IF frequency f_{IF}, then the signal is split into two branches. A narrow band pass filter (BPF) is placed in one branch to select the pilot, which is multiplied with the signal on the other branch using a frequency mixer. At the mixer output, the phase and frequency impairments introduced over the mm-wave transmission are cancelled for the down-converted signal at f_{IF}-f_p, while the image frequency f_{IF}+f_p carries doubled impairments due to noise addition. The image frequency can be removed by filtering, or simply by using a single sideband mixer. Power amplification of the selected pilot tone is often needed to ensure a sufficient dynamic range for the noise reduction. Finally, the restored signal, if required from a system perspective, can be converted back to the original frequency f_{IF} through an additional frequency conversion.

4.4.2 Experimental demonstration over millimeter-wave

As a proof-of-concept demonstration, experiments are carried out at both 28 GHz and at 73 GHz (E-band) using commercial components. In the measurement setup, a sinusoidal signal is transmitted as the carrier signal without modulated data in order to directly characterize phase noise improvements using a spectrum analyzer. For comparison, phase noise of the carrier signal is measured at the output of the mm-wave Rx at f_{IF} (point A in Fig. 4.9) and at the output of the noise cancellation mixer (point B in Fig. 4.9). The measured results are displayed in Fig. 4.10, where phase noise is presented in dBc/Hz versus frequency offset from the carrier. At both 28 GHz and the E-band, the pilot-based mitigation method demonstrates more than 20 dB noise reduction within the 100 kHz offset and more than 30 dB reduction at 10 kHz offset.

The purpose of the first experiment is to prove the noise mitigation concept with relaxed requirements on spectral efficiency and hardware performance. For instance, the BPF is chosen upon availability, so that the bandwidth is not optimized for the best achievable noise reduction.

4.4.3 Performance optimization

There are two critical design parameters to optimize in order to achieve the best possible phase noise performance: the bandwidth of the BPF for selecting the pilot tone and the pilot-to-signal power ratio (PSPR) [F].

The optimal filter bandwidth shall be defined for a given phase noise figure of the oscillator [43]. Higher phase noise increases the spectrum spreading of the pilot, and thus a wider filter is needed to capture the noise-contaminated pilot. In order to minimize bandwidth overhead,

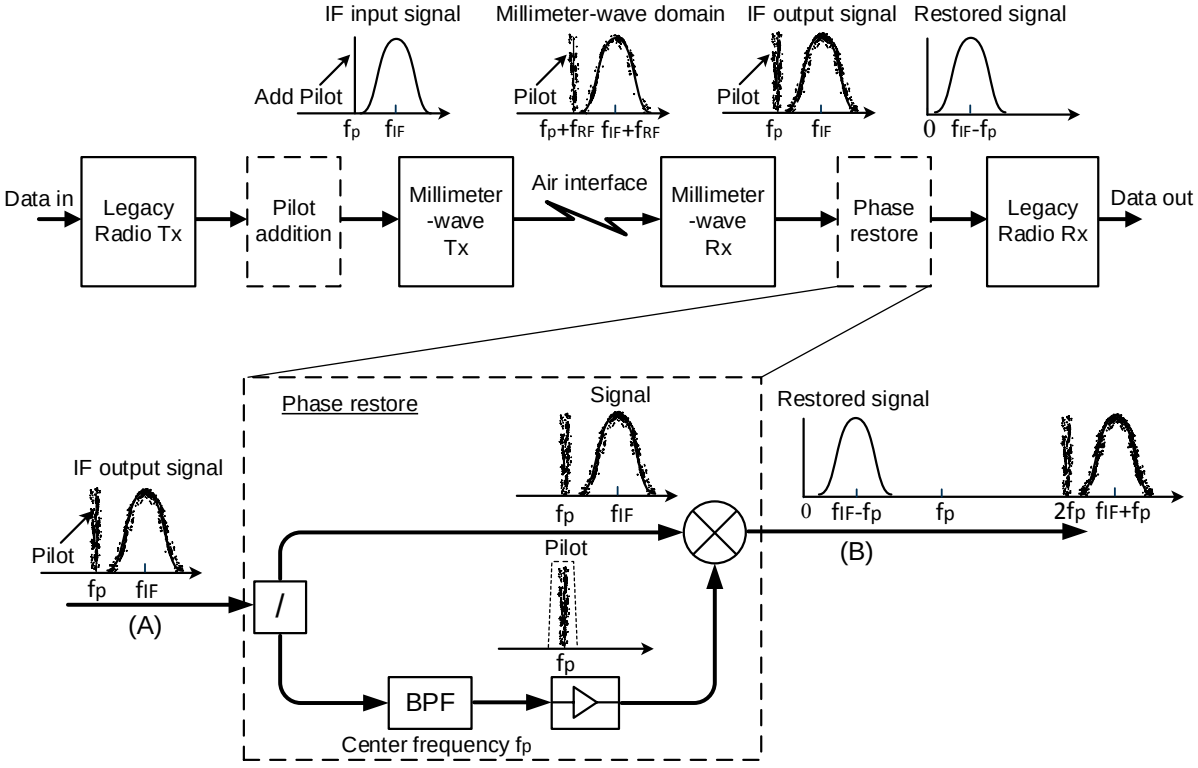

Figure 4.9: Illustration of the pilot-based phase noise mitigation principle in a heterodyne millimeter-wave radio link, and one possible phase-restore implementation at the receiver [F].

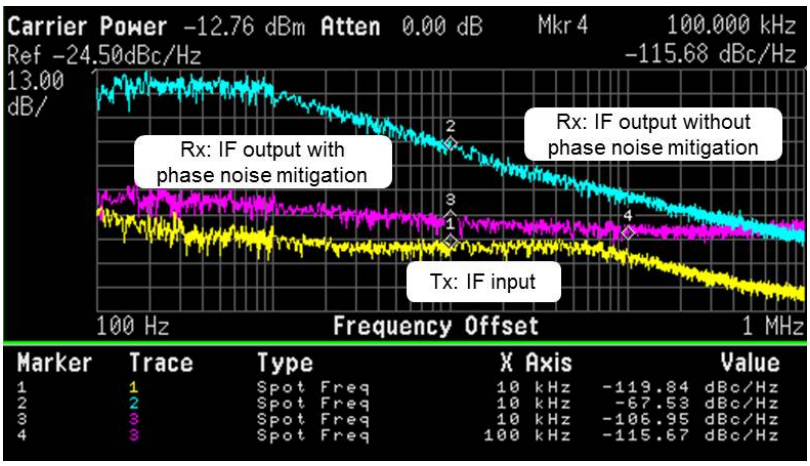

(a)

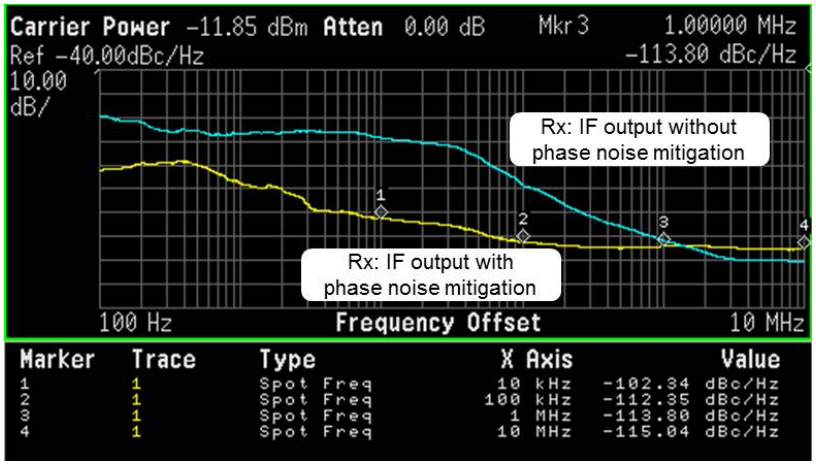

(b)

Figure 4.10: Measured phase noise of the received IF carrier signal before and after the pilot-based phase noise mitigation (a) over the 28 GHz band, and (b) over E-band at 73 GHz [F].

however, the pilot shall be placed as closely as possible to the signal spectrum, and consequently the filter shall be relatively narrow. In practice, the chosen filter bandwidth is a trade-off between spectral efficiency and phase noise performance. The degree of phase noise reduction also depends on the power of the pilot. On the one hand, the pilot shall be kept at a low power level to fulfil the spectrum mask requirement. On the other hand, it cannot be too weak so that the SNR of the pilot starts to limit the noise reduction. In practice, the pilot should be implemented with automatic gain control to compensate for gain variation in a frequency-selective radio channel.

4.5 Millimeter-wave fronthaul system demonstration

The analog phase noise mitigation can potentially be a technology enabler for mobile communications using mm-wave frequencies, as proposed for next generation radio access networks (5G). In paper [G], we demonstrate an analog fronthaul link as a new system application, complemented by the analog phase noise mitigation.

4.5.1 Digital fronthaul vs. analog fronthaul

A digital fronthaul link transports multi-gigabit digital CPRI information between the baseband unit and the remote radio unit at the cell site. Due to the demanding data-rate requirements, optical fibers are often used for digital fronthaul links. Thanks to the available wide bandwidth, digital wireless fronthaul is a feasible alternative as demonstrated in [C] and [f] using 70/80 GHz (E-band). However, even using a spectrally efficient modulation (e.g. 64-QAM), digital fronthaul still requires at least a few hundreds of MHz bandwidth for 2.5 Gbps CPRI transmission to support one LTE sector. Low bandwidth efficiency is considered to be the main drawback of digital wireless fronthaul, which can be the bottleneck for deploying fronthaul in future networks.

As opposed to digital wireless fronthaul, analog wireless fronthaul as a new solution is presented in [G]. The basic idea is to carry narrow-band analog radio access signals i.e. 20 MHz LTE signal over the air instead of multi-gigabit CPRI data. This method is much more bandwidth-efficient and therefore is scalable to future data-rate upgrades. The hardware implementation of an analog fronthaul link is different from the digital fronthaul, as illustrated in Fig. 4.11 using the main functional blocks. The analog fronthaul relays a radio signal between the BBU and the RRU. The RRU can be simplified to contain only the radio front-end for frequency up-/down- conversion and RF power amplifiers. The power-hungry data converters (DAC/ADC) are no longer needed, which reduces the power consumption at the cell site as compared to a conventional RRU for the digital fronthaul.

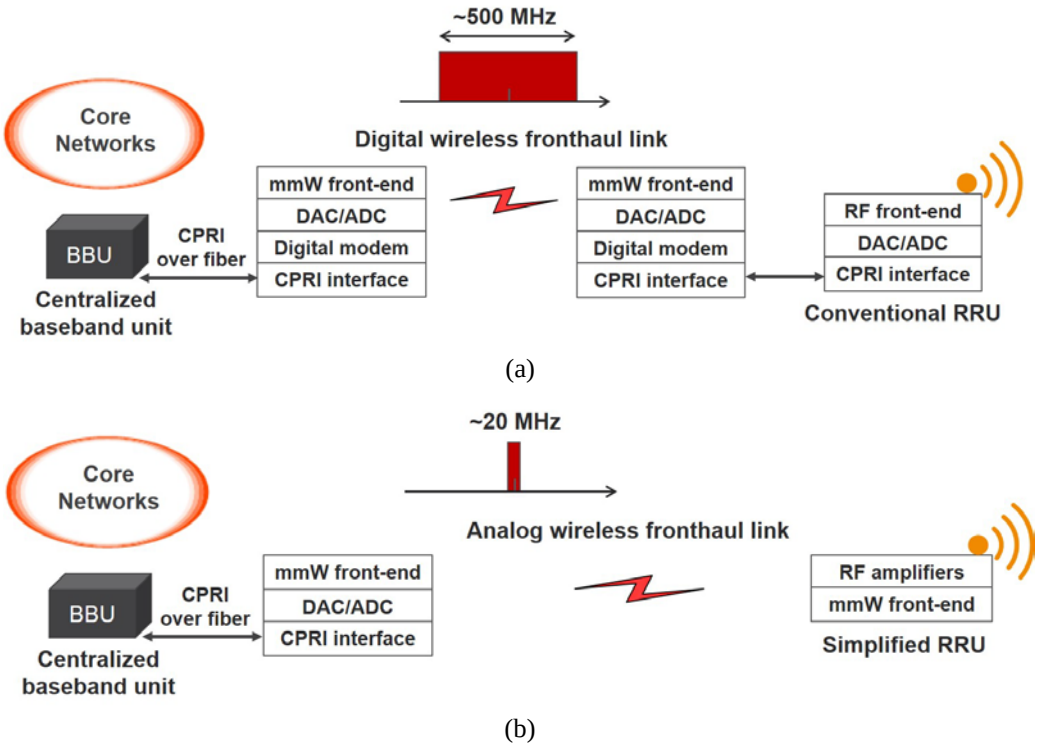

Figure 4.11: Comparison of end-to-end fronthaul link implementations, (a) digital wireless fronthaul, and (b) analog wireless fronthaul [G].

4.5.2 Analog fronthaul – advantages and challenges

Fig. 4.12 shows a potential application of using point-to-point analog fronthaul links to deploy small cells (RRUs) for capacity and coverage enhancement of a macro site. Each RRU supported by the analog fronthaul can be configured for one specific service or multi-service (i.e. 2G/3G/4G/Wi-Fi) thanks to transmission of analog radio signals, while the digital fronthaul transmission typically only supports one service at a time. Moreover, the analog fronthaul, being a bandwidth-efficient solution, is data-rate scalable by frequency multiplexing multiple narrow-band radio signals. For the RRUs not situated in line-of-sight relative to the macro radio base station (e.g. RRU4 in Fig. 4.12), the fronthaul connection is established by distributing radio signals through several line-of-sight links, in a daisy chain fashion.

The concept of analog fronthaul can be realized at various frequencies. The mm-wave bands are most attractive due to large bandwidth available for carrier aggregation to enable high link capacity. In addition, it reduces costs for operators to deploy mm-wave links using the license-free 60 GHz band or the light-licenced 70/80 GHz band (E-band). However, radio impairments such as phase noise and frequency error increase proportionally to the carrier frequency. For instance, the phase noise increases as much as 30 dB when the carrier frequency is shifted from 2.6 GHz to 80 GHz. The baseband digital signal processing in conventional radio base stations and user terminals (e.g. mobile phones) is not designed to handle such high frequency impairments. Hence, the additional impairments induced by the mm-wave fronthaul link must be minimized to maintain the performance of the radio access signals, so that users do not experience any degradation in service quality.

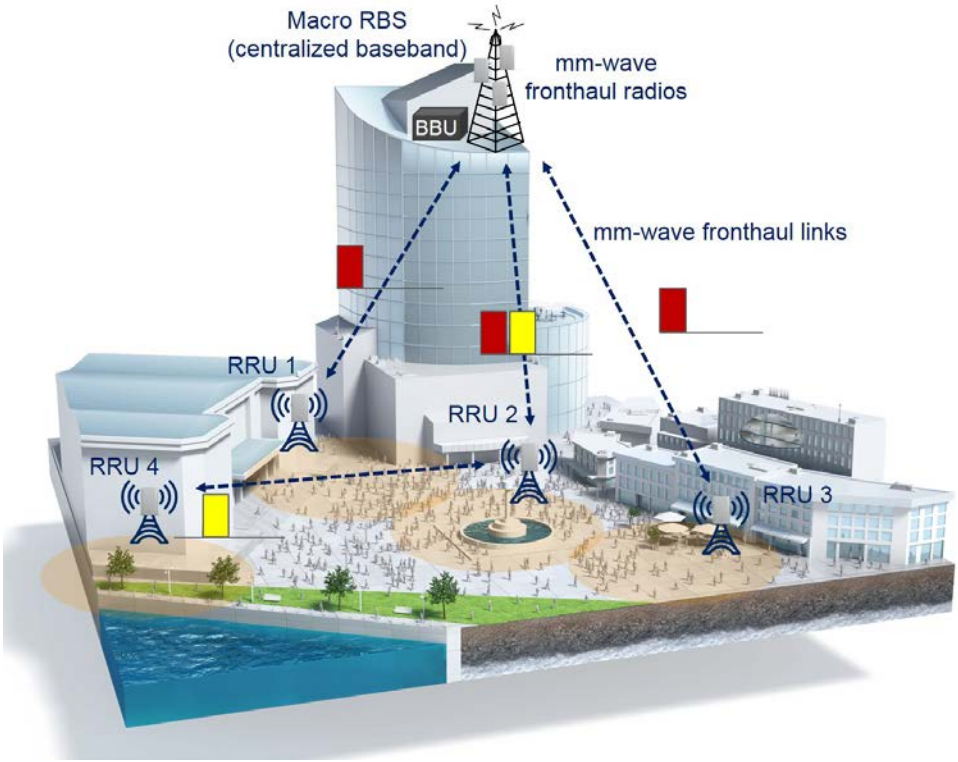

Figure 4.12: Deployment of analog mm-wave fronthaul links from/to a macro site [G], where different RRUs could use different sub-bands.

4.5.3 Implementation of analog fronthaul at 70/80 GHz

To demonstrate the feasibility of analog mm-wave fronthaul, a test link is designed and implemented at the 70/80 GHz band (E-band) with pilot-based phase noise mitigation applied to restore the signal at the receiver. Enabled by the noise mitigation, 20 MHz 64-QAM LTE uplink and downlink transmission is demonstrated over E-band with measured error vector magnitude (EVM) of about 3%. Furthermore, the impact of the pilot overhead (required frequency separation between the pilot and the signal) and the pilot power level on transmission performance is also investigated.

The analog fronthaul link is implemented using commercial RF components and mm-wave front-end modules. Fig. 4.13 depicts the experimental setup of the fronthaul link, where LTE signal constellations are displayed at different transmission stages. At the transmitter side, LTE uplink and downlink signals are generated from a vector signal generator. The received signal quality is evaluated in a signal analyzer, which demodulates the LTE signals digitally and measures the EVM as the performance indicator. A BPF with 2 MHz bandwidth is chosen as an acceptable trade-off between spectral efficiency and performance. To avoid cross-talk between the signal and the pilot, the required frequency separation in-between (pilot-signal spectrum separation) is optimized, as well as the pilot-to-signal power ratio (PSPR). For OFDM-based LTE downlink transmission, Fig. 4.14 shows the impact of these two parameters on the received signal EVM, measured after the noise mitigation. Considering the trade-offs between performance and spectral/power efficiency, pilot-signal separation of 4 MHz and PSPR of -10 dB are chosen for the fronthaul link demonstration.

4.5.4 End-to-end link demonstration

As shown in Fig. 4.15, an end-to-end demonstration (the connection between a mobile terminal, i.e. a laptop, and the core network) is realized using the analog fronthaul link, where the LTE up-/down-link signals are transmitted in frequency division duplex scheme over the E-band's low band (centered at 73 GHz) and high band (centered at 83 GHz), respectively. Service quality in terms of up-/down-link speed is evaluated at the mobile terminal and no performance penalty is detected.

The fronthaul link budget is described in Table III for the given implementation. Maximum link distance is limited to 500 meters. To improve the link distance and/or availability, the easiest way is to use bigger antennas with more gain, e.g. 43 dBi instead of 38 dBi that was used. Besides, the Tx output power can also be increased by applying linearization techniques to the power amplification at the Tx front-end.

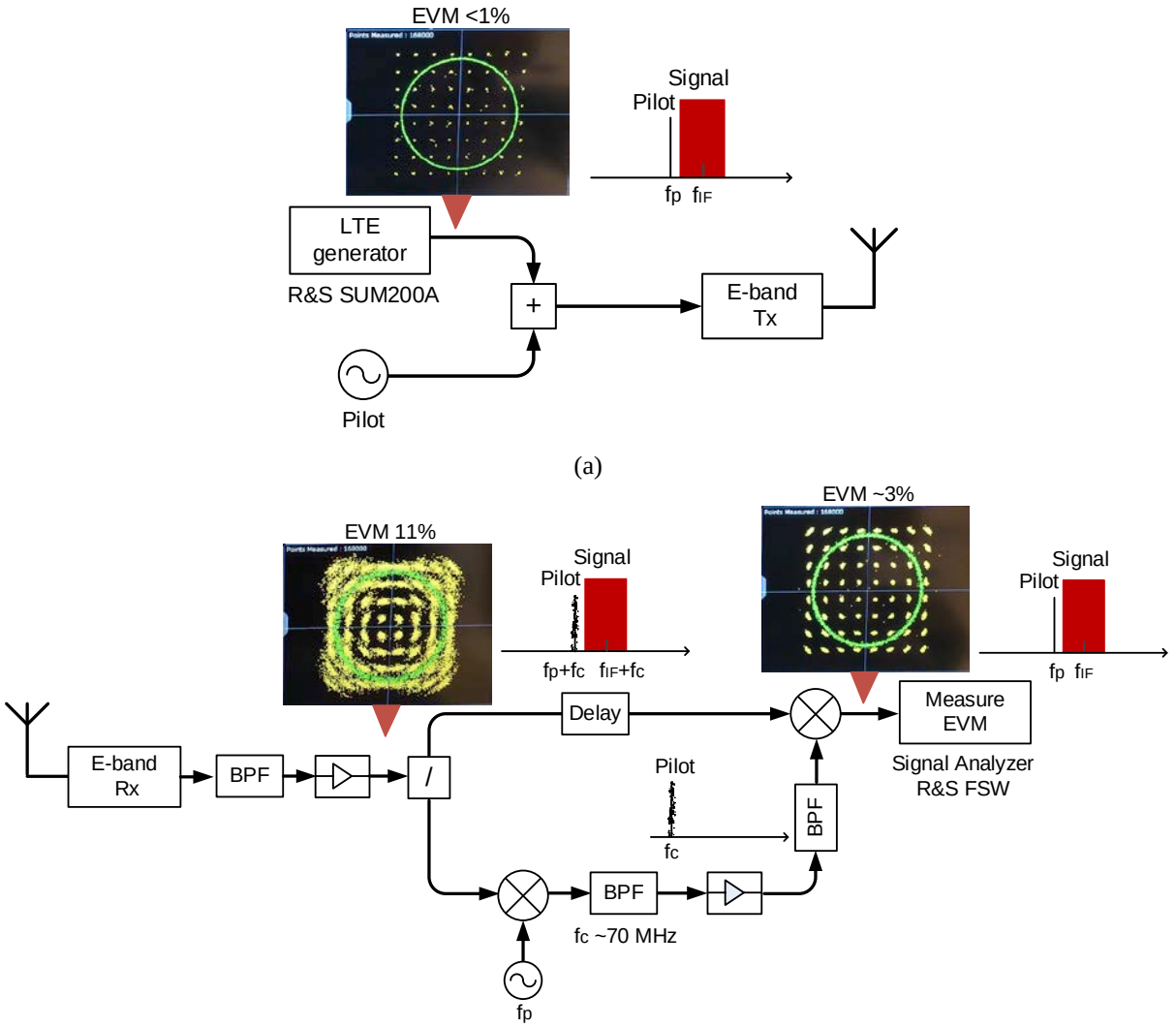

Figure 4.13: Experimental setup of the analog fronthaul link, (a) transmitter with an RF-pilot added, and (b) receiver with the pilot-based phase noise mitigation [G].

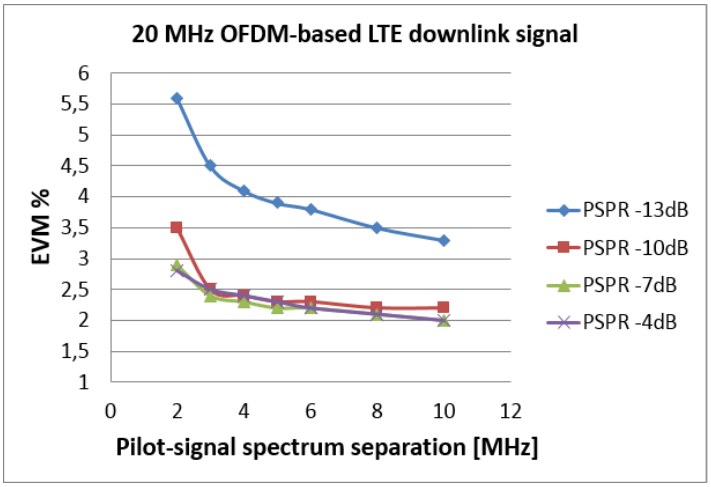

Figure 4.14: Impact of pilot-signal separation on signal quality in measured EVM at different pilot power levels [G].

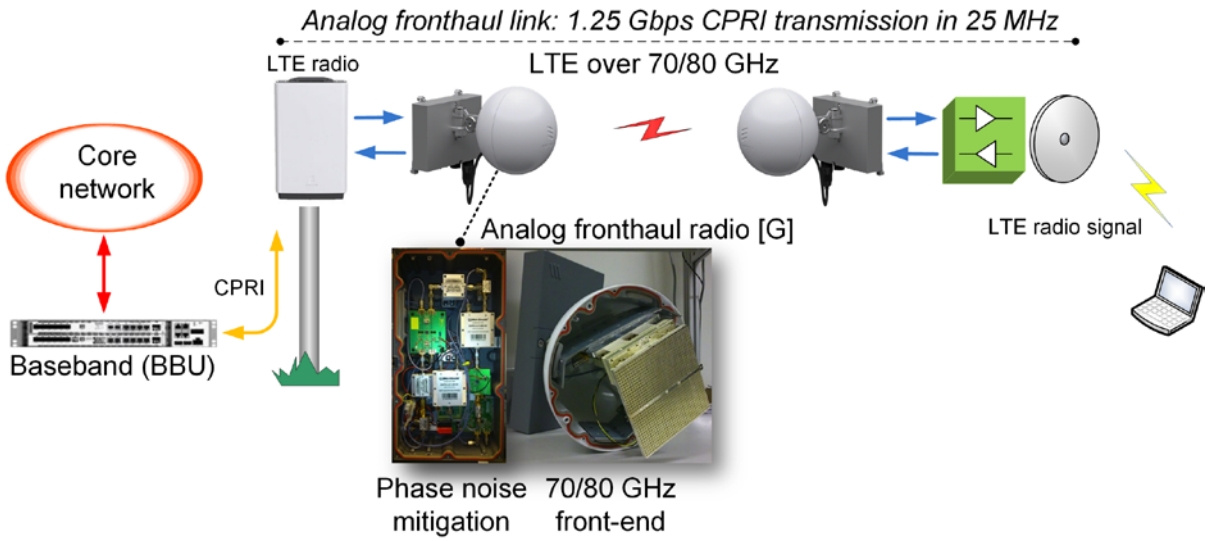

Figure 4.15: End-to-end demonstration of LTE transmission over analog fronthaul link at 70/80 GHz.

Table III: Link budget analysis for the analog fronthaul demonstrator [G].

Tx output power	5 dBm
Tx/Rx antenna gain (dBi)	38 dBi
Rx sensitivity for 3% EVM	−53 dBm
System gain	134 dB
Link margin	10 dB
Link distance	0.5 km

Chapter 5

Spectrally Efficient Wideband Communication

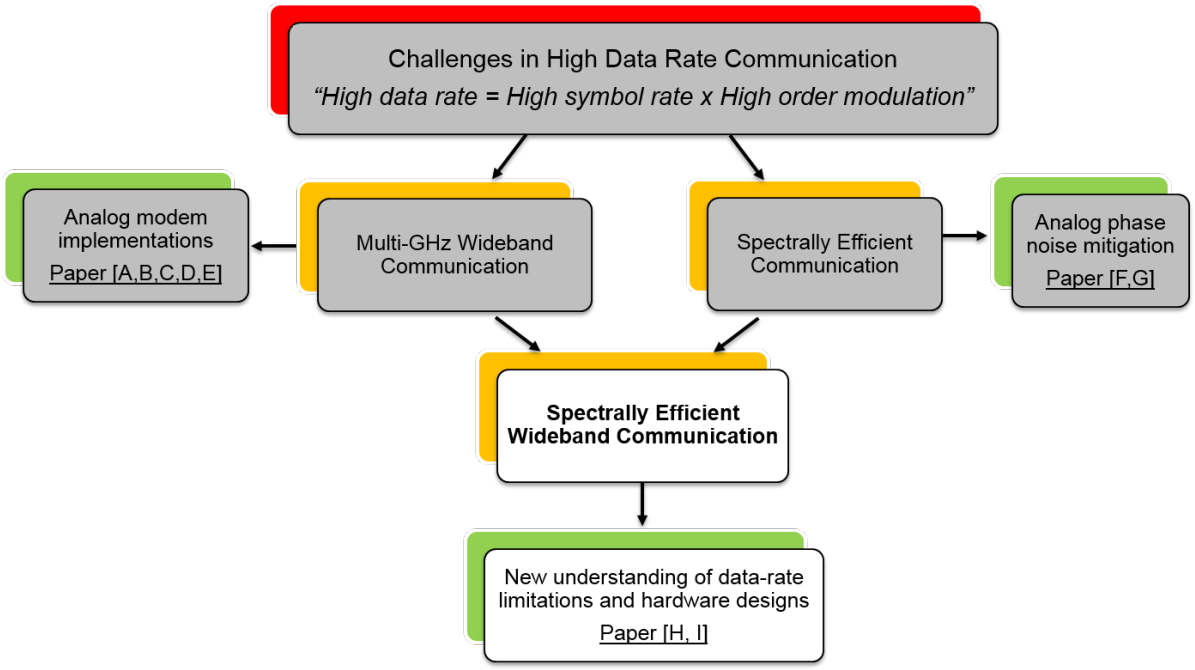

Figure 5.1: Thesis outline in block diagrams.

5.1 Implementation challenges

The combination of high-order modulation and wide modulation bandwidth provides extremely high data rate potential in mm-wave communication. However, it has been challenging to realize this combination in practice. Fig. 5.2 summarizes state-of-the-art transmission experiments beyond 100 GHz carrier frequency in a single-channel setup [5], [15–16], [18], [25–26], [45–49]. Transmission performance is presented as spectral efficiency in [bits per symbol], with respect to modulation bandwidth in symbol rate [GBaud]. The resulting data rate is the product of the two parameters.

Two categories can be observed as highlighted in the figure: high data rate realized using relatively simple modulations and thus very large bandwidths, such as 96 Gbps 8-QPSK transmission in 32 GBaud [5]; on the other hand, spectrally efficient 64-QAM modulations reported at lower data rates due to small bandwidths, i.e. at maximum data rate of 60 Gbps in 10 GBaud [45]. To the best of the author's knowledge, no single experimental demonstration has as yet been reported that simultaneously achieves large bandwidth and high-order modulation. To fully exploit the large bandwidth available, it is necessary to understand the practical limitations that prevent this combination from being successfully achieved.

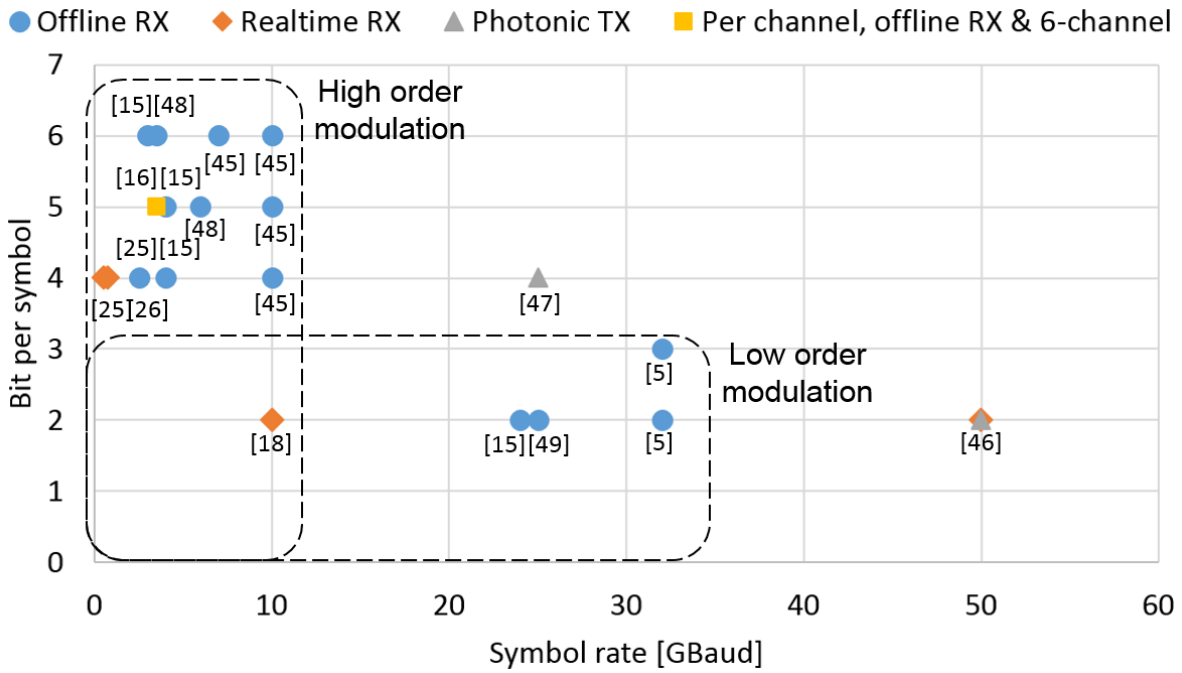

Figure 5.2: Published state-of-the-art single-channel transmission experiments beyond 100 GHz carrier frequency [I].

5.2 Hypothesis of white LO noise limitation

5.2.1 Introduction to LO noise

A typical single sideband phase noise spectrum of an oscillator is illustrated in Fig. 5.3. It can be divided into near-carrier phase noise with −30 and −20 dB/decade slopes and white noise floor. As already discussed in Chapter 4, the near-carrier phase noise limits the available modulation order in narrow band systems with low symbol rates. In mm-wave systems where the symbol rate is considerably high, communication performance is determined by the white noise floor rather than the near-carrier phase noise [50]. Therefore, a recent theoretical study concludes that the practical data rates in mm-wave and sub-mm-wave systems are limited by the LO noise floor [51]. However, only the phase noise is considered on the LO noise floor, known as white phase noise. In current models used for communication systems, LO noise is typically modelled as the sum of near-carrier phase noise and white phase noise [50], and both cause angular spreading in the constellation.

On the other hand, recently reported constellations from wideband mm-wave transmission measurements indicate the white LO noise with different properties. The example presented in Fig. 5.3 is a 10 Gbps 64-QAM constellation measured over E-band [52]. The distortion of the constellation is observed as circular clouds around each symbol, in contrast to angular spreading due to phase noise only. Based on the experimental observation, we believe that the LO noise floor consists of both phase and amplitude noise, which is defined as white (LO) noise in our recent study [H], [I].

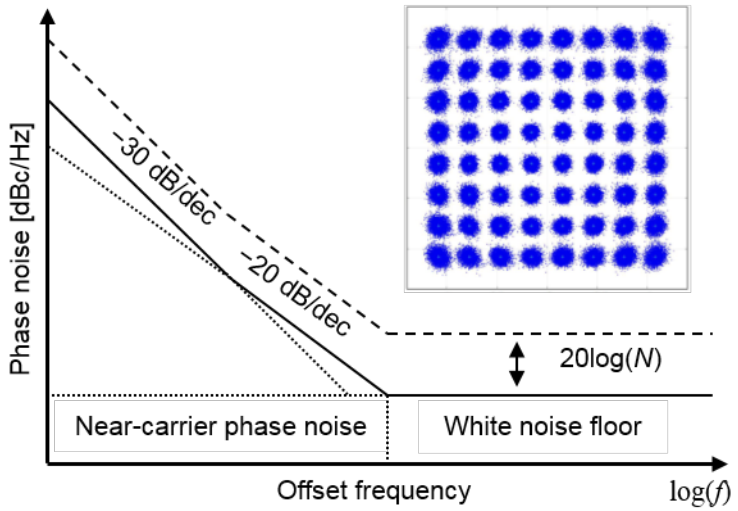

Figure 5.3: Single sideband phase noise spectrum of a typical oscillator, where the dashed line indicates noise degradation by $20\log_{10}(N)$ due to frequency multiplication. The inserted constellation is a 10 Gbps 64-QAM measured over E-band [52].

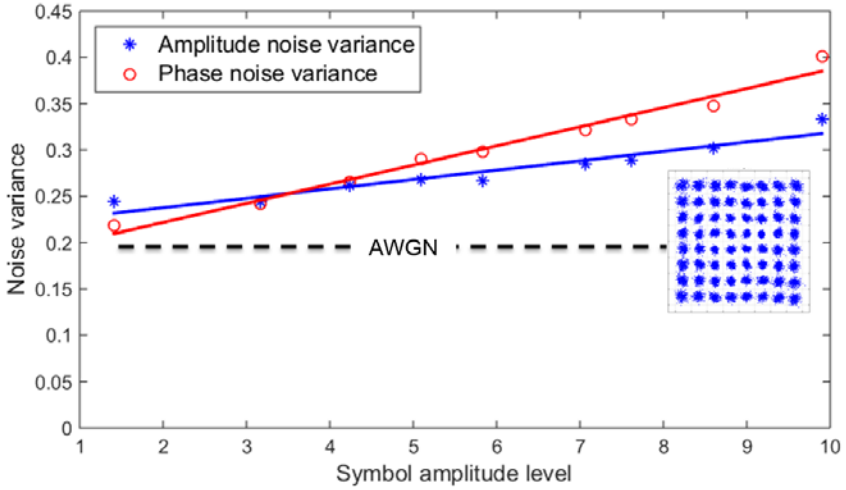

(a)

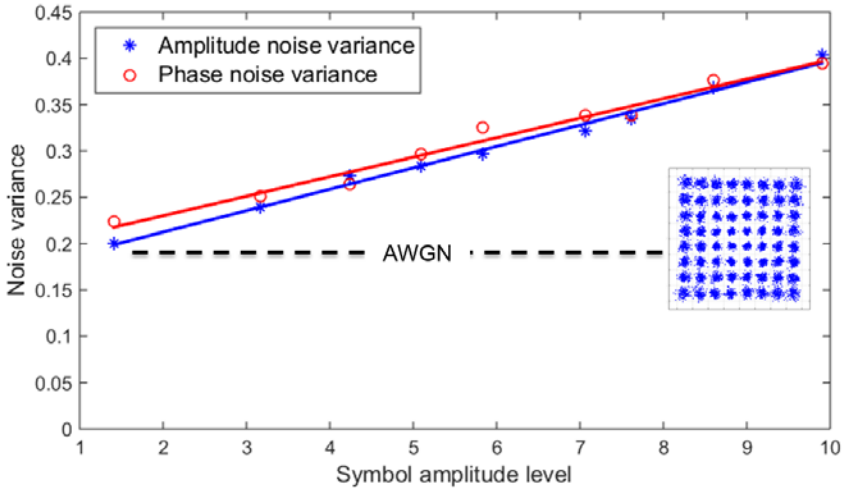

(b)

Figure 5.4: Computed noise variance in standard deviation versus 64-QAM symbol amplitude on measured 1 GBaud IQ data from inserted constellations, (a) normal LO driving power and (b) low LO driving power [I].

5.2.2 Proof of white LO noise properties

As a quantitative verification of the white LO noise properties, noise source analysis is performed on measured 64-QAM signals through frequency conversion [I]. Taking the IQ data, the amount of noise on each symbol is extracted and divided into phase and amplitude noise components, and the corresponding noise variance is computed using the standard deviation. Two sets of IQ data are analyzed using the same LO at the noise floor of −112 dBc/Hz, while the LO driving power is varied. One set of data is collected at +7 dBm (normal LO power) as required by the frequency mixer, and the other set is taken from +4 dBm (low LO power). The noise variances computed for the two cases are presented in Fig. 5.4 (a) and (b), where the corresponding constellations, the source of the IQ data for the analysis, are also shown.

In both cases with different LO power, it is shown that both phase noise and amplitude noise are scaled with the symbol amplitude. Due to being multiplied with the signal, the scaled phase and amplitude noise by definition is multiplicative noise. In addition, the measured signals contain AWGN (as drawn in a dashed line) although it is clearly the multiplicative noise from the LO that is the dominant noise source. The AWGN is believed to be the noise floor in the

measurement setup. When the mixer is driven by a low-power LO, the amplitude noise conversion is increased to reach nearly the same amount of converted phase noise. More importantly, the result in Fig. 5.4 (b) is an indication that the white LO noise has equal phase and amplitude noise contributions. To the authors' best knowledge, this is the first experiment reported on the white LO noise properties.

The amount of amplitude noise converted through the mixer is dependent on the LO power level. However, the influence of the amplitude noise, even when it is only partially converted is not negligible for wideband systems, as in this example considering 6.5% EVM in (a) compared to 7% in (b).

5.2.3 LO noise influence on communication performance

A new LO model is developed [H], including a white noise floor, which is missing in previously published models. Particularly, the new model is needed for wideband mm-wave systems. In wideband communication, transmission performance suffers more from white LO noise than from near-carrier phase noise. The white LO noise in mm-wave systems is generally high due to the fact that the noise increases by $20\log_{10}(N)$ dB (see dashed line in Fig. 5.3), when a low-frequency LO is multiplied by N times to obtain a high frequency source [H].

The new LO model is described in time domain as follows,

$$V_{\mathrm{LO}}(t) = \cos(2\pi f_c t + \phi(t)) + v(t), \tag{5.1}$$

where f_c is the LO's center frequency, $\phi(t)$ represents the near-carrier phase noise, modelled as a Wiener process [53], and $v(t)$ denotes the white noise, modelled as AWGN. The effect of $v(t)$ on communication is different from AWGN in the receiver and the near-carrier phase noise $\phi(t)$.

The origin of the noise that affects the communication signal comes from using mixers for frequency up-/down-conversion. In [I], we use an ideal multiplier, in which suppression of the amplitude noise on the LO signal is not considered, to model a frequency conversion mixer. In the transmitter, the communication signal $x(t)$ is multiplied with the LO signal (5.1), and the resulting signal arriving at the receiver can be written as

$$\begin{aligned} V(t) &= x(t)\big(\cos(2\pi f_c t + \phi(t)) + v(t)\big) + w(t) \\ &= x(t)\cos(2\pi f_c t + \phi(t)) + x(t)v(t) + w(t) \end{aligned}, \tag{5.2}$$

where $w(t)$ is the AWGN noise floor in the receiver. Note that $w(t)$ is additive noise, while $x(t)v(t)$ is multiplicative noise, which is scaled with the amplitude of the input signal $x(t)$. It is also easy to realize that $\phi(t)$ enters the signal in a multiplicative way.

The influence of LO noise on the communication signal can be explained from eq. (5.2). Both $\phi(t)$ and $v(t)$ are multiplied with the signal so that symbols with a higher amplitude suffer more than those close to the origin. However, they affect the constellation in different ways as illustrated in Fig. 5.5 (a) and (b). $\phi(t)$ adds distortion only to the phase direction, while $v(t)$

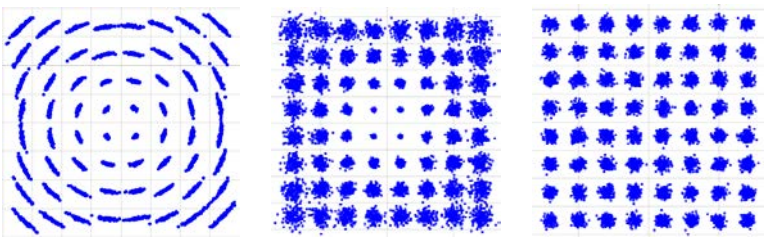

(a) (b) (c)

Figure 5.5: Simulated 64-QAM constellations with (a) only phase noise (b) only multiplicative white LO noise and (c) only AWGN noise.

contributes to circularly symmetrical noise clouds. Furthermore, $\phi(t)$ with a highly correlated nature from one symbol to the next, can be mitigated by phase tracking. Although the noise contribution $x(t)v(t)$ and the receiver AWGN $w(t)$ are both spectrally white and uncorrelated, they have different properties. The corresponding effect on the constellation is therefore different, as visualized in Fig. 5.5 (b) and (c). We can identify the relative contribution of the noise sources by analysing noise properties on the communication signal, as demonstrated in subsection 5.2.2.

5.3 Experimental verifications

We have provided experimental evidence (in 5.2.2) that the nature of the LO noise floor is white, including both phase and amplitude noise. Also, it is shown that in addition to phase noise, there is non-negligible contribution of amplitude noise through the frequency conversion mixer. As a consequence, the SNR of the frequency converted signal degrades as the LO noise floor increases, which is experimentally verified for both frequency up and down conversion. These are the main results, where we draw conclusions in [H], [I] that the capacity of wideband communication is primarily limited by the white LO noise floor.

Fig. 5.6 illustrates the experimental test-bench for the study of the LO noise floor influence through frequency conversion. The same setup is used for both frequency up and down measurements with swapped IF and RF frequency settings. It is implemented using a low-frequency mixer, driven by a 10 GHz LO. By reducing SNR at the LO output, the LO noise floor is increased to imitate typical noise performance of frequency multiplied mm-wave LOs. In this study, we assume that frequency multiplication does not change the LO noise properties. In the measurement setup, we manage to isolate the LO noise floor from other mixer-related impairments. The influence of LO noise floor is also isolated from the near-carrier phase noise by the way we degrade the noise floor as described in [H].

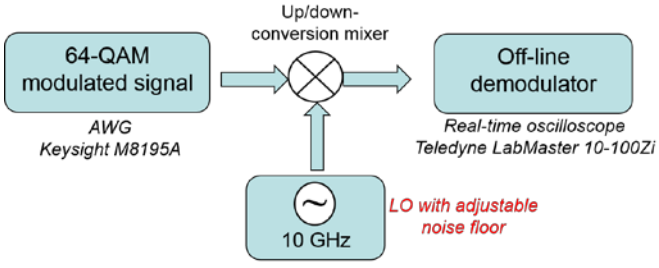

Figure 5.6: Measurement setup for performance evaluation of transmitter and receiver under noise floor influence of the corresponding LOs [I].

As shown in the measured noise spectrum in Fig. 5.7, the noise floor is varied in steps from −162 dBc/Hz without degradation up to −106 dBc/Hz, which is comparable to the level of a 94 GHz carrier after frequency multiplication [54]. Since the noise floor is reached already at 10 MHz offset frequency and there is no reason to believe it will not be flat farther out, we restrict the measurements up to 30 MHz for better measurement accuracy [55].

Measured EVM numbers of the frequency-converted 64-QAM signals at varied LO noise floor levels are presented in Fig. 5.8. It is shown that at all measured symbol rates for both up and down conversion, the signal EVM performance degrades when the LO noise floor is increased above −140 dBc/Hz. The flat EVM floor below −140 dBc/Hz is attributed to the noise floor from the measurement setup [H]. Signal spectra at 1 GBaud are captured and shown in Fig. 5.9 after up-conversion using the LO with degraded noise floors at −130 dBc/Hz and −112 dBc/Hz, respectively. The noise power is increased by approximately 15 dB, on the same order as the noise floor increase. It is evident that the white LO noise is converted through the mixer, thereby degrading the signal SNR.

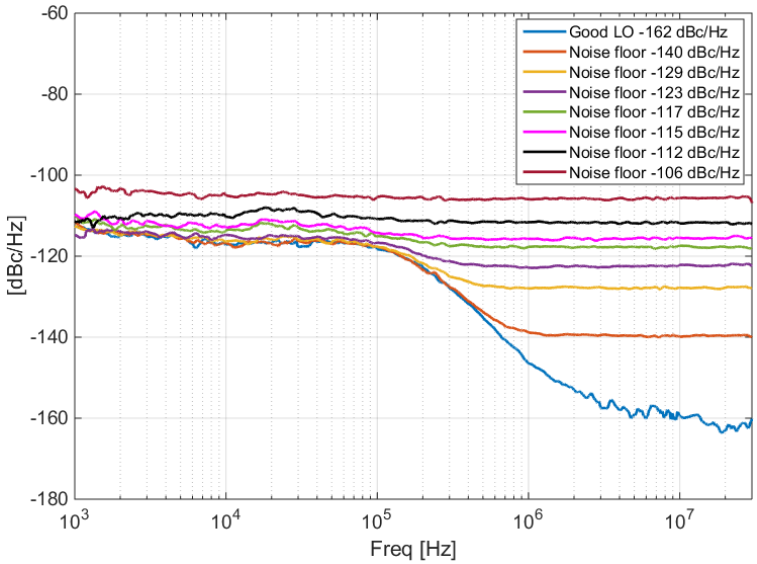

Figure 5.7: Measured LO noise profile with noise floor degradation [I].

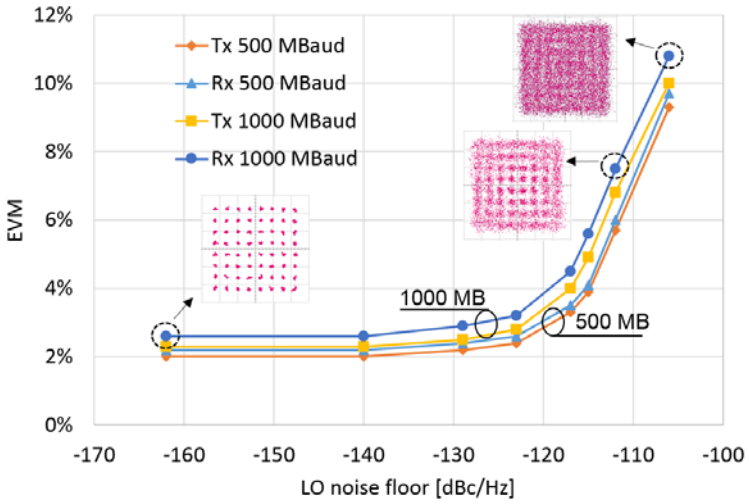

Figure 5.8: Measured transmitter and receiver EVM under varied LO noise floors at different symbol rates [I].

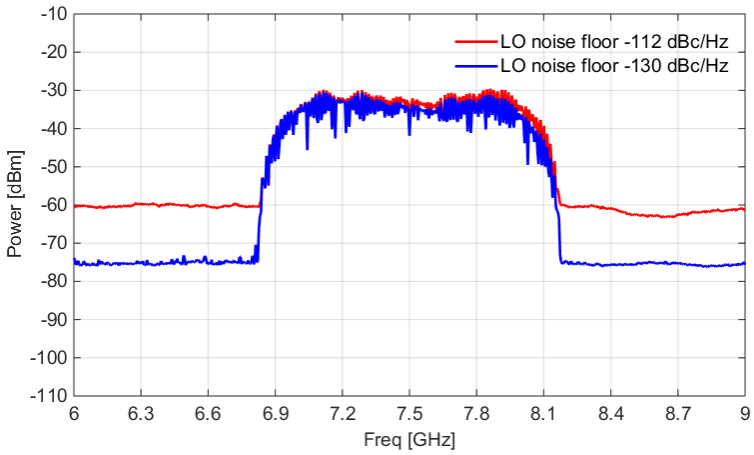

Figure 5.9: Measured up-converted 1 GBaud 64-QAM signal using LOs with degraded noise floors at −130 dBc/Hz and −112 dBc/Hz [I].

5.4 Hardware design improvements

In order to improve the SNR and thereby increase the achievable data rates, two design options to reduce the LO noise floor are proposed [I]. Using a BPF to suppress the noise floor outside the filter bandwidth is proven to be effective so that the signal quality can be restored. In particular, for conventional LO-multiplier chains (Fig. 5.10 (b)) where the LO noise floor is generally high, this approach is useful to minimize the performance loss due to the frequency multiplication. Fig. 5.10 (c) illustrates the LO-multiplier architecture with a BPF added at the multiplier output. In theory, the reduced noise floor could be even lower than the original floor of the low frequency LO. It is, however, in practical implementations determined by the filter stop-band attenuation (Q-value of the filter resonators). Moreover, filter bandwidth is a key design parameter, which shall be defined in relation to system specifications, such as modulation bandwidth/symbol rate, modulation format and communication performance.

The conventional LO-multiplier chain for mm-wave LO signal generations is an approach good for near-carrier phase noise, but not for the far-carrier white noise. Although it is feasible to suppress the white LO noise by filtering, it is at the expense of extra hardware and design complexity, especially if the LO needs to be tuned to different frequencies. The conclusions from our recent study in [H], [I] have implied that the LO hardware in future wideband communication systems shall be designed for low white noise. Thus, it would be advisable to design high-power and high-frequency LOs. A high output power makes sure that the SNR is high for the generated LO signal. A high-frequency fundamental LO avoids the need for frequency multiplication. As indicated by the corresponding LO noise profiles in Fig. 5.10 (b) and (d), compared to the conventional LO-multiplier chain, the high-frequency LO may offer a lower noise floor with a higher phase noise as a trade-off.

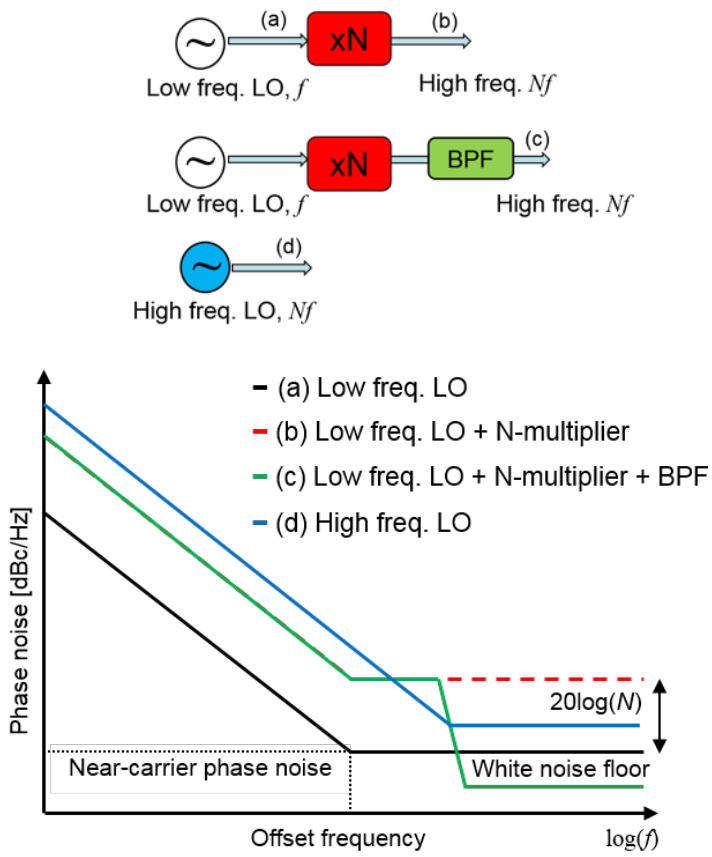

Figure 5.10: Block diagram of different LO architectures and the corresponding LO noise profiles [I].

5.4.1 Noise floor suppression using band pass filters

As a proof of concept, performance improvement by noise floor suppression is experimentally demonstrated using the same test-bench as in Fig. 5.6 with a narrow BPF inserted in the LO chain. The BPF is centered at 10 GHz with a −3 dB bandwidth of 5 MHz. The effect of noise floor suppression on the degraded LO is measured and presented in Fig. 5.11, including the LO without degradation for comparison. Outside the filter bandwidth, it is shown that the degraded noise floor at −112 dBc/Hz is restored to the level of the original LO below −160 dBc/Hz. Accordingly in Fig. 5.12, the EVM performance measured with the noise suppression LO is recovered to the same level as using the original LO. In addition, this result is an experimental proof that the near-carrier phase noise (in this case, 10 MHz offset from the carrier) has little impact on communication performance.

Derived from simulations, BPF bandwidth requirements are provided in relation to the symbol rate for 64-QAM modulation. Two BPF types are studied: Chebyshev and Butterworth. For a given LO noise floor and a performance threshold [I], simulations suggest that the bandwidth of BPF should be below 4% of the symbol rate for 5^{th} order Chebyshev and 2% of the symbol rate for 5^{th} order Butterworth. Therefore, for a 1 GBaud 64-QAM signal, the required bandwidth can be relaxed up to 40 MHz for a Chebyshev BPF compared to the 5 MHz BPF used in the measurement. Moreover, simulations indicate that a wider filter bandwidth could be used without affecting the performance at a lower level of the white LO noise.

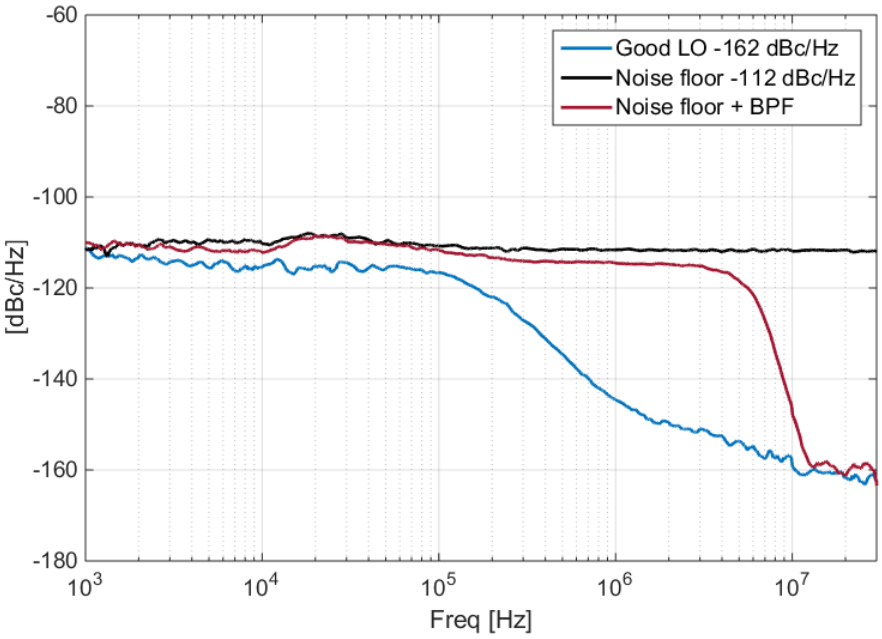

Figure 5.11: Measured noise suppression using BPF [I].

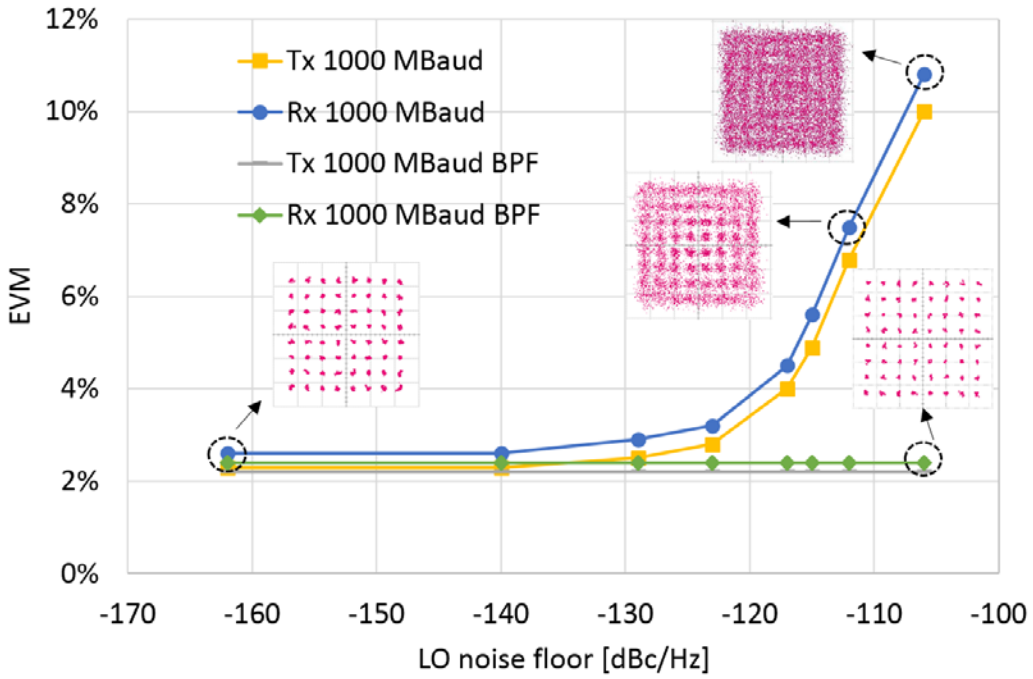

Figure 5.12: Measured transmitter and receiver EVM at 1 GBaud symbol rate with BPF noise suppression, comparing to without using BPF [I].

5.4.2 Proposal of a new LO architecture

As a compromise between near-carrier phase noise and far-carrier white noise, one design proposal is to aim at an intermediate high-frequency fundamental LO in wide-bandgap technology followed by a frequency multiplier with a low multiplication factor. For instance, state-of-the-art commercial GaN HEMT technologies can be used for high-power oscillators well above 50 GHz. A multiplication factor of 2 or 3 is then sufficient to reach the D-band for instance.

One issue with a high-frequency fundamental LO is that it requires additional circuitry for prescaling. To date, there are no commercially available PLLs beyond the Ku band. Fig. 5.13 shows an example of LO architecture based on a GaN HEMT VCO chip, an integrated frequency multiplier and prescaler, and a commercial PLL chip, e.g. ADF5355 from Analog Devices.

The near-carrier phase noise may also be an issue. Even if it has minor influence on capacity, as demonstrated in [H] and [I], it is still important for phase tracking and clock recovery. The near-carrier phase noise has to be taken into account in the design of the phase-locked loop. The loop bandwidth may be increased to compensate for the degraded near-carrier phase noise to avoid phase slipping issues. If the near-carrier phase noise is too high and cannot be handled by the clock recovery circuitry, a solution may be to use high-Q resonators, i.e. metallic cavity [56] or a dielectric resonator [57].

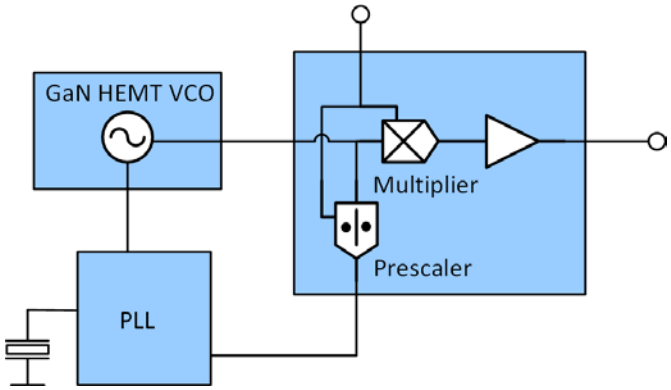

Figure 5.13: Proposed LO architecture for a future mm-wave system [I].

Chapter 6

Conclusions and Future Outlook

6.1 Conclusions

High data-rate transmission links are required to support the capacity evolution in 5G mobile networks and other future communication systems. This thesis presents hardware solutions [A-G] that address implementation challenges in high data-rate communication at mm-wave frequencies. Driven by strong commercial interest, the 70/80 GHz (E-band) has been the targeted frequency band for a majority of the system prototypes and demonstrations, although the proposed solutions are in principle generic.

Shannon's theorem introduces two technology alternatives for increased data rate: improving spectral efficiency (high-order modulation) and utilizing wide modulation bandwidth (high symbol rate). Millimeter-wave frequency bands offer multi-GHz modulation bandwidth, which in turn requires multi-gigabaud modulators and demodulators (Modems). Based on commercially available hardware, we propose modem designs that demonstrate multi-gigabaud mm-wave communication [A, B, C]. As opposed to conventional digital modems, the implementations in [B, C] are more hardware-efficient for reducing the cost and power consumption of the communication system. The digital demodulator in [B] is realized using minimum oversampling in the ADC, and thus allows higher symbol rate for a given ADC sampling speed. The multi-rate modem in [C], on the other hand, does not require any ADC due to its analog implementation. Another benefit of analog design is the inherently low latency, which makes it well-suited for wireless fronthaul applications, as demonstrated in [C].

Another aspect we address is the intrinsic bandwidth of the transmitter and receiver hardware, which has been evolving thanks to advanced semiconductor processes. Taking the advantage of InP DHBT technology, we present a multi-level baseband modulator circuit [D] with an experimentally verified data rate of 100 Gbps using 4-level amplitude modulation (PAM-4). When integrated with a laser, the PAM-4 transmitter achieves the highest reported data rate for short-range optical links, meanwhile being the most energy-efficient transmitter. In the same technology, a power detector circuit is reported for low-order wideband data transmission [E]. The circuit performance is verified over 100 to 150 GHz carrier frequency at a data rate of

13 Gbps, limited by the measurement setup. The achieved high energy efficiency (1.1 pJ/bit) makes the circuit attractive in low-power and high-speed applications.

Oscillator phase noise increases with the carrier frequency, which may limit the practical use of mm-wave frequencies. In [F], we report a phase noise mitigation technique using analog signal processing, which is therefore applicable to arbitrary mm-wave signal waveforms. As a key enabler, spectrally efficient transmission compliant with the LTE standard is demonstrated at E-band, as a showcase of a future 5G mm-wave system [G].

Fig. 6.1 summarizes the performance achieved for different hardware solutions in terms of data rate and spectral efficiency. For example, 100 Gbps is reached using simple modulation owing to wide bandwidth [D], and this would be very challenging to transmit over the air; while [G] enables high-order modulation over a high carrier frequency, but now within relatively narrow bandwidth. The solution in [B] takes a step towards combining spectrally efficient modulation with wide bandwidth. However, it has been challenging to the research community to implement this combination in practice, due to insufficient SNR. We provide experimental investigation in [H], [I], where a high noise floor from frequency-multiplied LO sources is identified as one primary limitation. A new understanding of data-rate limitation, with proposed hardware design improvements in [I], opens up extremely high data rate opportunities (i.e. beyond 100 Gbps as indicated by the outlined star in Fig. 6.1) in wireless communication.

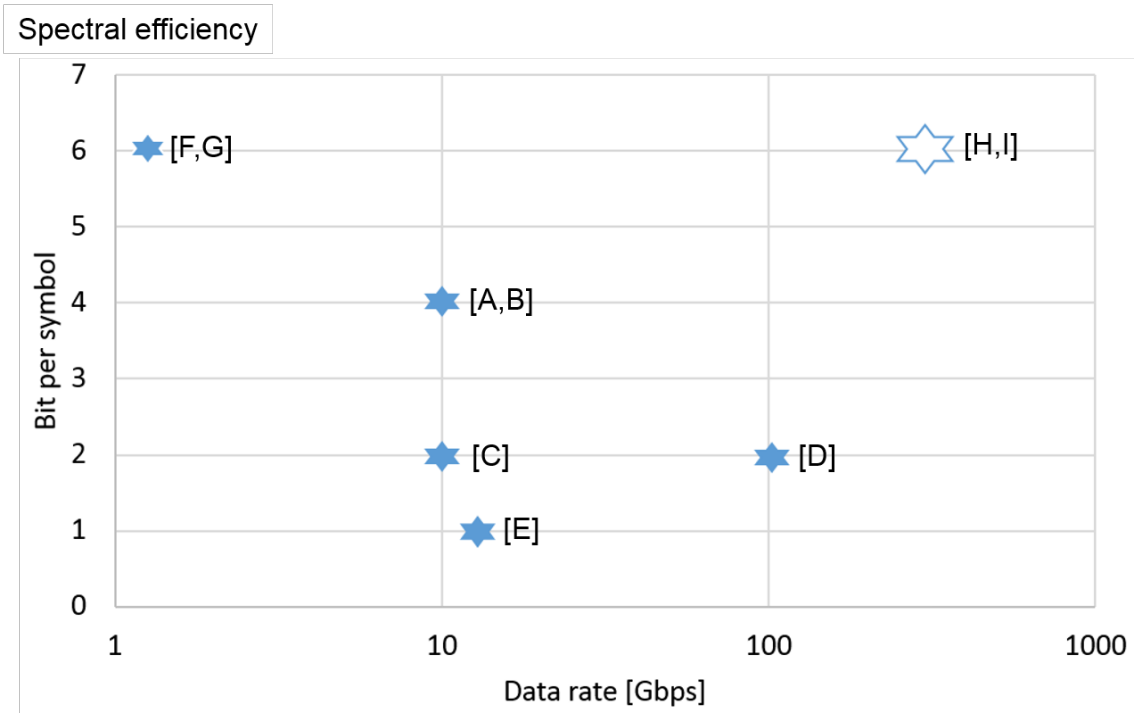

Figure 6.1: Summary of main results from appended papers [A–I], where solid stars represent demonstrated hardware solutions [A–G], and the outlined star indicates extremely high data rate potential for future implementations [H, I].

6.2 Research opportunities

The findings in papers [H] and [I] introduce new research opportunities. A few research topics are discussed in the following as examples in relation to the scope of this thesis.

New hardware designs

The conclusions drawn in [I], that the capacity of wideband communication is primarily limited by white LO noise floor, have implied that the LO hardware in these systems shall be designed for low white noise. We have suggested a new LO architecture based on GaN HEMT VCO. The proposal is to be implemented and verified.

A short-term solution is also proposed in [I], which uses a narrow BPF to suppress the LO noise floor. In wideband systems with LO-multiplier chains, this solution may be considered, although very narrow filters are generally challenging to implement at high frequencies.

System design and simulation

The bottleneck for deploying a spectrally efficient modulation is insufficient SNR, particularly in wideband systems. Aiming at a high SNR, simulation-assisted system design plays an important role in specifying key parameters as guidelines for circuit designers. Moreover, for a given hardware design e.g. front-end transceivers, there is a ‘sweet spot’ in terms of modulation order and bandwidth to achieve the best possible performance. System-level simulation offers the opportunity to choose the optimal combination.

Real-time system demonstration

So far, using spectrally more efficient modulation than OOK/ASK, 20 Gbps QPSK over 120 GHz is the highest data rate reported in a single channel for all electronic system demonstrators using real-time demodulation [18]. In the Swedish Foundation for Strategic Research (SSF) funded project ‘high data-rate wireless communications’, we have the goal of demonstrating 100 Gbps in a real-time system by means of spectrally efficient modulation in combination with multi-carrier technologies. The 140-GHz band, also known as the D-band, is currently considered as the target frequency band for the future system demonstration.

These are the paths that we have to pursue to realize future 5G mobile communication and the dream of an all-connected world.

Chapter 7

Summary of Appended Papers

This chapter summarizes the publications which are included in this thesis. For every publication, an abstract and a paragraph describing my contribution are provided.

Paper A

J. Chen, Z. He, L. Bao, C. Svensson, Y. Li, S. Gunnarsson, C. Stoij and H. Zirath, "10 Gbps 16QAM transmission over a 70/80 GHz (E-band) radio test-bed," in *Proc. 7th European Microwave Integrated Circuit Conference (EuMIC)*, Amsterdam, 2012, pp. 556-559.

This paper reports a millimeter-wave radio test-bed, which supports 16QAM transmission over 70/80 GHz band at data rates up to 10 Gbps. Performance of the 16QAM transmitter and receiver is evaluated in a loop-back lab set-up. With the proposed 10 Gbps on single carrier system architecture, it is possible to achieve 40 Gbps over a 5 GHz bandwidth when combined with polarization and spatial multiplexing.

My contribution: I designed the experiment, built the radio test-bed, performed measurements, analyzed the data, and wrote the paper.

Paper B

Z. He, **J. Chen**, C. Svensson, L. Bao, A. Rhodin, Y. Li, J. An and H. Zirath, "A hardware efficient implementation of a digital baseband receiver for high-capacity millimeter-wave radios," in *IEEE Transactions on Microwave Theory and Techniques*, vol. 63, no. 5, pp. 1683-1692, May 2015.

This paper presents an implementation solution for a digital baseband receiver, which consists mainly of an analog symbol timing recovery (STR) block and a digital carrier recovery block. The STR is realized based on "one-sample-per-symbol" sampling, resulting in relaxed requirements from the A/D converter's sampling speed. In this sense, the proposed solution is hardware-efficient. To functionally verify the solution, a proof-of-concept 5 Gbps E-band

system using 16 QAM modulation is implemented and tested in the laboratory. The test results demonstrate that the proposed solution works for high-capacity millimeter-wave radios for point-to-point links, one of the targeted applications.

My contribution: I took part in designing the experiment, performing measurements and data analysis. I built the system measurement setup, and contributed to writing the paper.

Paper C

J. Chen, Z. He, Y. Li, T. Swahn and H. Zirath, "A data-rate adaptable modem solution for millimeter-wave wireless fronthaul networks," in *IEEE International Conference on Communication Workshop (ICCW)*, London, 2015, pp. 1-6.

In this paper, we present a novel differential encoding scheme for differential quadrature phase-shift keying (D-QPSK) modulation, which enables data-rate adaptable transmission without modification of a standard receiver. A multi-rate D-QPSK modulator/demodulator (modem) is implemented and tested for data rates up to 10 Gbps, limited by the bandwidth of the microwave components in use. It has been verified that this modem meets the fronthaul link requirements with respect to multi-gigabit, low latency and high system performance. Therefore, it is proposed for the implementation of wireless fronthaul links using millimeter-wave bands.

My contribution: Together with Z. He I built the modem setup and performed measurements. I built the radio link used to characterize the modem solution, and I wrote the paper.

Paper D

J. Chen, Z. He, T. Lengyel, K. Szczerba, P. Westbergh, J. S. Gustavsson, H. Zirath and A. Larsson, "An energy efficient 56 Gbps PAM-4 VCSEL transmitter enabled by a 100 Gbps driver in 0.25 μm InP DHBT technology," in *Journal of Lightwave Technology*, vol. 34, no. 21, pp. 4954-4964, Nov. 2016.

As a potential technology enabler for next-generation VCSEL-based optical interconnects, this paper presents a wide-bandwidth and energy-efficient multilevel pulse-amplitude-modulation (PAM) VCSEL driver implemented in InP 0.25 μm double-heterojunction bipolar transistor (DHBT) technology. Error-free electrical data transmission up to 56 Gbps PAM-2 and 100 Gbps PAM-4 is demonstrated at a driver energy consumption less than 2 pJ/bit. The driver is integrated and tested with an in-house fabricated 850 nm VCSEL. Error-free 56 Gbps PAM-4 optical transmission at a transmitter energy consumption of 3.7 pJ/bit is demonstrated without equalization. This is the highest data rate reported for an integrated PAM-4 modulated VCSEL transmitter, while being most energy-efficient above 40 Gbps operation.

My contribution: The driver circuit was designed by Z. He. I designed the experiment, performed measurements, analyzed the data, and wrote the paper.

Paper E

M. Bao, **J. Chen**, R. Kozhuharov and H. Zirath, "A high speed power detector for D-band communication," in *IEEE Transactions on Microwave Theory and Techniques*, vol. 62, no. 7, pp. 1515-1524, July 2014.

This paper presents a D-band power detector (PD) consisting of a four-way power divider and four identical active PD units. The proposed PD is designed and manufactured in 0.25-μm InP DHBT technology, which is characterized by on-chip measurements with both a sinusoidal signal and a binary amplitude shift-keying modulated signal at data rates up to 13 Gb/s over carrier frequencies from 100 to 150 GHz. Measured bit error rate (BER) is less than 10^{-12} at the carrier frequency of 120 GHz. In addition, the proposed PD achieves state-of-the-art low power consumption at 15 mW, corresponding to the lowest reported energy per bit of 1.1 pJ/bit.

My contribution: The circuit was designed by M. Bao. I designed the data transmission experiment, performed measurements, analyzed the results, and wrote the measurement section of the paper.

Paper F

J. Chen, B. E. Olsson, A. Persson and J. Hansryd, "Experimental demonstration of RF-pilot-based phase noise mitigation for millimeter-wave systems," in *IEEE 80th Vehicular Technology Conference (VTC2014-Fall)*, Vancouver, BC, 2014, pp. 1-5.

Millimeter-wave bands are gaining popularity for high data rate wireless communication. However, oscillator phase noise also increases as the carrier frequency increases. Methods of phase noise mitigation are therefore crucial for future millimeter-wave systems. In this paper, we propose to adopt analog phase noise mitigation using an RF pilot-tone, which reduces both phase and frequency impairments of an arbitrary millimeter-wave signal at the expense of reduced spectral efficiency. The method is verified experimentally at carrier frequency of 28 GHz and E-band 73 GHz showing a 20 dB noise reduction up to 100 kHz offset. Since the method relaxes the phase noise requirement, it is attractive for phase noise sensitive technologies at high carrier frequency. Taking OFDM technology used in LTE as an example, simulation results indicate that the reduced phase noise using the pilot method enables an LTE signal on a millimeter-wave carrier with marginal performance impact.

My contribution: I designed the experiment, built the measurement setup, performed measurements, analyzed the data, and wrote the paper.

Paper G

J. Chen, B. E. Olsson, J. Hansryd and I. Gerszberg, "Demonstration of analog millimeter-wave fronthaul link for 64-QAM LTE signal transmission," in *IEEE 82nd Vehicular Technology Conference (VTC2015-Fall)*, Boston, MA, 2015, pp. 1-5.

In this paper, we propose an analog wireless fronthaul concept to enable bandwidth-efficient and scalable fronthaul networks. The basic idea is to transport narrow band analog radio signals over millimeter-wave bands instead of multi-gigabit digital signals. The phase and frequency impairments introduced by high frequency carriers are effectively reduced using an analog pilot-based mitigation technique. As a proof-of-concept demonstration, an analog fronthaul link is implemented, and the link performance is verified for 20 MHz 64-QAM LTE transmission over 70/80 GHz (E-band).

My contribution: I designed the experiment, built the radio link demonstrator, performed measurements, analyzed the data, and wrote the paper.

Paper H

J. Chen, Z. He, D. Kuylenstierna, T. Eriksson, M. Hörberg, T. Emanuelsson, T. Swahn and H. Zirath, "Does LO noise floor limit performance in multi-gigabit millimeter-wave communication?," in *IEEE Microwave and Wireless Components Letters*, vol. 27, no. 8, pp. 769-771, Aug. 2017.

Extremely high data rate communication can potentially be achieved by combining high-order modulations and wide bandwidths at millimeter-wave (mm-wave) frequencies. However, it has been challenging to implement this combination in practice. In this paper, we present an experimental investigation of whether the white noise floor of frequency-multiplied LO sources is a major noise contribution to wideband signals. Hardware measurements are performed using multi-gigabit 64-QAM signals. The measured results show that the transmitter performance degrades as the LO noise floor increases. Hence, the LO noise floor is identified as a primary limitation on achieving the highest possible data rate in wideband mm-wave systems.

My contribution: I designed the experiment, performed measurements, and wrote the paper.

Paper I

J. Chen, D. Kuylenstierna, S. E. Gunnarsson, Z. He, T. Eriksson, T. Swahn, H. Zirath, "Influence of white LO noise on wideband millimeter-wave communication," *submitted to IEEE Transactions on Microwave Theory and Techniques, September 2017*.

In this paper, we present a mathematical model to describe the influence of LO noise on frequency conversions. Followed by experimental investigations using multi-gigabit 64-QAM signals, measurements are performed at up and down frequency conversions. Both cases show SNR degradation as the corresponding LO noise floor increases. For an explanation, we provide an experimental proof that the nature of the LO noise floor is white, with nearly the same amount of phase and amplitude noise. Various ways to reduce the noise floor through hardware design improvements are discussed. The discussions are supported by numerical simulations, where key hardware requirements are also proposed.

My contribution: I developed the mathematical model and the simulation model, designed the experiment, performed measurements, and wrote the paper with support in discussion with the co-authors.

Acknowledgments

Now I come to the moment when I feel truly close to the finishing line in a long race. During the past 7 years, I was part-time pursuing my PhD study and part-time working as an Ericsson employee. There were certainly moments when I felt it was mission impossible to fulfil all the requirements. Finally I made it through with support from many people, so that I am ready to finish the race.

I would like to take this opportunity to express my deep gratitude to all the people who helped me make it happen.

First of all, I want to thank my first manager Dr. Thomas Lewin for giving me the opportunity to work at Ericsson Research. It was his trust that encouraged me to take on the challenge to start my PhD study. Also, I am very grateful to Prof. Herbert Zirath for accepting me as a PhD student in the first place. It was his attitude to research that inspired me to take my work forward, and it was his kindness that supported me all the way through. Being my main supervisor, Associate Prof. Thomas Swahn deserves a big thanks for sharing so much knowledge and experience with me. It was his enthusiasm and trust that made me believe in myself. In addition, I am very thankful to Docent Sten E. Gunnarsson as my assistant supervisor for providing so much concrete feedback and ideas on everything. It was his encouragement that lightened up my way at low points. Special thanks go to Prof. Thomas Eriksson for his supervision and support on work related to modelling and simulation. His persistence motivated me to produce the best possible results. Besides, I owe Dr. Zhongxia (Simon) He a huge thank-you for being such a wonderful colleague and supervisor. It would not have been possible to produce these many results without his contributions and hard work.

I would like to say thank you to all my colleagues at Ericsson Research and everybody at Microwave Electronics Laboratory for creating such a friendly environment. I am especially very grateful to Yinggang Li, Jonas Hansryd, Bengt-Erik Olsson, Dan Kuylenstierna, Koen Buisman and Thomas Emanuelsson for sharing their expertise and valuable discussions. Tamas Lengyel, Krzysztof Szczerba, Mikael Mazur and Prof. Anders Larsson in the Photonics group that I got to know through collaboration, also deserve a big thank-you for their support.

However, life is not all about work! Thanks Anna for being my lunch buddy. Thanks Lei and Tingting for their initiatives in organizing weekend gatherings. Thank you all my friends for making my life more colorful! Zonghe, my best friend, deserves a huge thank-you for always being there for me from the very beginning. I would not have got this far without him. I want

to thank Géza for showing me the world (not only on a map☺). Thank you for so much laughter, support and so many kilometers that we made together.

Last but not least, I must say thank you to my parents. It is their unconditional love that supports me in pursuing my goals and being myself. I love you very much!

This work was jointly financed by the Swedish Foundation for Strategic Research (SSF) via the ‘High Datarate Wireless Communications’ project and the ‘Multi-Tbps Optical Interconnects’ project, as well as by Ericsson Research, Ericsson AB.

References

[1] Ericsson mobility report, November 2015.
https://www.ericsson.com/assets/local/news/2016/03/ericsson-mobility-report-nov-2015.pdf

[2] Ericsson Review 5G radio access, 6/2014.
https://www.ericsson.com/assets/local/publications/ericsson-technology-review/docs/2014/er-5g-radio-access.pdf

[3] China mobile research institute, "C-RAN the road towards green RAN," White paper v. 2.6, Sept. 2013.

[4] Ericsson microwave towards 2020, September 2015.
https://www.ericsson.com/assets/local/news/2014/9/microwave-towards-2020.pdf

[5] F. Boes *et al*., "Ultra-broadband MMIC-based wireless link at 240 GHz enabled by 64GS/s DAC," in *39th International Conference on Infrared, Millimeter, and Terahertz waves (IRMMW-THz)*, Tucson, AZ, 2014, pp. 1-2.

[6] K. Eriksson, I. Darwazeh and H. Zirath, "InP DHBT Distributed Amplifiers With Up to 235-GHz Bandwidth," in *IEEE Transactions on Microwave Theory and Techniques*, vol. 63, no. 4, pp. 1334-1341, April 2015.

[7] C. E. Shannon, "A mathematical theory of communication," in *The Bell System Technical Journal*, vol. 27, no. 4, pp. 623-656, Oct. 1948.

[8] J. R. Pierce. *An Introduction to Information Theory: Symbols, Signals and Noise*. Dover Publications, New York, 1980.

[9] Ericsson Review Microwave capacity evolution, 1/2011.
https://www.ericsson.com/res/docs/review/Microwave-Capacity-Evolution.pdf

[10] Ericsson Microwave Outlook report 2016, Ericsson, October 2016.
https://www.ericsson.com/assets/local/microwave-outlook/documents/ericsson-microwave-outlook-report-2016.pdf

[11] Ericsson Review Microwave Backhaul beyond 100 GHz, 2/2017.
https://www.ericsson.com/assets/local/publications/ericsson-technology-review/docs/2017/etr-beyond-100ghz.pdf

[12] J. Wells, "Faster than fiber: The future of multi-G/s wireless," in *IEEE Microwave Magazine*, vol. 10, no. 3, pp. 104-112, May 2009.

[13] P. Larsson, "Lattice array receiver and sender for spatially orthonormal MIMO communication," in *Proc. IEEE 61st Vehicular Technology Conference*, Stockholm, 2005, pp. 192-196, vol. 1.

[14] ITU Radio Regulations, part 1 chapter II article 5 (frequency allocations) and part 3 resolution 767 (studies towards an identification for use by administrations for land-mobile and fixed services applications operating in the frequency range 275-450 GHz).

[15] S. Carpenter *et al*., "A D-Band 48-Gbit/s 64-QAM/QPSK Direct-Conversion I/Q Transceiver Chipset," in *IEEE Transactions on Microwave Theory and Techniques*, vol. 64, no. 4, pp. 1285-1296, April 2016.

[16] K. Katayama *et al*., "A 300 GHz CMOS Transmitter With 32-QAM 17.5 Gb/s/ch Capability Over Six Channels," in *IEEE Journal of Solid-State Circuits*, vol. 51, no. 12, pp. 3037-3048, Dec. 2016.

[17] I. Kallfass *et al*., "All Active MMIC-Based Wireless Communication at 220 GHz," in *IEEE Transactions on Terahertz Science and Technology*, vol. 1, no. 2, pp. 477-487, Nov. 2011.

[18] H. Takahashi, A. Hirata, J. Takeuchi, N. Kukutsu, T. Kosugi and K. Murata, "120-GHz-band 20-Gbit/s transmitter and receiver MMICs using quadrature phase shift keying," in *Proc. 7th European Microwave Integrated Circuit Conference*, Amsterdam, 2012, pp. 313-316.

[19] C. Thakkar, L. Kong, K. Jung, A. Frappe, and E. Alon, "A 10 Gb/s 45mW adaptive 60 GHz baseband in 65 nm CMOS," in *IEEE Journal of Solid-State Circuits.*, vol. 47, no. 4, pp. 952-968, Apr. 2012.

[20] A. C. Ulusoy and H. Schumacher, "Multi-Gb/s analog synchronous QPSK demodulator with phase-noise suppression," in *IEEE Transactions on Microwave Theory and Techniques*, vol. 60, no. 11, pp. 3591-3598, Nov. 2012.

[21] T. Tsukizawa *et al.*, "A fully integrated 60-GHz CMOS transceiver chipset based on WiGig/IEEE 802.11ad with built-in self calibration for mobile usage," in *IEEE Journal of Solid-State Circuits*, vol. 48, no. 12, pp. 3146-3159, Dec. 2013.

[22] V. Dyadyuk *et al.*, "A multigigabit millimeter-wave communication system with improved spectral efficiency," in *IEEE Transactions on Microwave Theory and Techniques*, vol. 55, no. 12, pp. 2813-2821, Dec. 2007.

[23] M. S. Kang, B. S. Kim, K. S. Kim, W. J. Byun, and H. C. Park, "16-QAM-based highly spectral-efficient e-band communication system with bit rate up to 10 Gbit/s," in *ETRI J.*, vol. 34, no. 5, pp. 649-654, Oct. 2012.

[24] K. Okada *et al.*, "A full four-channel 6.3-Gb/s 60-GHz CMOS transceiver with low-power analog and digital baseband circuitry," in *IEEE Journal of Solid-State Circuits*, vol. 48, no. 1, pp. 46-65, Jan. 2013.

[25] C. Wang *et al.*, "A 10-Gbit/s wireless communication link using 16-QAM modulation in 140-GHz band," in *IEEE Transactions on Microwave Theory* and *Techniques*, vol. 61, no. 7, pp. 2737-2746, Jul. 2013.

[26] C. Wang *et al*., "0.34-THz Wireless Link Based on High-Order Modulation for Future Wireless Local Area Network Applications," in *IEEE Transactions on Terahertz Science and Technology*, vol. 4, no. 1, pp. 75-85, Jan. 2014.

[27] F. Xiong, *Digital Modulation Techniques*, 2nd edition Norwood, USA: Artech House, 2006, ch. 9.

[28] N. K. Jablon, "Joint blind equalization, carrier recovery and timing recovery for high-order QAM signal constellations," in *IEEE Transactions on Signal Processing*, vol. 40, no. 6, pp. 1383-1398, Jun. 1992.

[29] L. Franks, "Carrier and bit synchronization in data communication−A tutorial review," in *IEEE Transactions on Communications*, vol. 28, no. 8, pp. 1107-1121, Aug. 1980.

[30] H. Takahashi, T. Kosugi, A. Hirata, K. Murata, N. Kukutsu, "10-Gbit/s Quadrature Phase-Shift-Keying modulator and demodulator for 120-GHz-Band wireless links," in *IEEE Transactions on Microwave Theory and Techniques*, vol. 58, no.12, pp. 4072-4078, Dec. 2010.

[31] J. Hacker *et al.*, "THz MMICs based on InP HBT technology," in *IEEE MTT-S International Microwave Symposium*, Anaheim, CA, 2010, pp. 1-1.

[32] K. Szczerba, P.Westbergh, M. Karlsson, P. A. Andrekson, and A. Larsson, "60 Gbits error-free 4-PAM operation with 850 nm VCSEL," in *Electronics Letters*, vol. 49, no. 15, pp. 953-955, Jul. 2013.

[33] W. Soenen *et al.*, "40 Gb/s PAM-4 transmitter IC for long-wavelength VCSEL links," in *IEEE Photonics Technology Letters*, vol. 27, no. 4, pp. 344-347, Feb. 2015.

[34] CPRI interface specification, v. 6.0, Aug. 2013.

[35] P. Westbergh *et al.*, "High-speed oxide confined 850-nm VCSELs operating error-free at 40 Gb/s up to 85 °C," in *IEEE Photonics Technology Letters*, vol. 25, no. 8, pp. 768-771, Apr. 2013.

[36] K. Szczerba *et al.*, "30 Gbps 4-PAM transmission over 200m of MMF using an 850 nm VCSEL," in *European Conference and Exhibition on Optical Communication*, Geneva, 2011, pp. 1-3.

[37] C.-H. Lin, C.-H. Tsai, C.-N. Chen, and S.-J. Jou, "4/2 PAM serial link transmitter with tunable pre-emphasis," in *Proc. International Symposium on Circuits and Systems*, 2004, pp. I-952-5, vol. 1.

[38] A. V. Rylyakov *et al.*, "A 40-Gb/s, 850-nm, VCSEL-based full optical link," in *OFC/NFOEC*, Los Angeles, CA, 2012, pp. 1-3.

[39] T. Lengyel, K. Szczerba, P. Westbergh, M. Karlsson, A. Larsson, and P. Andrekson, "Sensitivity improvements in an 850 nm VCSEL transmitter using a one-tap pre-emphasis

electronic filter," in *European Conference on Optical Communication (ECOC)*, Valencia, 2015, pp. 1-3.

[40] P. Westbergh, E. Haglund, R. Safaisini, J. S. Gustavsson, and A. Larsson, "High-speed 850 nm VCSELs operating error free up to 57 Gbit/s," in *Electronics Letters*, vol. 49, no. 16, pp. 1021-1023, Aug. 2013.

[41] M. Hörberg, "Low phase noise GaN HEMT Oscillator design based on high-Q resonators," PhD thesis, Department of Microtechnology and Nanoscience, Chalmers University of Technology, Gothenburg, April 2017.

[42] M. R. Khanzadi, R. Krishnan, and T. Eriksson, "Estimation of Phase Noise in Oscillators with Colored Noise Sources," in *IEEE Communications Letters*, vol. 17, no. 11, pp. 2160-2163, November 2013.

[43] S. L. Jansen, I. Morita, T. C. W. Schenk, N. Takeda, and H. Tanaka, "Coherent optical 25.8-Gb/s OFDM transmission over 4160-km SSMF," in *Journal of Lightwave Technol*ogy, vol. 26, no. 1, pp. 6-15, Jan. 2008.

[44] B. E. Olsson, C. Larsson, J. Mårtensson, and A. Alping, "Analog electrical phase noise compensation for coherent optical receivers," in *ECOC Technical Digest*, Sep. 2012.

[45] I. Ando, M. Tanio, M. Ito, T. Kuwabara, T. Marumoto and K. Kunihiro, "Wireless D-band communication up to 60 Gbit/s with 64QAM using GaAs HEMT technology," in *IEEE Radio and Wireless Symposium (RWS)*, Austin, TX, 2016, pp. 193-195.

[46] T. Nagatsuma *et al*., "Real-time 100-Gbit/s QPSK transmission using photonics-based 300-GHz-band wireless link," in *IEEE International Topical Meeting on Microwave Photonics (MWP)*, Long Beach, CA, 2016, pp. 27-30.

[47] S. Koenig *et al*., "100 Gbit/s wireless link with mm-wave photonics," in *Optical Fiber Communication Conference and the National Fiber Optic Engineers Conference (OFC/NFOEC)*, Anaheim, CA, 2013, pp. 1-3.

[48] K. Katayama, K. Takano, S. Amakawa, S. Hara, T. Yoshida and M. Fujishima, "CMOS 300-GHz 64-QAM transmitter," in *IEEE MTT-S International Microwave Symposium (IMS)*, San Francisco, CA, 2016, pp. 1-4.

[49] H. J. Song *et al.*, "50-Gb/s Direct Conversion QPSK Modulator and Demodulator MMICs for Terahertz Communications at 300 GHz," in *IEEE Transactions on Microwave Theory and Techniques*, vol. 62, no. 3, pp. 600-609, March 2014.

[50] M. R. Khanzadi *et al*., "Calculation of the Performance of Communication Systems from Measured Oscillator Phase Noise," in *IEEE Transactions on Circuits and Systems I, Reg. Papers*, vol. 61, no. 5, pp. 1553-1565, May 2014.

[51] J. Antes and I. Kallfass, "Performance Estimation for Broadband Multi-Gigabit Millimeter- and Sub-Millimeter-Wave Wireless Communication Links," in *IEEE Transactions on Microwave Theory and Techniques*, vol. 63, no. 10, pp. 3288-3299, Oct. 2015.

[52] D. del Rio *et al*., "A Wideband and High-Linearity E-B and Transmitter Integrated in a 55-nm SiGe Technology for Backhaul Point-to-Point 10-Gb/s Links," in *IEEE Transactions on Microwave Theory and Techniques*, vol. 65, no. 8, pp. 2990-3001, Aug. 2017.

[53] A. Demir, A. Mehrotra, and J. Roychowdhury, "Phase noise in oscillators: a unifying theory and numerical methods for characterization," in *IEEE Transactions on Circuits and Systems I: Fundamental Theory and Applications*, vol. 47, no. 5, pp. 655-674, May 2000.

[54] U. Lewark, A. Tessmann, H. Massler, A. Leuther and I. Kallfass, "Active frequency multiplier-by-nine MMIC for millimeter-wave signal generation," in *German Microwave Conference*, Darmstadt, 2011, pp. 1-4.

[55] *R&S FSUP Signal Source Analyzer Specifications, Data Sheet 06.03*.

[56] M. Hörberg, T. Emanuelsson, S. Lai, T. N. D. Thanh, H. Zirath and D. Kuylenstierna, "Phase-Noise Analysis of an X-Band Ultra-Low Phase-Noise GaN HEMT Based Cavity Oscillator," in *IEEE Transactions on Microwave Theory and Techniques*, vol. 63, no. 8, pp. 2619-2629, Aug. 2015.

[57] P. Rice *et al*., "A 10 GHz dielectric resonator oscillator using GaN technology," in *IEEE MTT-S International Microwave Symposium Digest*, 2004, pp. 1497-1500, vol. 3.